Master's thesis

NTNU
Norwegian University of Science and Technology
Faculty of Natural Sciences
Department of Materials Science and Engineering

Marita Kyllingstad

Epoxy based coatings with graphene and graphene oxide additions for antifouling applications

Master's thesis in Material Science and Chemical Engineering
Supervisor: Hilde Lea Lein
Co-supervisor: Ingrid Hallsteinsen, Sidsel Meli Hanetho, Matilde Skogen Chauton and Anh Hoang Dam

June 2021

NTNU
Norwegian University of Science and Technology

Marita Kyllingstad

Epoxy based coatings with graphene and graphene oxide additions for antifouling applications

Master's thesis in Material Science and Chemical Engineering
Supervisor: Hilde Lea Lein
Co-supervisor: Ingrid Hallsteinsen, Sidsel Meli Hanetho, Matilde Skogen Chauton and Anh Hoang Dam
June 2021

Norwegian University of Science and Technology
Faculty of Natural Sciences
Department of Materials Science and Engineering

NTNU
Norwegian University of
Science and Technology

Preface

This thesis is submitted to the Norwegian University of Science and Technology (NTNU) in the course "TMT4900 Material Chemistry and Energy Technology, Master's Thesis" as the final examination of the Master of Science degree within the field of Chemical Engineering and Biotechnology.

The thesis work was performed from January 2021 to June 2021 and is built on the work performed by the author during the specialization project which was carried out from August 2020 to December 2020. The experimental work was performed at laboratories at the Department of Material Science, NTNU Nanolab, Department of Chemical Engineering and Department of Physics. All the laboratory work was performed by the author, but the MATLAB script found in the Appendix C is developed by Senior Engineer Astrid Bjørkøy at the Department of Physics at NTNU. The head supervisor for this thesis was Associate Professor Hilde Lea Lein. The work has been supported by SINTEF Industri, SINTEF Ocean and CealTech AS with Research Scientist Sidsel Meli Hanetho, Senior Research Scientist Matilde Skogen Chauton and Senior Material Chemist Anh Hoang Dam as respectively co-supervisors. Associate Professor Ingrid Hallsteinsen at NTNU was also a co-supervisor for this master's thesis. The thesis was also supported by the research group Functional Materials and Materials Chemistry (FACET) at NTNU.

CealTech AS provided the graphene oxide paste, graphene dispersion and the epoxy Epikote 828. Algae nutrition medium was provided by the Department of Biotechnology and Food Science (IBT) at NTNU while SINTEF Ocean provided the algae tribal culture.

Trondheim, 06.06.2021

Marita Kyllingstad

Acknowledgements

Writing a master's thesis during the Covid-19 pandemic has been challenging, but not impossible due to the great support I have had from all my supervisors, friends and family. I wish to extend my special thanks to my head supervisor Hilde Lea Lein for her great support to my work as well as her inspiring words during our weekly meetings. The assistance provided by my co-supervisors Sidsel Meli Hanetho and Ingrid Hallsteinsen on these weekly meetings is also greatly appreciated. Your helpful tips and feedback on my laboratory work gave me motivation throughout the year.

My co-supervisor Matilde Skogen Chauton deserves a huge thanks for all our e-mails and meetings to discuss the work and theory of algae and marine growth. Your valuable insight improved my work significantly and helped optimizing my laboratory set-up. I want to express my thanks to my co-supervisor Anh Hoang Dam. Thank you so much for joining our team and providing me with useful tips with respect to the behavior of graphene and graphene oxide materials.

It has been challenging finishing the laboratory work due to the ventilation reparation which was performed on most of the laboratories used in this thesis. I want to thank the technical staff at the laboratories for making time in their schedules to provide me with the required training in a safe manner with respect to Covid-19 and the ventilation reparation. In particular, I want to thank Senior Engineer Anita Storsve for all her support, relocation assistance regarding the laboratory work and for always helping me whenever needed at the laboratories. I also want to address a special thanks to Senior Engineer Astrid Bjørkøy for spending hours with me at the fluorescence microscopy and to Senior Engineer Johannes Ofstad for all his valuable insight when performing surface tension measurements. The electronic workshop, the glassblowing workshop and the mechanical workshop also deserve a huge thanks for their help with pump speed adjustments, preparation the biofilm reactor, preparation of of sample holders for the biofilm reactor and substrates respectively.

Due to the pandemic, there has been only digitally meetings once a week with my research group FACET throughout the semester. I want to extend a big thanks to all the professors, Ph.D candidates and other master students in the group for giving me valuable comments during my presentations, helping when facing difficulties with the laboratory work and the positive tone within the group. The small talks with my fellow students at the study halls of IMA have been greatly appreciated during the semester and has helped on my motivation to face the challenges appearing in the laboratory work.

Finally, my partner, friends and family deserve a great thanks for always believing in me and supporting me whenever needed. Even though you may have had to discuss topics which are not exactly your favorites with me throughout the semester, I hope you know how much I appreciate each and everyone of you!

Abstract

The process in which marine growth is undesirable accumulated onto submerged construction is called biofouling. Prevention of biofouling is beneficial with respect to economical aspects, environmental issues, costs and maintenance for several marine industries. By depositing an antifouling coating containing additives with antifouling properties, the biofouling can be limited. Coatings with additions of graphene materials appear as promising low toxic antifouling coatings and can possibly be a substitute for the higher toxic copper coatings which are commonly used today. In addition, graphene based coatings also exhibit great mechanical properties.

The overall aim of this master's thesis was to prepare epoxy based antifouling coatings with additions of graphene (G) and graphene oxide (GO) and investigate their antifouling and surface properties. Characterization of surface properties as roughness, particle distribution, microstructure, contact angles and surface free energy were performed in addition to the antifouling properties. Biofilms were generated by submerging coated samples in a biofilm reactor with an algae tribal culture representing a realistic sea environment. A quantification method based on counting number of diatoms at submerged samples by using optical microscopy was suggested. Furthermore, a method to investigate the biofilm thicknesses was proposed by utilizing fluorescence microscopy in combination with the software MATLAB.

The sol-gel method was used to prepare two coating systems: the epoxy resin bisphenol A diglycidyl ether (DGEBA) with additions of GO and the epoxy resin Epikote 828 with additions of G. The GO slurries were found partly stable one week after preparation while the G slurries appeared stable even after three weeks.

Polyethylene substrates were spray coated with the prepared sols and slurries in two, three and four coating layers. Small microcracks were observed on all the prepared coatings due to the high content of volatile solvents. The GO and G particles were evenly distributed within the cured coating matrices. The coated samples exhibited a significantly more hydrophilic character compared to the un-coated substrates due to the reduced surface roughness of the coated samples. Consequently, less growth was observed on all the coated samples. The roughness of GO containing coatings were slightly higher compared to the other coatings resulting in a greater contact surface between the GO sheets and marine growth. The combined effect explained why the GO coatings exhibited better antifouling properties compared to the G coatings.

The marine growth reduced with increasing GO or G content within the coatings and was found to be independent of number of coating layers. Diatoms were found to be the dominating fouling organism on the submerged samples, although bacterial growth was also observed. The dominating antifouling mechanism of the GO and G coatings were assumingly related to oxidative stress. The experimental procedure for generation of biofilms was successful, but can be enhanced further by increasing the light access and using an algae culture of known composition. Characterization of diatoms may benefit from measuring a larger part of the sample surface as diatoms were found growing unevenly on the sample surface. The coatings containing 0.250 wt% GO appeared as the optimal coating with respect to surface and antifouling properties. Regarding further work, the mechanical properties must be investigated to evaluate the marine applicability of the prepared coatings.

Samandrag

Prosessen der uønsket marin vekst akkumuleres på marine konstruksjoner kalles biologisk begroing. Forebygging av biologisk begroing er gunstig med hensyn til økonomiske aspekter, miljø, kostnader og vedlikehold for flere marine næringer. Biologisk begroing kan begrenses ved å deponere et belegg som inneholder tilsetningsstoffer med grohindrende egenskaper. Belegg med tilsats av grafenmaterialer viser lovende grohindrende egenskaper og kan være en erstatter for de mer giftige kobberbeleggene som ofte brukes i dag. I tillegg har grafenbelegg ofte gode mekaniske egenskaper.

Det overordnede målet for denne masteroppgaven var å fremstille epoxybaserte grohindrende belegg med tilsats av grafen (G) og grafenoksid (GO), samt undersøke deres overflateegenskaper og evner til å forhindre biologisk begroing. Karakterisering av overflateegenskaper som ruhet, partikkelfordeling, mikrostruktur, kontaktvinkler og overflateenergi ble undersøkt i tillegg til de grohindrende egenskapene. Begroingen ble generert ved å senke belagte prøver i en biofilmreaktor med en algekultur som representerte et realistisk sjømiljø. En kvantifiseringsmetode basert på telling av antall kiselalger på nedsenkede prøver ved bruk av optisk mikroskopi ble foreslått. Videre ble en metode for å undersøke tykkelsen av begroingsbelegget ved bruk av fluorescensmikroskopi i kombinasjon med programvaren MATLAB lagt fram.

Sol-gel-metoden ble benyttet for å fremstille to beleggsystemer: epoksyharpiksen bisfenol A diglycidyleter (DGEBA) med tilsats av GO og epoksyharpiksen Epikote 828 med tilsats av G. En uke etter prepareringen var GO suspensjonene delvis stabile, mens G suspensjonene var stabile selv etter tre uker.

Polyetylensubstrater ble spraybelagt med de preparerte suspensjonene i to, tre og fire belegglag. Små mikrosprekker ble observert på alle de tilberedte beleggene på grunn av det høye innholdet av flyktige løsningsmidler. GO- og G-partiklene ble jevnt fordelt i de herdede beleggene. De belagte prøvene hadde en betydelig mer hydrofil karakter sammenlignet med de ikke-belagte substratene på grunn av den reduserte overflateruheten. Dermed ble den marine veksten redusert på de belagte prøvene. Ruheten til GO-belegg var litt høyere sammenlignet med de andre beleggene, noe som resulterte i en større kontaktflate mellom GO-flakene og den marine veksten. Den kombinerte effekten var sannsynligvis grunnen til at GO-beleggene hadde bedre grohindrende egenskaper sammenlignet med G-beleggene.

Den marine veksten ble redusert med økende mengde GO- eller G-innhold i beleggene. I tillegg var mengde begroing uavhengig av antall belegglag. Diatomer ble funnet til å være den dominerende begroingsorganismen på de nedsenkede prøvene, selv om det også ble observert bakterievekst. Den dominerende grohindrende mekanismen til GO- og G-beleggene var antagelig relatert til oksidativt stress. Den eksperimentelle prosedyren for generering av biofilm var vellykket, men kan forbedres ytterligere ved å øke lystilgangen og bruke en algekultur med kjent sammensetning. Siden kiselalgene ble funnet ujevnt fordelt på prøveoverflatene, kan det være en fordel med tanke på karakteriseringen av slike organismer å undersøke et større areal av prøveoverflaten. Beleggene som inneholdt 0,250 wt% GO fremsto som det optimale belegget med hensyn på overflateegenskaper og hindring av begroing. Med tanke på videre arbeid, så må de mekaniske egenskapene til beleggene undersøkes for å evaluere beleggenes marine anvendbarhet.

List of Abbreviations

AFM	-	Atomic force microscopy
ATR	-	Attenuated Total Reflection
CSA	-	Cross-sectional analysis
DGEBA	-	Diglycidyl ether bisphenol A
DSA	-	Drop Shape Analyser
EDS	-	Energy dispersive X-ray diffraction
Epikote	-	Epikote resin 828
EtOH	-	Ethanol
FIB	-	Focused ion beam
FACET	-	Functional Materials and Materials Chemistry
FTIR	-	Fourier-transform infrared spectroscopy
G	-	Graphene
GO	-	Graphene Oxide
IFM	-	Infinite force microscopy
IMA	-	Department of Materials Science
NTNU	-	Norwegian University of Science and Technology
OWRK	-	Owens-Wendt-Rabel-Kaelble
PE	-	Polyethylene
PPGBAE	-	Poly (propylene glycol) bis(2-aminopropyl ether)
rpm	-	Rounds per minute
ROS	-	Reactive oxygen species
RT	-	Room Temperature
SEM	-	Scanning Electron Microscope
TBT	-	Tributyltin
TEM	-	Transmission Electron Microscopy
TEOS	-	Tetraethyl Orthosilicate
UV	-	Ultraviolet
VOC	-	Volatile organic compound
XRD	-	X-Ray Diffraction

Table of contents

1 Background

1.1 Background

The undesirable accumulation of marine growth is called marine biofouling (hereby called biofouling) [1, 2] and is illustrated in Figure 1.1.

(a) **(b)** **(c)**

Figure 1.1: Marine biofouling can cause undesirable growth on submerged constructions as a) offshore constructions [3], b) pipelines [4] and c) farmed fish cages [5].

Biofouling can have a negative impact on several marine industries and maritime activities [6]. Marine growth occurring on ship vessels can be directly translated into increasing fuel consumption as the marine growth will result in an increase in the drag of the vessel due to increased weight and roughness [7, 8]. Furthermore, fouling organisms on ship vessels can migrate to biospheres in which they naturally do not exist and thereby disrupt the existing ecosystem [2, 9]. Marine growth is also reported to increase the corrosion rate of metals and concrete structures which arise safety concerns for marine facilities [10]. Additionally, biofouling arise as a problem for the farmed fish industry as the formation of biofilms on the cage netting will prevent the required nutrient exchange, deform the cage due to the increased weight and lower the oxygen exchange which all result in a lower fish production rate [11]. To conclude, prevention of biofouling could have a huge positive effect with respect to efficiency, maintenance and cost for a broad range of maritime industries.

Antifouling approaches as for example coatings [7], mechanical cleaning [12], electrolyzing seawater [13], UV-irradiation [14] and ultrasonic treatments [15] can be used to prevent biofouling. Antifouling coatings are commonly used to prevent marine growth as this approach appears favorable with respect to effectiveness and cost [8].

Dispersing inorganic additives as antifouling agents evenly throughout the coating matrix is a commonly used approach to achieve antifouling coatings [7, 16]. Tributyltin (TBT) has been reported as an excellent antifouling agent, but was banned in 2008 since the chemical was proven to appear toxic to non-fouling organisms [2, 8]. Copper (Cu) based antifouling coatings have also been widely used and are less toxic compared to TBT coatings, but the use of copper antifouling agents must be limited as the copper is hazardous to several non-fouling organisms with a long-term perspective [17]. Therefore, research on low-toxic and sustainable antifouling agents with excellent antifouling properties limited to the targeted fouling organisms are of great interest.

In the last decade, graphene (G) and graphene oxide (GO) have been reported as promising antifouling agents with a low degree of toxicity [18, 19]. Dispersing G or GO in the coating matrix have also improved the mechanical properties of the coating matrix [20, 21] which is an advantage for antifouling coatings in rough marine environments. Therefore, both G and GO are promising substitutes to obtain effective and more sustainable antifouling coatings with great mechanical properties.

1.2 Aim of work

The main objective of this master's thesis is to gain a better insight in the antifouling behavior of G and GO coatings. Epoxy coatings suitable for marine environments, which also exhibit antifouling properties due to additions of graphene (G) and graphene oxide (GO), will be prepared. The preparation and characterization techniques are further developed from those performed by the author during the specialization project [22].

The first objective is to prepare well-dispersed G and GO epoxy slurries suitable for spray coating deposition. CealTech AS will prepare G-epoxy dispersions, while the author will prepare GO epoxy dispersions and prepare both the GO and G slurries with suitable solvents. The sols and slurries will be characterized with respect to presence of functional groups, viscosity and stability.

In the second objective, the aim is to obtain an understanding of how additions of various G and GO content can affect the coatings with respect to coating surface properties. The prepared sols and slurries will be spray coated onto pre-treated polyethylene substrates. Furthermore, the coatings will be characterized with respect to wetting properties, surface free energies, thickness estimations, surface roughness and surface cracks.

The final objective is to investigate the antifouling properties of the coatings by submerging the samples in a biofilm reactor with algae nutrition for two and four weeks. The aim is to develop a more standardized characterization of algae growth compared to the method used in the specialization project [22]. The marine growth will be investigated using optical microscopy, fluorescence microscopy and SEM. Fouling behavior of coatings with additions of G or GO will be compared to un-coated substrates and coatings with no G or GO additions.

2 Introduction

2.1 Introduction to biofouling

Marine biofouling (hereby called biofouling) is defined as undesirable biological growth on submerged constructions in marine environments [1, 23]. Around 4000 marine species have been reported as fouling organisms and are therefore a potential contributor to the biofilm production on submerged constructions [24]. Biofouling has caused economic and environmental issues for several industries as for example shipping industry, oil and gas industry and fish farms [25].

2.1.1 Formation of biofilms

It is commonly known that almost any surface will be covered with microbial cells when being submerged in an aquatic medium [26, 27, 28]. A theory for this to occur is because substrate surfaces can be richer in nutrition compared to the bulk environment surrounding the immersed substrate resulting in attachment to the substrate surface being favorable. The community of settled cells and their possible reaction products at a surface is called a biofilm [27].

The formation of a biofilm is believed to occur in four main phases as illustrated in Figure 2.1 [29]. The first phase appear within minutes of submersion and is recognized by the formation of a reversible attached conditioning film composited of mainly proteins and protein fragments [23, 24, 29]. The second attachment phase begins after one to twenty four hours in which bacteria and unicellular organisms as diatoms start to attach on top of the conditioning film. Fouling organisms in the second phase are often labelled primary colonizers and will create a microbial film. Adsorption of primary colonizers appear due to physical forces as Brownian motion, electrostatic interaction and van der Waals forces. The microbial film are composed by dead and living cells and slime which have been secreted by the cells [29]. The diatom *Amphora* is known to easily settle on submerged substrates [30]. The third settlement phase appear after submersion time for one week and is dominated by settlement of protozoa and spores of macroalgae. Diatoms are also part of the fouling organisms appearing in the third phase. Fouling organisms in this phase are called secondary colonizers. Species belonging in the last phase will start to attach on the surfaces after two or three weeks. The biofouling occurring in the fourth phase are commonly named macrofouling and include the attachment of larvae of macrofoulers, barnacles, mussels and soft sponges which are called tertiary colonizers [29, 31].

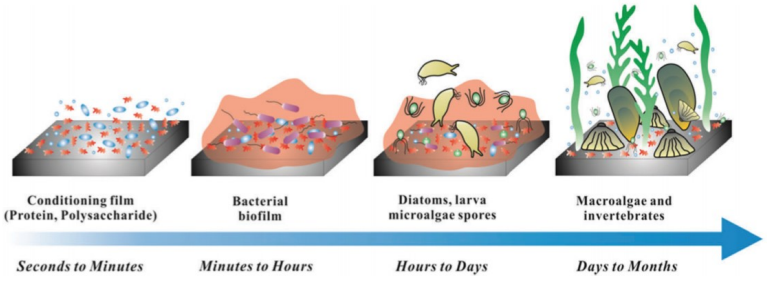

Figure 2.1: Representative illustration of the growth process of marine biofilms. The Figure is adapted from [29].

Even though there is overall good agreement with the biofilm formation time line shown in Figure 2.1, there are reported cases in which the biofilm formation phases occur in parallel, separately or overlap [1, 27, 29, 32]. For instance, tertiary colonizers as the barnacles of the type *Amphibalanus Amphitrite* have been reported to settle directly on the substrate surfaces with no present biofilm [33]. The film thickness of the biofilm will increase as more species attach to the surface or by growth of the already attached species [1, 32] resulting in a three-dimensional structure [34]. Biofilms containing diatoms have been reported as 500 µm thick [31]. Already adhered species can improve the attachment ability of other species or prevent other species from attaching [35, 36]. The accumulation of marine species do not necessarily appear constant over time or over the entire submerged surface of the substrate [27]. Investigations of biofilm structures conclude with biofilms being built up of cell agglomerates separated by voids and channels within the structure in a heterogeneous structure [24, 37].

2.1.2 Parameters affecting the biofouling

The biofilm settlement on submerged substrates are a complex process and a broad range of parameters have been reported to affect the formation and growth of biofilms on submerged constructions. Seawater parameters as temperature, salinity, composition, pH, submersion time and degree of pollution have been reported to affect the biofouling composition [2, 23, 24]. For example will diatom growth depend on the silica resources within the submersion medium [31]. Diatoms have also been reported to be able to migrate to substrate areas with the most suitable and productive environmental conditions. Some substrate areas may have the greatest availability for light or nutrients or have a lower degree of water fluctuations and thereby favor diatom growth [38].

The seawater composition and thereby the composition of the biofilm is dependent on season, hydrodynamic region, light access, nutrition supply and geographical location [25, 29, 30, 32, 36, 39, 40]. Rascio [23] and Yebra et al [2] reported significantly less fouling settlement and increased detachment respectively on ships having a speed faster than six knots. This is also in agreement with research performed by [41] who found a significant reduction in both number of diatoms and bacteria on coatings being submerged in dynamic seawater conditions compared to static conditions.

Bacteria and diatoms are the major components within biofilms in natural environments [30]. The size of diatoms do not change constantly over time. The size changes of diatoms are characterized by the two time scales lasting for a diurnal time and monthly-annual time as shown in Figure 2.2. Cell growth and division occur during the life cycle related to the diurnal time scale. The size reduction is related to reduction in length and individual cells will grow twice their minimum size before they divide into to smaller daughter cells. The life cycle lasting for a monthly-annual time period is called cell size reduction-restitution cycle. The size will gradually decrease before a relatively sudden increase of size occur until the size maximum is reached. The size changes in this life cycle is related to changes in width and length of the diatoms [42]. The time period of the monthly-annual cycle depends on environmental factors and may last for several years [43].

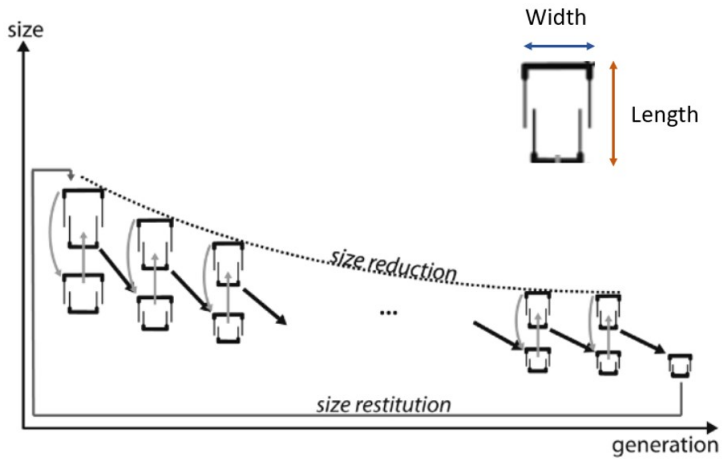

Figure 2.2: Cell size reduction of diatoms represented for diurnal life cycles (grey arrows) and monthly-annual cell size reduction-restitution cycle (black arrows). The size definitions with respect to length and width of a diatom are also included. Figure adapted from [42].

Biofouling on submerged substrates seem to a large content to depend on the physicochemical properties of the substrate rather than biological processes in a report conducted by Absolom et al. [44]. The roughness of the substrate surface has been reported to affect the formation of biofilm on submerged substrates in which rougher surfaces are more prone to biofouling [27, 45]. With a rougher substrate surface the mass transport of biological matter is believed to increase as the rough substrate surface protects small particles from shear forces and thereby increases the area available for biofouling settlement [27]. The wettability is defined as the degree in which a fluid can adhere or spread out on a surface [46] and this surface property has been linked to the biofouling behavior of the substrate [31, 47, 48]. The effect of wettability with respect to biofouling will be discussed in detail in Section 2.5.3.

2.1.3 Consequences of biofouling

The development of biofouling on submerged constructions have some undesirable consequences with respect to both economy and environment. The formation of even a thin layer of a biofilm (a hundred microns in thickness) on submerged constructions can cause severe issues related to corrosion, increased drag force and reduce the heat transfer efficiency which result in higher maintenance costs and increasing environmental emissions [27, 29, 32, 49]. For example will biofilm formation on ship hulls result in loss of energy due to the biofilm layer inducing extra mass which cause an increase in the fuel consumption [27]. A ship vessel covered with fouling species will be harder to manoeuvre and an increase in power is required to achieve the same speed as a non-fouled ship vessel [1]. Other effects of biofilm formation are reduced effectiveness of remote sensors or changes in water quality for drinking water distribution systems [27]. Biofouling occurring on a carbon steel pipe reduced the cross-sectional pipe area with 52% in only two and a half year [50] which prevented desirable waterflow through the pipeline. Fouling by macro-organisms have been reported to increase the coefficient in frictional resistance significantly compared to fouling by micro-organisms [51]. Biofouling is reported to cost the US Navy about one billion dollars each year [31]. The frictional resistance of submerged substrates have been reported to increase with more

than 10% after a submersion time of ten days due to the development of microbial films [24]. Taking the consequences presented in to consideration, prevention of biofouling on submerged construction would be favorable.

2.2 Prevention of biofouling by antifouling coatings

There are a broad range of methods to prevent biofouling like for instance coatings [7, 52], mechanical cleaning [12], electrolyzing seawater [13], UV-irradiation [14] and ultrasonic treatments [15]. Covering the submerged constructions with an antifouling coating have been reported as the most efficient way to prevent biofouling on submerged constructions [8]. By using antifouling coatings, the fuel consumption of ships related to biofouling can be significantly reduced. The world fleet of 39 000 vessels in the 1990s consumed 184 million tonnes of heavy fuel oil. If these vessels had not been coated with antifouling coatings, the fuel consumption would have been 40% higher which corresponds to a total consumption of 256 million tonnes [7].

There are several types of antifouling coatings. Coatings exhibiting vibrating properties have been reported to exhibit antifouling properties. The piezoelectric coating polyvinylidene fluoride has been reported to prevent marine growth due to vibrations [53]. Unfortunately, the use of such coatings are limited due to the large power requirements associated with the technology [2]. Fouling release coatings are another type of antifouling coatings which prevent biofouling due to their non-stick behavior. They exhibit very low surface free energies which make the bio-settlement difficult. Silicone elastomers as polydimethylsiloxane are typically used as fouling release coatings [54]. However, the fouling release behavior often require high flow conditions for sufficient prevention of biofouling [2]. Biocidal antifouling coatings contain one or more active additives called antifouling agents which exhibit antifouling properties [52] and thereby control the degree of algae growth on the constructions [29]. Biocidal coatings are commonly used in marine environments due to their effectiveness among the settlement of a broad range of fouling organisms [2].

2.2.1 Antifouling agents

There have been reported a broad range of antifouling agents which have been successfully added to several antifouling coating systems. Coatings with additions of tributyltin (TBT) have been reported as efficient antifouling coatings and were commonly used in the 1990s to prevent marine biofouling. However, these coatings caused severe damages on non-target species and were therefore abandoned worldwide in 2008 [2, 55, 56]. The disappearance of dog-whelk from coastal areas with a large boat activity has been associated with the presence of TBT [31]. Decrease in oyster larval lifetime and shell malformations in grown-ups oysters have been linked to the earlier usage of TBT in antifouling coatings [57].

Copper based materials have also been used globally as antifouling agents. However, as copper is released into the environment concerns regarding heavy metal toxicity appear [58]. As with TBT, copper has been reported to target non-fouling organisms as oysters [31]. Due to environmental concerns, more environmentally friendly and less toxic antifouling agents compared to TBT and copper are preferable for future use in antifouling coatings [49].

Antifouling agents which prevent biofilm production from a broad range of the fouling

organisms, and at the same time appear non-toxic towards non-fouling species, are of great interest. Utilizing the natural antifouling behavior of some marine species have been proposed as a way of preparing low toxic and sustainable environmental coatings [59]. Zinc based antifouling agents have also been prepared, but the antifouling behavior have been reported to be affected by salinity [60]. Graphene materials as graphene (G) and graphene oxide (GO) have been reported as low toxic [61, 62] and exhibit promising antifouling properties [62]. In addition, graphene based materials have been reported to obtain excellent mechanical properties [20]. The combination of the low toxicity, antifouling behavior and great mechanical properties of graphene based materials make antifouling coatings with additions of graphene materials highly interesting.

Introduction to G

G is a recently discovered allotrope of carbon with a hexagonal lattice structure built up by sp^2 carbon atoms as shown in Figure 2.3 [63, 64, 65]. G are the building blocks of graphite since G is a single atom layer of graphite [66]. A broad range of application areas are suitable for G due to its excellent material properties. The material exhibit a large surface area (2630 m^2/g) [67], great modulus of elasticity (1 TPa) [20], high room temperature electron mobility (250 000 $cm^2/$ V·s) [68] and a great thermal conductivity (5 000 W/mK) [69]. Mono-layers of G with no defects have been reported as "the strongest material ever measured" by Lee et al. [20]. G have also been reported as a zero-band gap semiconductor [67, 68] which makes the material exhibit no fluorescence [70].

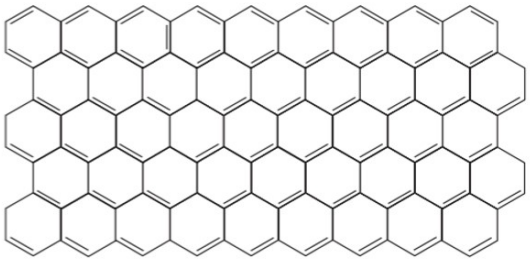

Figure 2.3: Chemical structure of graphene. Adapted from [65].

Some commonly production routes of G are chemical vapor deposition growth on metal surfaces, micro-mechanical exfoliation and exfoliation of G in solvents [67]. However, further research on G remained challenging as a large scale production of G remained difficult due to the resulting low yield and the time consuming process [63]. G like monosheets have been prepared by exfoliation of GO sheets into monosheets of GO followed by reduction of the single layered GO sheets. This latter method has the potential to be scaled up, but challenges regarding the in-homogeneity of GO resulting in generation of defects during the reduction appears as an issue [71].

Another challenge which must be overcome to reach the full potential of G, is to prepare stable dispersions of G in a broader range of solvents [67]. When dispersing G in a polymer to obtain a nanocomposite, achieving a homogeneously dispersion often appear as the main challenge. G tends to agglomerate in a polymeric matrix due to the large specific surface area and strong van der Waals interactions with other G sheets [71, 72]. However, the excellent material and antifouling properties make G a promising candidate as a more environmentally friendly and low toxic antifouling agent in marine coatings.

Introduction to GO

GO consists of a semi-aromatic network of functional groups containing oxygen with sp^2/sp^3 bonded carbon atoms as shown in Figure 2.4 [65, 73]. The basal plane of GO sheets are dominated by the functional groups hydroxyl (-OH) and epoxy (C-O-C) while carbonyl (C=O), carboxyl (-COOH) and phenol (-C_6H_6O) are commonly found at the sheet edges [63, 73]. The presence of carboxyl, hydroxyl and epoxy groups are especially beneficial with regards to stability of GO in an organic polymer matrix due to the formation of covalent bonds [74]. Their presence is also essential for the good solubility of GO in water which is estimated as 6.6 µg/mL [75].

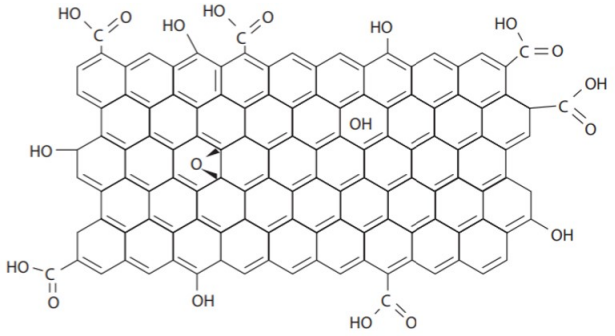

Figure 2.4: Chemical structure of graphene oxide. Adapted from [65].

The material properties of G and GO differ from each other as well. The elastic modulus of GO is about 25 % of a monolayer G [71]. GO is an insulator [76] and exhibit fluorescence [70]. However, GO is suitable for a broad range of application areas as for instance biosensors, bio-medicine, energy material for fuel cells, filtration material and gas separation [63, 71]. The chemical structure of GO is tunable and can be functionalized to enhance the spatial distribution, degree of defects, surface charge or lateral size [63].

GO can be produced by different methods, and the most commonly production routes are: Brodie method and Staudenmaier method, Hummers method and modifications of it as well as Tour method. A modified version of Hummers method which include strong acid/base treatment is commonly used today [63]. This method is beneficial with respect to large scale production, however the heavy acid/base treatment leave the prepared GO structure significantly disordered compared to the crystalline G [76].

Advantages with GO compared to G can be related to utilizing the functional groups to facilitate the dispersion stability of GO in various solvents and the scale-up ability with respect to large production volumes [63, 71]. Large scale production of G can be obtained by reduction of GO. However the resulting product exhibit a significant degree of defects within the sp^2 carbon lattice and the product is therefore referred to as reduced GO (rGO) rather than G [77]. Due to the difficulties with large scale production of graphene, investigations regarding the material properties of large scale producible GO and reduced GO are therefore of great interest [63].

2.2.2 Antifouling behavior of G and GO

Antifouling properties

Both G and GO have been reported to exhibit great antifouling properties towards bacteria growth of *E.coli* [19, 62, 78, 79, 80]. As reported by Lee et al. [81], more sufficient growth

inhibition was achieved with increasing GO content in polymeric GO dispersions. A reduction in the thickness of the biofilm layer was observed with increasing GO content using fluorescence microscopy. This indicates that a higher GO content in the coatings will result in the coating with the best antifouling properties. The antifouling properties of GO were also seen to increase with increasing lateral size of the sheets [82].

As an antifouling agent should be sustainable and only target fouling organisms, a lot of research have been performed to investigate the toxic behavior of GO and G. In research performed by Chen et al. [61], G was found to be bio-compatible and appearing harmless to living human tissue which is in good agreement with other research [83]. GO have also been reported to exhibit low cytotoxicity when being exposed to the mammalian cells [62, 84, 85]. However, the toxicity of GO has been reported to depend on dose, extent of exfoliation and sheet size [86]. More research regarding the toxicity of G and GO should be performed before their use as antifouling agents become globally available all though the present research are promising.

Antifouling mechanisms

The dominating antifouling mechanism of graphene based materials is assumed to be physical damaging of fouling cells due to direct contact with the sharp nanosheet edges [19, 62, 78, 79, 80]. The cutting of bacteria cells with the sharp nanosheets have been reported to cause osmotic imbalance which resulted in bacterial death [87]. Extraction of lipid molecules from the bacterial cells is another antifouling mechanism which appear in combination with the cutting mechanism [80, 83]. The strong interaction between G and the lipids are believed to be promoted due to the sp^2 carbons within the G sheets which result in bacteria cell viability [80]. The mechanical damage on bacterial cells due to cutting by G nanosheets have been shown using scanning electron microscopy (SEM) [87]. GO sheets have also been reported to behave antifouling when trapping bacteria cells and isolate them from the growing community. With this wrapping mechanism, the GO sheets block the active site of bacterial growth [82, 88].

The antifouling mechanism of graphene based materials are assumed to involve both physical and chemical effects. Chemical antifouling mechanisms involve introduction of oxidative stress resulting in reactive oxygen species (ROS) generation [83, 89, 90], charge transfer [91] or direct oxidation of cellular components [78]. Generation of ROS cause cell death as it induces oxidative stress which has been reported to damage cellular components as DNA, lipids and proteins within the bacteria cells [92]. Charge transfer induced by the G materials will disturb the respiration process of the bacteria which is essential to produce energy for cell growth and maintenance [91, 93, 94]. The direct oxidation of the oxidant glutathione have been proven to induce oxidative stress within the bacteria cell as unoxidized glutathione prevent cell damage of cellular components while the oxidized version do not [95].

2.3 Antifouling coating processing

The main component of a solvent-based protective coating is usually an organic polymeric resin. The function of the resin is to serve as the physical structure of the coating as well as determine the degree of ion diffusion and ultraviolet (UV) radiation through the coating matrix. Additives as antifouling agents and curing agents may also be added to the coating to improve certain coating characteristics [96]. Incorporation of nanomaterials as G and GO in a resin can enhance the antifouling properties as well as enhance the cured coating properties with respect to porosity, strength and degree of delamination. Coatings with an organic polymer as

resin and reinforcement materials in the form of nanomaterials are referred to as polymer-based nanocomposites [97]. Curing agents are often added to facilitate the bonding within the coating and reduce the curing time. A solvent is often added to un-cured coatings to serve as the carrier of the different components. However, the solvent should exist only in the un-cured state of the coating to secure complete curing and optimal hardness of the cured coating [96].

2.3.1 Preparation of organic nanocomposites

The sol-gel method is suitable for preparation of nanocomposites containing inorganic, organic or a combination of organic and inorganic polymeric structure. The principle of the method is a polymerization process which results in formation of a three-dimensional network [98]. A sol consisting of dispersed particles in a solution is forming a gel through condensation and hydrolysis processes. The gel is defined as a rigid network consisting of pores and polymeric chains [99]. Advantages with the sol-gel method is associated with low temperature processing, mild reaction conditions, achieving good bonding between inorganic and organic chemicals as well as obtaining products with a homogeneous structure [98, 100].

Organic nanocomposites are often prepared by either in situ polymerization or solution blending which are two methods to perform the sol-gel method [101]. In situ polymerization is a commonly used fabrication technique for epoxy nanocomposites [102, 103, 104] in which the nanoparticles are dispersed in the polymeric monomer before the monomer is polymerized [101]. In the solution blending method the nanoparticles are dispersed in a solvent before being mixed with the polymer monomer. Acetone and ethanol are among typical solvents used in the sol-gel process [98]. Acetone is classified as a polar aprotic solvent and ethanol as a polar protic solvent [105]. The polymer matrix and nanoparticles can develop covalent bondings through condensation reactions [101]. Addition of a curing agent into the dispersion of nanoparticles in the polymeric monomer allows for proper polymerization [101] followed up by a suitable coating deposition. Crack free coatings can be achieved by proper evaporation of the solvents from the gel which can be obtained by heat treatment [98].

The main challenge with regards to obtaining homogeneous organic nanocomposites is to obtain well dispersed nanoparticles within the coating matrix as poor dispersiability have resulted in poor homogeneity of the cured coating [104]. However, functionalization of the nanoparticle may enhance the degree of bonding between the nanoparticles and the surrounding polymer matrix [101, 106]. Sonication and intense stirring have also been reported to improve the dispersiability of nanoparticles within epoxy nanocomposites [107]. Due to the large surface area of the dispersed nanoparticles, the weight percent of nanoparticles should be less than 5 wt% to secure good dispersiability and optimize the mechanical properties of the cured coating [98, 108].

Epoxy nanocomposites

Epoxy resins are commonly used in industrial coatings because of their strong mechanical properties, good adhesion to substrate surfaces and outstanding chemical and water resistance. However, the main drawbacks with epoxy based coatings are their sensibility towards UV degradation and the poor dispersibility of nanoparticles within epoxy resins [83, 96, 104]. Bisphenol A diglycidyl ether (DGEBA) and Epikote are two commonly used epoxy resins which both arise from the chemical compound bisphenol A [96, 109, 110]. The chemical structures of DGEBA and Epikote 828 are shown in Figure 2.5.

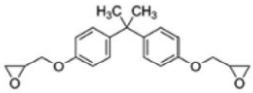

(a) Bisphenol A diglycidyl ether

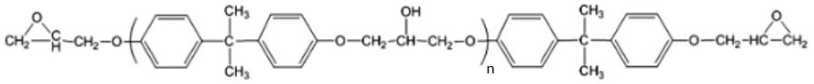

(b) Epikote 828

Figure 2.5: Chemical structures of epoxy resins of a) Bisphenol A diglycidyl ether and b) Epikote 828, n = 0.1 - 0.2. Figures are adapted from [111] and [112] respectively.

The curing agent poly(propylene glycol) bis(2-aminopropyl ether) (PPGBAE) is a diamine which have been reported as suitable for epoxy resins [96, 110]. The chemical structure of PPGBAE are shown in Figure 2.6. The primary amine groups are of special interest as these groups are assumed to yield an improtant contribution to the cross-linked polymer network which occur when mixing the epoxy resins with the curing agent [113].

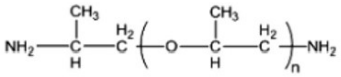

Figure 2.6: Chemical structure of the curing agent poly(propylene glycol) bis(2-aminopropyl ether) with n = 2.6. Figure adapted from [112].

The polycondensation occurring between epoxy resins and diamines during the gelation are believed to be the reactions as shown in Figure 2.7. In the first reaction, a primary amine of the curing agent reacts with the epoxide group of the resin. During this reaction the primary amine loses an H atom and thereby becomes a secondary amine. In the second reaction, branching occur in which another epoxide group reacts with the H atom in the secondary amine [114]. During the polycondensation, the cross-linking will increase which results in an increasing mechanical strength of the cured coating. However, if the degree of cross-linking exceeds a system specific limit the final coating may appear brittle as the plastic deformation is restricted [115].

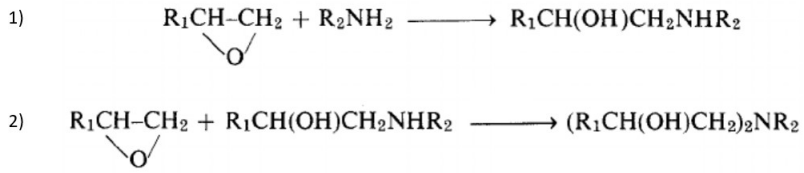

Figure 2.7: Chemical polycondensation reactions occurring between epoxy resins and diamine curing agents. Figure adapted from [113].

Nanoparticles at concentrations below 5 wt% have been evenly dispersed in DGEBA and Epikote resins resulting in coatings with increasingly mechanical strengths [71, 109, 110, 116]. Antifouling epoxy coatings have also been prepared in which the coatings containing the antifouling agents achieved better antifouling properties compared to the epoxy coatings [117].

Hybrid nanocomposites

Polysiloxane coatings are an organic-inorganic hybrid coating where a siloxane backbone have reacted with an organic resin as for example epoxy [96, 118]. Such coatings have since the 1990s been recognized for their excellent UV resistance, good adhesion strength, good chemical resistance and low volatile organic compound (VOC) content. Silicone polymers have also been reported to exhibit a non-stick behavior due to their low surface free energies which is beneficial with respect to prevention of biofouling [8, 23, 31]. Hybrid nanocomposites made of an epoxy-polydimethylsiloxane backbone with GO additives have also been reported to exhibit great antifouling properties [119]. However, the antifouling properties of polysiloxane coatings seem to be most efficient at larger water flows and are therefore not so effective in docking periods for the ships [8, 31]. The silicone polymer coatings are prone to mechanical damage due to their softness and may therefore not be suitable for marine applications if no reinforcement fillers as for instance G materials are added to the coating [8, 120, 121, 122].

2.3.2 Pre-treatment prior to coating deposition

Prior to the coating deposition, some pre-treatment of the substrate to obtain a rougher substrate profile as well as removal of dust, old paint or contamination from the substrate surface can help achieving good adhesion between the cured coating and the substrate [7, 96]. In addition, with a rougher surface profile the contact area between coating and substrate increases which is beneficial for the adhesion. A rough surface profile for the substrate can be achieved by performing dry abrasive blasting in which blasting particles are accelerated towards the substrate surface with compressed air. The mass of the blasting particles will affect the resulting surface profile of the substrate. As a result of abrasive blasting, smaller dust particles will be cut off from the blasting particles and are attached to the substrate surface by static electricity. If the dust particles are left on the substrate surface during the coating deposition, the adhesion strength between the coating and substrate will be affected negatively. Cleaning the substrate surfaces to remove the dust particles should therefore be performed prior to the coating deposition [96].

2.3.3 Coating deposition

Marine coatings are usually deposited onto large ships or constructions with challenging geometries with respect to coating deposition. Spray coating is a commonly used deposition technique within the marine industries as the method benefits from being a cost-effective method, suitable for a broad range of geometries as well as resulting in homogeneously coatings [123, 124]. However, coating slurries to be spray coated must exhibit low viscosities to be transferred out of the spray coating nozzle and onto the substrate. Therefore, the solvent content is often as high as 50-80 wt% [124, 125]. Coatings containing volatile organic compounds (VOC) are under restrictions due to the environmental effects of letting VOC out into the environment. Substances which are classified as VOCs will evaporate rapidly and are carbon-containing species. Coatings should therefore contain as low degree of VOCs as possible. Powder coatings and water-borne coatings are promising suitable coatings which have a less negatively impact on the environment with respect to emissions of VOCs [7, 124]. However, these methods may not overcome the benefits which the spray coating deposition technique offer.

Spray coating parameters as working distance, temperature, pressure and drop size can all affect the final coating properties [126]. Hand-held spray coaters may suffer from limited control of motion during the deposition which may result in uneven coating thicknesses of the cured coatings [125]. The coating thickness is adjusted by number of coating layers deposited onto the substrate.

2.4 Coating sol and slurry properties

2.4.1 Stability of dispersions

Unstable coating slurries should be prevented as agglomerated nanoparticles are harder to separate and may form a less homogeneous coating when the coating slurry is being deposited [105]. Stable dispersion of GO and G have been prepared using ethylene glycol, N,N-dimethylformamide and N-methyl-2-pyrrolidone, although partly stable dispersion have been achieved using acetone, ethanol, iso-propanol and chloroform [75]. Agglomeration of nanoparticles in a colloidal dispersion can be prevented by making use of the stabilization mechanisms shown in Figure 2.8 below [127].

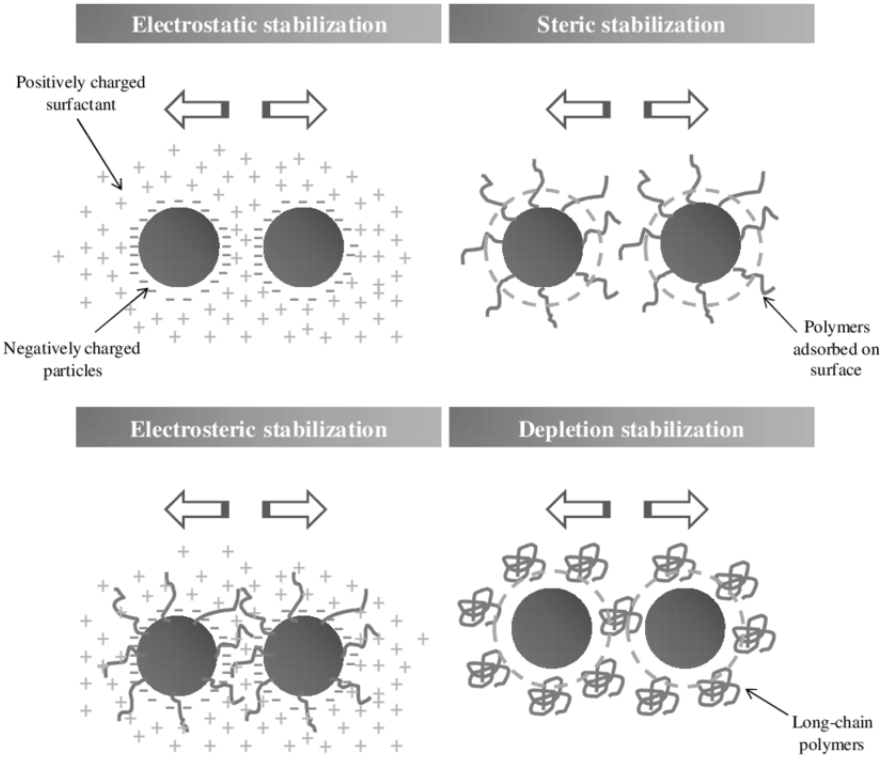

Figure 2.8: Stabilization mechanisms for colloidal dispersions. Figure adapted from [127].

Electrostatic stabilization

Electrostatic stabilization stabilizes a dispersion if the repulsive forces between particles and the solution appear larger than the attraction forces. Van der Waals forces can attract particles closer together into agglomerates and thereby result in unstable dispersions. Repulsive forces appear due to overlapping double layers between the particles which cause them to separate resulting in stable dispersions [105]. The electrical double layer existing around dispersed particles appear

due to differences in electrostatic charge between ions in the dispersion and the solid particle which cause the surrounding ions to adsorb onto the particle surface [128]. GO sheets in a dispersion exhibit repulsive forces due to the electrostatic repulsion appearing between ionized carboxylic and phenol hydroxyl groups in the sheets [129].

A schematic explanation of the electrical double layer and the corresponding electrical potential is found in Figure 2.9 [130]. The first layer is called the Stern layer and consists of ions in the dispersion being adsorbed onto the particle surface due to chemical interactions. The second layer is called the Gouy layer and is a diffusive layer consisting of free ions which movements are influenced by electric attraction and thermal motion rather than chemical interaction with the solid particle. In the Gouy layer there is a slipping plane which marks the boundary in which bulk fluid remains attached to the solid particle. The potential difference of this slipping plane and the bulk is called the zeta-potential [128]. The zeta-potential of a dispersion can help investigating the stability because it determines the interparticle forces [131].

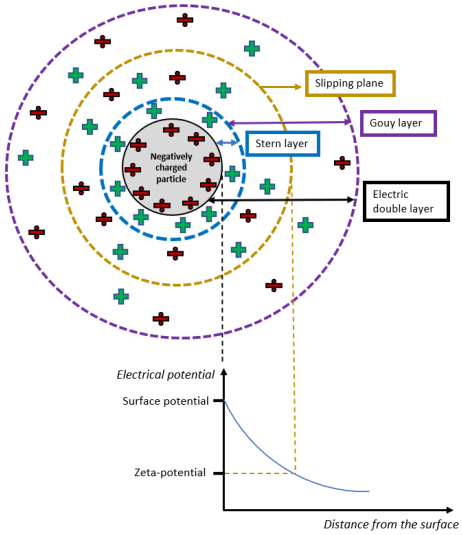

Figure 2.9: Schematic illustration of the electrical double layer of a particle in a dispersion with the corresponding electrochemical potential. Figure adapted from [130].

The stability of a dispersion increases with increasing absolute value of the measured zeta-potential. A dispersion with zeta-potentials above ± 25 mV are considered as stable [105]. Lee et al. [81] found that the zeta-potential decreased with increasing GO content in polymeric dispersions of 0.00 - 2.60 wt% GO. The absolute value of the zeta-potential will decrease with increasing ionic strength since the electrical double layer will decrease. The ionic strength is increasing with the concentration of ions in the dispersion [128]. However, the ionic strength should not be larger than about 0.1 M to secure an efficient electrostatic stabilization as ionic strength affects the double layer thickness [128]. The zeta-potential can also be altered by adjusting the pH of the dispersion. The isoelectric points is defined as the pH where particles have a zero net surface charge. By adjusting the pH far away from the isolectric point, the dispersion should become more stable as this result in an increasing absolute value of the zeta-potential and electrostatic forces dominating over attractive forces [128].

Polymeric stabilization

Steric stabilization and depletion stabilization are two polymeric stabilization mechanisms. Steric stabilization involves adsorption or attachment of polymers onto the particle surfaces

of particles in a colloidal dispersion [105]. Attachment of polymers results in a steric repulsive force due to entropy effects [128]. Expansion of the attached polymer should reduce the overall Gibbs free energy of the system which is beneficial for the stability [105]. G and GO dispersions have been stabilized with the support of steric stabilization [21, 132, 133, 134, 135, 136].

Depletion stabilization differ from steric stabilization as it stabilize a dispersion with un-attached polymers. The larger molecular weight of the polymers, the more stable colloidal dispersion as the depletion repulsion forces increases [137]. Depletion stabilization have been used to stabilize GO dispersions. The advantages with depletion stabilization is related to available particle surfaces as the polymers remain un-attached and the stability being less sensible to the ionic strength [138].

If a colloidal dispersion is dominated by polymer stabilization rather than electrostatic stabilization, the colloidal can appear stable even if the absolute value of the zeta-potential is not larger than 25 mV. Therefore, indications of stability based on the measured zeta-potential may not be realistic if polymer stabilization dominates [139].

Electrosteric stabilization

The electrosteric stabilization is the combination of the electrostatic and steric stabilization mechanisms. A polymer will be attached to a charged particle surface so that a polymer layer forms around the particle as well as an electrical potential. When two particles in a colloidal dispersion collide, repulsive forces appear due to the effect of the electrostatic repulsion and the steric repulsion [105].

2.4.2 Fluid properties

A functional barrier coating should be continuous and free from defects which require the coating to be in liquid state during the coating deposition. The fluid property of the coating slurry is a significant parameter with respect to achieving a homogeneously coating. The fluid and deform properties of a material is defined as the material rheology. The coating must be easily transferred and flow out during spray coating deposition, but should later exhibit a hold-up property to secure that the coating remains on the substrate surface rather than flowing off. Viscosity (η) is a rheology property defined as the ability of a material to resist flow. The viscosity is calculated by the following Equation [7]:

$$\eta[Pa \cdot s] = \frac{\sigma}{\dot{\gamma}} \tag{2.1}$$

The shear stress (σ) is defined as the force per unit area and will create a deformation in the fluid known by an angle which is characteristic for the shear parameter. The shear rate ($\dot{\gamma}$) is a measure of the rate a fluid is sheared or deformed during flow. The units for shear stress and shear rate are Nm^{-2} (directly transferred as Pa) and s^{-1} respectively [7]. The viscosity of water, acetone, ethanol, DGEBA and Epikote 828 are shown in Table 2.1.

Table 2.1: Viscosity values for water, acetone, ethanol, DGEBA and Epikote 828 at 20 °C [7, 140, 141].

Material	Viscosity [Pa · s]	Temperature [°C]
Water	0.0010	20
Acetone	0.0003	20
Ethanol	0.0012	20
DGEBA	4.0 - 6.0	25
Epikote	32.0	20

Fluids are often characterized as Newtonian or non-Newtonian depending on how the viscosity is affected by shear rate. If viscosity is plotted as a function of shear rate as shown in Figure 2.10, a Newtonian fluid (A) will exhibit a constant viscosity while the viscosity of a non-Newtonian fluid (B and C) will depend on the shear rate. A non-Newtonian fluid is classified as shear thickening (C) if the viscosity increases with shear rate and as shear thinning (B) if the viscosity decreases with increasing shear rate.

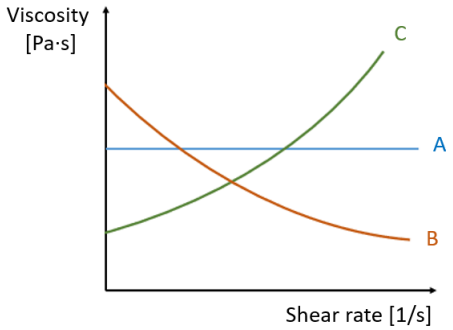

Figure 2.10: Viscosity plotted as a function of shear rate displaying A: Newtonian fluids, B: Shear thinning fluids and C: Shear thickening fluids. Figure adapted from [7].

Newtonian fluids are often simple, low molecular weight materials. Polymers and particles in a continuous phase are often found to be non-Newtonian fluids. Organic coating slurries usually contain both particles and polymers, and such coatings are often found to behave as shear thinning fluids. The degree of thinning and at which shear rate region most thinning occur is dependent on the chemical and physical properties of the materials in the coating. Shear thickening behavior is often observed for coatings containing a high content of pigment particles or other additives [7].

2.5 Cured coating properties

2.5.1 Coating adhesion

Great adhesion between the coating and substrate should occur for antifouling coatings to avoid exposure of the bare substrate which is more susceptible to biofouling. Adhesion have been reported to be affected by the surrounding environment in which submersion in water have resulted in reduced adhesion strength [142]. However, the adhesion strength of epoxy coatings was found to be recovered after the coatings had been submerged in water for two weeks which may be due to the limited water uptake reported in epoxy coatings [143]. The coating adhesion

is also affected by the chemical and physical bonds between the coating and the substrate. There are four main forces contributing to the adhesion: chemical bonds, intermolecular forces, molecular interactions and mechanical interlocking [96].

Contributions to adhesion strength

The force contributions to adhesion directly linked to the chemical nature of the coating and substrate are chemical bonds, intermolecular forces and molecular interactions. Chemical bonds can contribute to adhesion if the functional groups present in the coating are capable with those of the substrate. Therefore, there is assumed a low contribution to adhesion strength from chemical bonds if the substrate is metallic and the coating is non-metallic. The presence of functional groups as hydroxyl, carboxyl and amines in the binder have been reported to increase the chemical adhesion force. Intermolecular forces are also known as Van der Waals forces and include dispersion forces, dipole-dipole attractions and induction forces which occur between temporary dipoles, permanent dipoles and permanent dipoles and induced dipoles respectively. Molecular interactions are an intermediate contribution between the two former contributions ad are in general described as interactions between electron donors and acceptors [96].

The mechanical force contribution to adhesion strength is known as mechanical interlocking and is dependent on the surface profile of the substrate surface. Mechanical interlocking give a hook and anchor effect in which the coating clings to irregularities on the substrate surface. Nevertheless, the coating must wet the substrate surface properly to avoid voids in the interface which may reduce the coating adhesion [96]. Hagen et al [142] reported a weaker adhesion strength on epoxy coatings being coated on a smooth surface compared to a rougher surface. The adhesion is therefore dependent on both chemical and mechanical contributions as epoxy contains the functional groups which promote chemical bonds.

Adhesion may also be affected by time between the coating layer depositions in terms of drying time. If the former coating layer has not cured sufficiently before the next coating layer is deposited, the final coating will exhibit a wrinkled surface [7].

Characterization of adhesion

Currently there is no proper method of measuring the coating adhesion of a coating. However, the pull-off test (ISO 4624) is a commonly used procedure even though it usually measures the cohesion of the coating rather than the adhesion itself. The cohesion is a measurement of the attraction between the same molecules while adhesion is the attraction between different molecules [96].

2.5.2 Coating surface roughness

As explained in the former section, the substrate roughness can enhance the adhesion strength of the coating. However, the surface roughness of the coating should not be too rough for antifouling coatings. Antifouling coatings exhibiting a microscale roughness exhibited significantly more marine growth compared to coatings with a nanoscale roughness after being submerged in algae cultures [144]. Holm et al. [145] found that the rougher a coating surface becomes, the more likely biofouling is to occur and the more the overall roughness will increase. However, roughness alone can not explain biofouling behavior on different coatings as the type and size of fouling organisms have also been reported to affect the biofouling even at various roughnesses [144].

The average roughness, Ra, represents the average absolute deviation of the roughness irregularities from the baseline [146]. The average deviation from the baseline can be detected as well as the height difference between the highest and lowest valley in the detected line. Roughness measurements can be performed in a profilometer which will leave permanent damage on the coating surfaces in form of a scratch with induced stresses [96]. Non-contact measurements of roughness can be conducted in a confocal microscopy [147] or optical microscopies [30, 148].

2.5.3 Coating wettability

The wettability of coatings being submerged in marine environments are of great interest as it affects the antifouling properties of the coating as well as the contact area between the coating and the surrounding medium.

Contact angles

Contact angles (wetting angles) of a droplet deposited onto a coating surface are characteristic for the wettability of the coating [149]. The coating is classified as hydrophilic if the contact angle is less than 90 °and as hydrophobic if the contact angle is larger than or equal to 90 °as shown in Figure 2.11. Complete wetting is achieved when the contact angle is 0 °. Contact angles can be measured using sessile drop mode in a drop shape analyser [144, 148, 150, 151]. G sheets have been reported to exhibit water contact angles in the range 95 - 100 °[152, 153] and do therefore exhibit a hydrophobic surface character. GO sheets exhibit a hydrophilic surface which is assumed to be due to the functional groups containing oxygen located at the sheets [153, 154].

Figure 2.11: Liquid drop on a substance having a hydrophobic surface and hydrophilic surface. Figure adapted from [149].

The wettability of a surface is affected by the microstructure and roughness of the surface according to the Wenzel model:

$$cos\theta_a[^\circ] = r \cdot cos\theta \tag{2.2}$$

where θ_a is known as the apparent contact angle measured on a rough surface, r is the surface roughness and θ is the measured intrinsic contact angle on a planar surface [155]. However, in general the literature agrees that surfaces with a R_a value less than 0.5 µm have no significant impact on the contact angles [156]. The Wenzel model assumes that the liquid droplet completely wets the irregularities of the rough substrate which is illustrated in Figure 2.12.

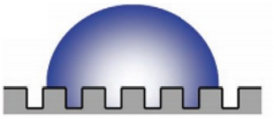

Figure 2.12: Complete wetting of irregularities on a rough surface. Figure adapted from [149].

Surface free energy

The surface free energy is defined as the excess energy associated with the presence of a surface [157]. The surface free energy is not calculated directly, but can be estimated through a set of contact angles [158]. Hydrophilic surfaces are associated with high surface free energies while the opposite matter for hydrophobic surfaces. The contact angles can be related to surface free energies by Young's Equation [159, 160]:

$$\gamma_{sv} = \gamma_{sl} + \gamma_{lv} \cdot cos(\theta) \tag{2.3}$$

where θ is contact angle and γ is the surface energy of the solid-vapor (sv), solid-liquid (sl) and liquid-vapor (lv) interface. The parameters θ and γ_{lv} are measurable, while the parameter γ_{sl} must be calculated. There are different models that can be used for the further calculation. The Owens-Wendt-Rabel-Kaelble (OWRK) model is often used. It parts the surface free energy of the solid-liquid interface into a polar and dispersive fraction [160, 161]. The polar part are associated with hydrogen bonds and permanent electron densities while the dispersive parts arise from contributions from London forces which appear due to temporary electron density variations [162, 163]. The surface free energy between a solid substance and a liquid can be calculated according to the OWRK model by solving a set of linear equations based on the measured contact angles of two different liquids. Water and 1-Bromonaphthalene are a suitable liquid combination for characterization of surface free energy by the OWRK-model [162, 164].

Relation between wettability and antifouling properties

The wettability in terms of contact angles and surface free energies of coatings have been reported to affect the antifouling properties of submerged coatings. Surface free energies of surfaces being submerged in sea water have been reported to increase with submersion time which may be related to an increase in surface roughness as biofouling occur [40].

In several reports, more biofouling have often been observed on hydrophobic surfaces (low surface free energy) compared to hydrophilic surfaces (high surface free energy) [40, 47, 81, 100, 151, 165]. A hydrophilic surface will have a lower surface-water interfacial energy and thereby resist algae growth better compared to hydrophobic surfaces [81]. However, contrary findings in which more biofouling have been seen on hydrophilic surfaces have also been reported [166]. The contrary findings may be explained by the fact that preferred settling surface seems to depend on type of fouling organisms. Diatoms have been reported to adhere well to hydrophobic substrates rather than hydrophillic ones [167]. However, the sea lettuce *Ulva* seem to prefer to settle on substrates having a more hydrophillic character [167]. Surfaces which exhibit a combination of hydrophobic and hydrophillic character are labelled amphiphilic and seem to be the optimal choice with respect to prevention of biofouling of many different species [8]. This is also in agreement with research performed by Baier [50, 168]. He suggested that the biofouling was at it lowest for surfaces having surface free energies of 20-30 mN/m and that the biofilm formation would increase with both increasing and decreasing surface free energies

above this optimum value. This phenomena is illustrated in Figure 2.13.

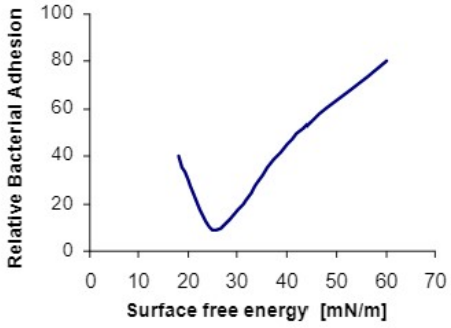

Figure 2.13: Relative biofouling as function of surface free energy. Figure adapted from [50].

2.5.4 Mechanical properties

Mechanical properties as hardness and elastic modulus of coatings are of great interest with respect to investigations of the coating durability. Rate of deformation, temperature and surrounding environment are all factors which can alter the mechanical properties of polymer coatings [169].

The hardness quantifies the ability of a material to resist permanent deformation which is usually measured by running an indenter with a given force along the coating surface [170]. Hardness may be investigated by Vickers hardness test or Martens hardness test. The measured hardness values of polymer nanocomposite coatings may be affected by time and speed of elastic recovery, limited resolution of the optical microscopy as well as size and quantity of reinforcement particles in Vickers hardness test. Martens hardness test can overcome the limitations related to the visco-elastic and optical properties of the coatings since the indention depth is measured under working load [171].

Vickers hardness are usually calculated from:

$$HV[N/mm^2] = \frac{P_{max} \cdot k}{d^2} \tag{2.4}$$

where P_{max} is the applied test force [N], k is a constant dependent on the indenter geometry [-] and d is the diagonal length of the indenter [µm] [172].

The Martens hardness, HM, is calculated from:

$$HM[N/mm^2] = \frac{F}{A_s(h)} \tag{2.5}$$

With F being the applied test force [N] and $A_s(h)$ being the surface area of indenter at a distance h from the tip [mm^2] [171].

Modulus of elasticity (Young's modulus) is usually measured with traditional tensile stress and strain tests [169] and is calculated from Hooke's law:

$$E[GPa] = \frac{\sigma}{\epsilon} \tag{2.6}$$

Where σ [GPa] is the stress applied and ϵ [-] is the corresponding strain [169].

Another mechanical property of great interest with respect to marine coatings, is the scratch resistance. During ship docking periods, marine coatings are especially susceptible to scratch formation which can cause detachment of the coating. Therefore, antifouling coatings to be used on ships should exhibit a great scratch resistance. Usually, the scratch resistance of a coating is measured in a scratch tester by dragging a stylus along the coating surface under an increasing normal force until the coating detaches [173].

2.5.5 Coating thickness

The coating thickness may affect several of the surface properties mention above. A too thin coating may result in un-sufficient wetting of the substrate surface leaving some of the bare substrate exposed. In addition, thin coatings are more likely to achieve a rough coating surface if the coating is barely covering all the substrate irregularities. As the coating thickness increases due to more coating layers being deposited, the pore content within the coating decreases. Therefore, the diffusion of ions through the coating may decrease with increasing coating thickness. Less ion diffusion through the coating matrix is beneficial with respect to water uptake within the coating and potential corrosion of the substrate beneath the coating [174]. However, the coating thickness should not be thicker than required due to unnecessarily use of chemicals and increase environmental emissions. The antifouling properties of coatings with thicknesses ranging from 0.1 mm - 2.0 mm prepared by Wendt et al. [175] were found to be independent on coating thicknesses.

Coating thicknesses may be measured with scanning electron microscopy (SEM) in combination with element dispersive spectroscopy (EDS) [176]. However, this method is used to investigate cross-sections of the coated samples which require some pre-treatment. Another limitation is related to conductivity of the coating as only conductive samples appear visible in SEM. This limitation can be overcome by sputter coating the samples with a thin layer of a conductive material [148]. Non-destructive measurements of the coating thicknesses have been achieved on organic and inorganic coatings using a coating thickness gauge [150, 174, 177] and by utilizing Raman spectroscopy [178]. The presence of GO sheets within the coating are visible with the bare eye [81] and can therefore be useful during thickness estimation based on optical microscopy [30].

2.5.6 Coating failure

During the film formation in which solvent evaporation and cross-linking occur, there will be induced internal stresses in the coating. If the internal stresses are present at a high degree, the coating may suffer from crack formation or adhesion losses. The adhesion loss occur for coatings with volatile solvents in which the solvent evaporates before the functional groups within the coating have oriented themselves into the optimal position with regards to substrate and coating matrix interaction [7]. Coating failure in terms of surface cracks can be visually inspected by SEM or optical microscopy [144].

The coating will act as if it is in tension when internal stresses are present as the coating adhere to the substrate surface. The greater this tensile stress is, the less external stress can be applied onto the coating before the coating deteriorates due to cracking or delamination [7].

The coatings may be exposed to external stresses from UV degradation, cracking, delamination, fouling, corrosion, water uptake and moisture uptake [7, 96].

Polymer surfaces are exposed to degradation when biofilms are developed on the polymer surfaces [179]. The polymer surfaces are degrading as bacteria within the biofilms attack the polymer surface [180]. Such changes in the polymer surface with respect to functional group can be investigated using FTIR analysis [40]. As new functional groups form due to bacteria attacks, the surface free energies may of the surfaces may change and thereby alter the antifouling properties of the the submerged coatings.

2.6 Characterization of antifouling properties

As have been explained in the earlier, the antifouling properties of antifouling coatings depend on coating parameters as for example surface roughness, wettability and distribution of antifouling agents. However, there are several possible methods to perform investigations and characterization of antifouling properties and some of them will be explained below.

2.6.1 Performing antifouling experiments

When performing antifouling experiments, coated samples and un-coated references are often submerged in a reactor filled with seawater and a known tribal culture of fouling bacteria or primary colonizers. Optimal conditions for the living system can be achieved by connecting circulation pumps, secure light access or apply constant stirring in the reactor. Often a bacteria or algae nutrition is added to the reactor as well to accelerate the marine growth [81], but experiments have also been performed by submersion directly in the sea [148, 181]. The salinity of seawater is usually in the range 3.3-3.8 wt% and dilution of the seawater can be performed if higher salinity levels are reached [2]. Sufficient growth to investigate the antifouling properties of the submersed samples have been achieved with submersion for five days. However, usually the submersion time is from a couple of days to several months [148, 181, 182].

2.6.2 Characterization of biofouling

There are several available method of biofouling characterization and the most suitable method will depend on fouling organisms properties as cell size, distribution, fluorescence behavior and concentration [183]. A schematic overview of the most commonly used characterization techniques for investigation of antifouling properties on coatings are shown in Figure 2.14. Some methods require some pre-treatments as cell separation and filtration while other methods can be performed directly on the sample surface.

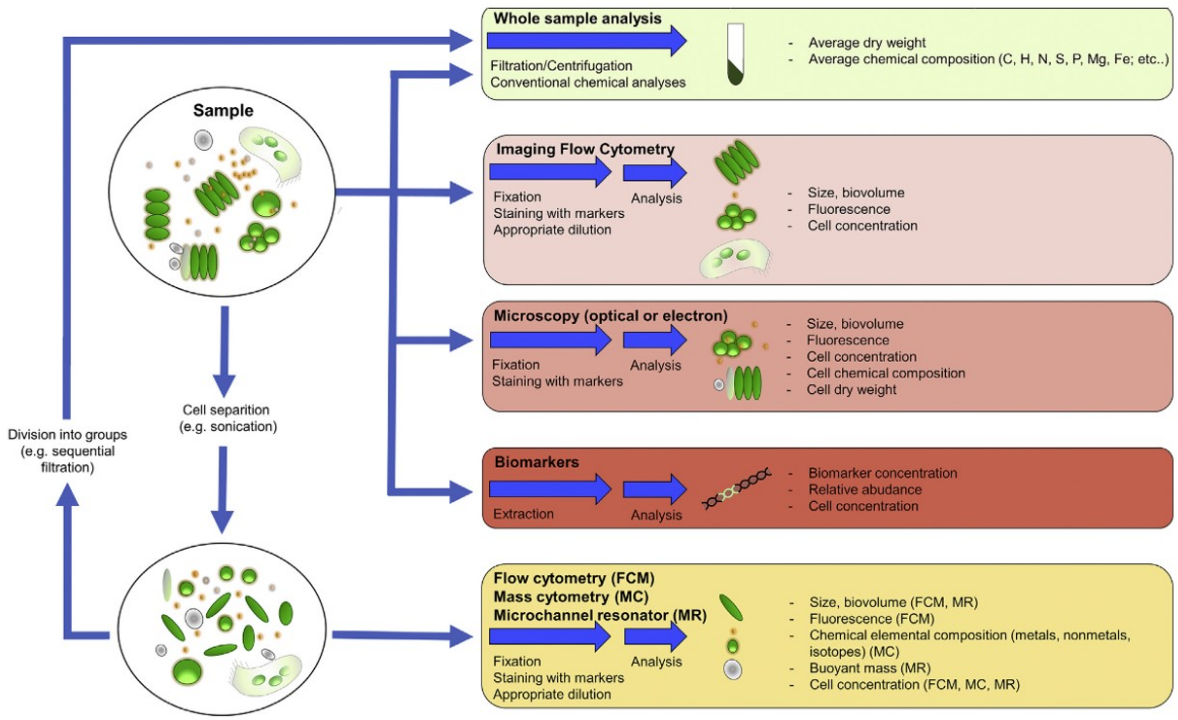

Figure 2.14: Schematic representation of present methods to analyze and investigate microbial cells of mixed populations. Figure adapted from [183].

The average dry weight of the generated biomass on the samples can be found by weighing the sample mass before and after the antifouling experiment or by scraping off the achieved biofouling followed up by centrifuging and weighing. It should be mentioned that the result include all attached matter and salt particles which limits the accuracy [183]. Utilizing washing agents can overcome the issue related to mass of salt particles [184].

With methods as optical microscopy, SEM and fluorescence microscopy, number of fouling organisms, percentage of biofouling covered area and fouling specie characterization have been estimated [32, 38, 41, 182]. These methods are in general time consuming and may suffer from some underestimations of cells if the fouling organisms prefer growing in flocs [183]. Visualizations of biofilms have been achieved by taking optical images of the sample surfaces, transforming the images into binary forms and obtaining the threshold value which makes the visualization in form of 3D mapping possible [182]. Element analysis can be performed in SEM to characterize species within the biofilm. For instance, diatoms are known for their characteristic encasement with a high degree of silica [181, 185, 186] making them suitable for characterization by element analysis.

With respect to methods as fluorescence microscopy and flow cytometry, chlorophyll itself is found in several biofilms and is naturally fluorescent which makes investigation of biofilms in fluorescence microscopy possible [32, 81]. Supplementary fluorescence proteins can be added to the tribal culture prior to the antifouling experiment to gain even more fluorescence signal within the biofilm. Thickness estimations of the biofilm can be performed using z-stacking in the fluorescence microscopy [81]. In addition, biofilm thicknesses have been performed using SEM which require preparation of cross-sections of the samples prior to the analysis [181] and optical microscopy [30].

Cytometric methods can be used to characterize cell properties of heterogeneous microbial populations as cell size, number of cells, cell morphology, cell cycle phase, DNA content and the degree of specific proteins within the biofilm. With image flow cytometry, the cells are stained with markers and thereby imaged using an optical microscopy. Nevertheless, this method is unsuitable for small bacteria or viruses. Cells to be measured with flow cytometry are often removed from the settlement surface and stained with markers. The cell size is limited to less than 50 µm. Mass cytometry is quite similar as flow cytometry, but utilizes a inductively coupled plasma detector instead of a laser detector. In general, the cytometric methods are limited by the lack of standard protocols for analysis [183].

By utilizing either genetic biomarkers (DNA) or non-genetic biomarkers (chlorophyll), the biomarker concentration or cell concentration can be estimated. The main steps for DNA biomarker analysis involves: i) sample collection, ii) sample storage, iii) DNA extraction, iv) DNA amplification, v) identification of different DNA sequences and vi) data elaboration. Microchannel resonators are microfluidic systems which can be used to investigate the dry weight of single cells. However, the latter method is relatively new and suffer from lack of standard protocols [183].

3 Experimental

A schematic overview of the laboratory work performed in this master's thesis is provided in Figure 3.1. The laboratory work is partly based on research articles, personal recommendations given to the author, work performed in the previous specialization project and master's thesis at NTNU [22, 187] and empirical research.

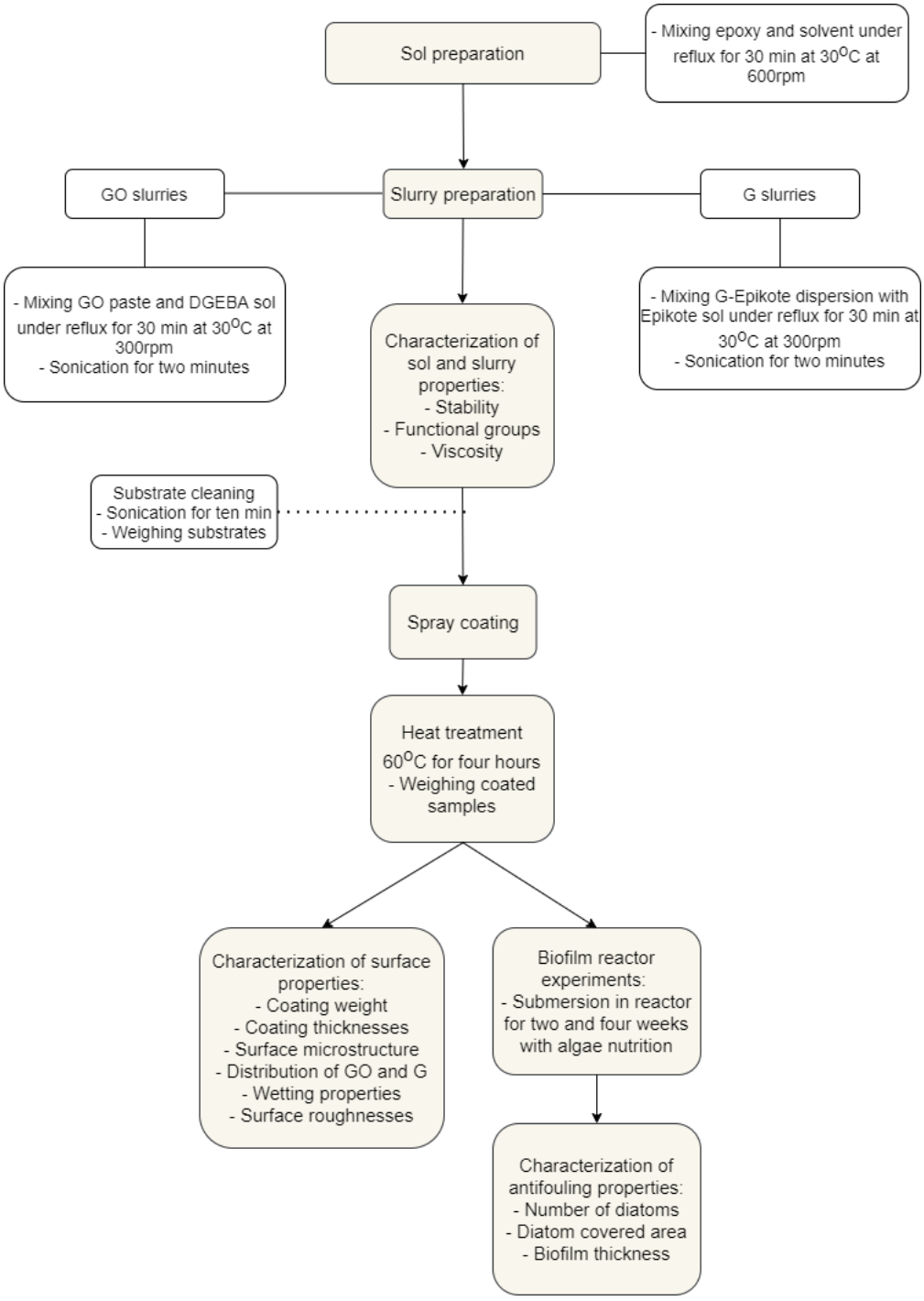

Figure 3.1: Schematic overview of the conducted laboratory work.

3.1 Chemicals and apparatus

The epoxy coatings prepared in this master's thesis were synthesized from the chemicals provided in Table 3.1 which also includes information regarding algae mediums. CealTech AS provided a Graphene-Epikote dispersion containing 0.6 wt% G and 99.4 wt% Epikote and a GO paste containing 10 wt% GO and 90 wt% aqueos mixture. SINTEF Ocean provided the algae tribal culture which consisted of primary colonizers and represented a realistic biosystem. Department of Biotechnology and Food Science at NTNU provided the silica algae nutrition medium which was stored at 6 °C. The algae culture and nutrition were used in experiments to investigate the antifouling properties. Both DGEBA and Epikote are included when referring to epoxy further on in this report.

Table 3.1: Chemical information regarding the chemicals used in the synthesis of the epoxy coatings and the nutrition medium for the biofilm reactor experiments [140, 141, 188, 189, 190, 191, 192, 193]

Chemical	Abbreviation	CAS nr.	Formula	Supplier	Function
Bisphenol A diglycidyl ether (100.00%)	DGEBA	1675-54-3	$C_{21}H_{24}O_4$	Sigma-Aldrich	Resin for GO slurries
Epikote Resin 828 (100.00%)	Epikote	68038-32-4	$C_{18}H_{21}ClO_3$	Resolution Performance Products	Resin for G slurries
Poly (propylene glycol) bis(2-aminopropyl ether) (100.00%)	PPGBAE	9046-10-0	$CH_3CH(NH_2)CH_2$-$(OCH_2CH(CH_3))_nNH_2$	Sigma-Aldrich	Curing agent
Acetone (99.00%)	-	67-64-1	CH_3COCH_3	VWR Chemicals	Solvent
Ethanol (99.97%)	EtOH	64-17-5	C_2H_5OH	VWR Chemicals	Solvent
Graphene oxide paste (10.00wt%)	GO paste	7782-42-5	$C_xO_yH_z$	CealTech AS	Antifouling agent
Graphene-Epikote dispersion (0.6 wt% G)	G-Epikote	-	-	CealTech AS	Precursor to G slurries
Silica algae nutrition medium	Algae nutrition	-	$Na_2SiO_3 \cdot 3H_2O$	Department of Biotechnology and Food Science (IBT) at NTNU	Algae growth medium
Algae tribal culture	Algae culture	-	-	SINTEF Ocean	Algae growth

Material properties of the chemicals used to synthesize the coatings are shown in Table 3.2 while the calculations for the preparation are found in Appendix A. For all preparations and chemical handling, acetone and mixtures containing acetone were extracted using glass pipettes to prevent undesirable reactions with plastic pipettes.

Table 3.2: Relevant material properties of the chemicals used to prepare epoxy coatings [140, 141, 188, 189, 190]

Chemical	Molar mass, Mm [g/mol]	Density, ρ [g/mL]
DGEBA	340.41	1.160
Epikote	184.00 - 190.00	1.160
PPGBAE	230.00	0.948
Ethanol	46.07	0.790
Acetone	58.08	0.792

An overview of the instruments used for preparation and characterization of the prepared coatings are provided in Table 3.3.

Table 3.3: Equipment used for the preparation and characterization of the prepared coatings.

Apparatus	Manufacturer	Purpose
Ultrasonic Cleaner USC-TH	VWR	Sonication of slurries and substrates prior to coating
Airbrush Double-Action Air Valve (40-9513)	Cocraft	Spray coating of slurries and sols
Airbrush Lakksprøyte 9 CC (13-001)	BILTEMA	Spray coating of slurries and sols
PF Oven	Carbolite Gero	Heat treatment to remove excess solvent
Biofilm reactor	NTNU Workshop	Measurements of coated substrates
Control unit	Heigar	Temperature control unit of the biofilm reactor
FT 200 Immersion Cooler	Julabo	Cooler connected to the biofilm reactor
GP-400 Recirculating Waterbath	Neslab	Waterbath containing the biofilm reactor
EHEIM Universial 300	EHEIM	Sea water pump in biofilm reactor
RS Pro 12V 324 mbar Water Pump 2.8 L/min (M400-S)	RS Components AS	Sea water pumps in biofilm reactor
IWAKI Magnetic Drive Pump (MD-6Z)	IWAKI Pumps	Sea water pump in biofilm reactor
Tetra Whisper 2000 Air pump	Tetra	Air pump for circulation within the algae culture
Pocket salt meter PAL SALT	ATAGO	Salinity measurements of sea water solutions
Bruker Vertex 80v	Bruker	FTIR analysis of sols and slurries
Physica MCR 301	Anton Paar	Rheology analysis of sols and slurries
Zeiss LSM 800	Zeiss	Analysis of coating and biofilm thickness and particle distribution in coatings
Sputter Coater S150B	Edwards Vacuum	Gold sputter coating of coatings prior to surface analysis
Cressington 208	Cressington	Carbon sputter coating of coatings prior to element analysis
Memmert UM 600	Memmert	Oven for degassing after sputter coating
LVFESEM, Zeiss Supra, 55VP	Zeiss	Surface analysis and element analysis of coatings
Drop Shape Analyser DSA100	Krüss	Contact angle and surface free energy measurements of coated substrates
Infinite Focus SL	Alicona	Roughness analysis and algae growth investigation
Dektak 150	Veeco	Roughness analysis of coated substrates

3.2 Preparation of sols and slurries

Two types of epoxy sols were prepared with 90 wt% solvent compared to mass epoxy: a DGEBA sol with 90 wt% acetone-ethanol (50 wt% of each component in the mixture) compared to mass DGEBA and an Epikote sol with 90 wt% acetone compared to mass Epikote. In addition, GO slurries were prepared by mixing GO paste with DGEBA sol and G slurries were prepared by diluting the received G-Epikote dispersion from CealTech with acetone.

All the chemical handling and the sol and slurry preparations were conducted in a fume hood. Furthermore, the chemicals were weighed out using a microscale weight with four decimals precision. The calculations for the synthesis of the sols and slurries are found in Appendix A. After preparation, the sols and slurries were left to cool down to room temperature for 15 minutes before being transferred to sealed glass bottles and stored at 6 °C. In addition, about 10 mL of each sol and slurries were transferred to smaller, sealed containers using glass pipettes before the stability was investigated by visual inspection one day, one week and three weeks after preparation.

3.2.1 Preparation of epoxy sols

The required masses of the chemicals needed to prepare the epoxy sols with 90 wt% solvent are found in Table 3.4. The epoxy resins and their corresponding solvent(s) were mixed by hand in a beaker using a metal spatula for two minutes. Thereafter, they were transferred to a 250 mL round-bottom flask which was placed in a water bath on a heating plate and connected to a condenser as seen in Figure 3.2. The heating plate, with a magnetic stirrer function, was placed beneath the water bath with the temperature set to 30 °C and the stirring speed set to 600 rounds per minute (rpm). The sols were prepared by mixing under reflux for 30 minutes.

Table 3.4: Required masses of components to prepare the DGEBA sol and Epikote sol.

Sol type	Chemical	Mass [g]
DGEBA sol	DGEBA	60
	Acetone	27
	EtOH	27
Epikote sol	Epikote	60
	Acetone	54

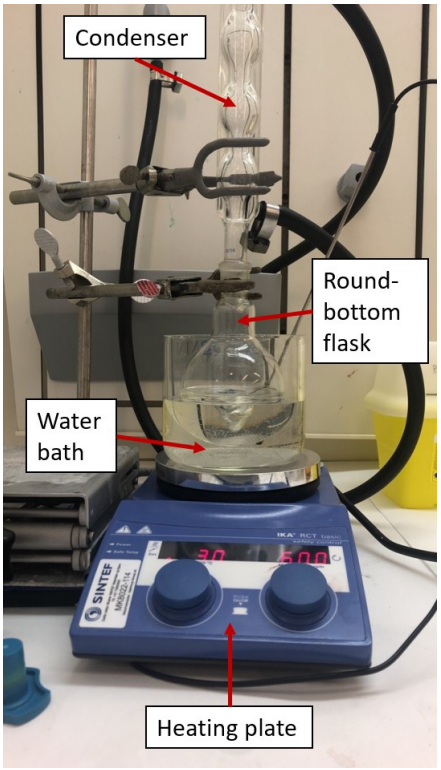

Figure 3.2: Experimental set-up for the epoxy sol synthesises.

3.2.2 Preparation of GO slurries

GO slurries containing 0.125 wt%, 0.250 wt%, 0.500 wt% and 0.750 wt% GO compared to mass DGEBA were prepared by mixing synthesized DGEBA sol with GO paste (containing 10 wt% GO). The required mass of each of the components are shown in Table 3.5.

Table 3.5: Mass of components required to prepare GO slurries containing 0.125 wt%, 0.250 wt%, 0.500 wt% and 0.750 wt% GO compared to mass DGEBA.

Weight ratio, GO/DGEBA [-]	DGEBA sol [g]	GO paste [g]
0.00125	50	0.3290
0.00250	50	0.6579
0.00500	50	1.3158
0.00750	50	1.9737

First, the DGEBA sol and GO paste were mixed together in a beaker by hand by using a metal

spatula for five minutes until only smaller fragments of GO paste were seen in the dispersion. The GO slurries were then mixed on a heating plate at 30 °C with a connected magnetic stirrer set to 300 rpm for 30 minutes. Evaporation of solvents was prevented by covering the beaker with parafilm. The experimental set-up is shown in Figure 3.3. The GO slurry preparations were completed after sonication of the GO slurries performed in *Ultrasonic Cleaner USC-TH* for two minutes to stabilize the dispersion.

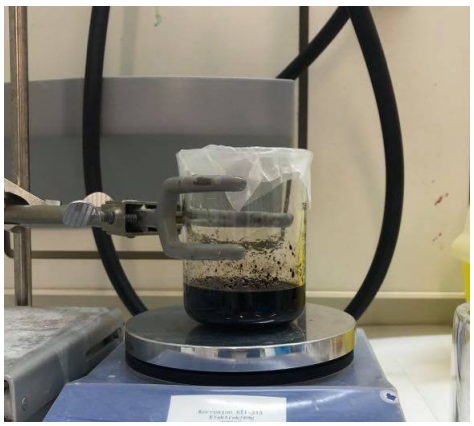

Figure 3.3: Experimental set-up for the GO slurry synthesises.

Only the 0.125 wt% GO and 0.250 wt% GO slurries were low viscous enough to be spray coated, and therefore no further work was performed on the prepared GO slurries containing 0.500 wt% and 0.750 wt% GO.

3.2.3 Preparation of G slurries

The graphene-Epikote dispersion with 0.6 wt% G compared to mass Epikote was diluted to 0.125 wt% G and 0.250 wt% G slurries by adding the required masses of Epikote and acetone found in Table 3.6.

Table 3.6: Mass of components required to prepare G slurries containing 0.125 wt% and 0.250 wt% G compared to mass Epikote.

Weight ratio, G/Epikote [-]	0.6 wt% G-Epikote dispersion [g]	Epikote [g]	Acetone [g]
0.00125	5.4825	20.8662	23.6842
0.00250	10.9649	15.4167	23.6842

The 0.6 wt% G-Epikote dispersion was first mixed with acetone by hand in a beaker. The further preparation of the G slurries was performed in a similar manner as the preparation of GO slurries described in section 3.2.2.

3.3 Procedure for spray coating deposition

Epoxy, GO and G coatings were all deposited by the spray coating procedure which will be explained in detail below.

3.3.1 Pre-treatment of substrates

Glass blast substrates of polyethylene (PE) with a diameter of 12.6 mm and height of 4 mm were customized by the fine mechanical workshop at NTNU. The parameters for the glass blasting procedure are shown below in Table 3.7.

Table 3.7: Glass blasting parameters for the preparation of polyethylene (PE) substrates.

Parameter	Description
Blasting media	Glass beads
Size of blasting media	0.18 - 0.30 mm
Gas pressure	7 bar
Working distance	150 - 200 mm

The pre-treated substrates were placed in a beaker containing ethanol before being sonicated in a *VWR Ultrasonic Cleaner USC-TH* for ten minutes. The cleaned substrates were transferred to a clean beaker filled with ethanol. The cleaned substrates were stored in the beaker sealed with parafilm and were coated within two days after the sonication. Ten minutes prior to the coating deposition, the substrates were taken out of the beaker, dried with light duty tissue wipers and left to air-dry in a fume hood. All un-coated substrates used as references in the measurements described further on in this report were also cleaned with the cleaning procedure explained in this section.

3.3.2 Coating sol and slurry batches

The required amount of each sol or slurry to prepare one layer of coating (hereby referred to as a coating batch) are shown in Table 3.8. The calculations can be found in Appendix A. The storage bottles containing the slurries and sols were placed in room temperature half an hour prior to the coating batch preparation. The coating batches were added to small sample glasses before the required volume of curing agent was added using micropipettes right before the coating deposition. To secure a homogeneous mixture, the sample glasses were hand shaken for ten seconds before being transferred to the sample holder of the spray coater.

Table 3.8: Required masses of coating sols and slurries corresponding to one coating layer.

Sol/slurry type	Mass required for one layer of coating [g]	Volume of curing agent [mL]
DGEBA sol	0.5000	0.0938
Epikote sol	0.5000	0.6829
0.125 wt% GO	0.5033	0.0938
0.250 wt% GO	0.5066	0.0938
0.125 wt% G	0.5003	0.6829
0.250 wt% G	0.5007	0.6829

It should be noted that DGEBA based batches and Epikote based batches contained the same mass of epoxy, but the number of moles was different as the epoxies have different molar mass (see Table 3.2). However, it was chosen not to adjust the batch masses to obtain the same number of epoxy moles as that resulted in the Epikote based batches exhibiting a too low volume to be spray coated.

3.3.3 Coating deposition

The glass blast PE substrates were weighed prior to the spray coating deposition on a microscale weight. Thereafter, the substrates were spray coated by filling the steel sample holder with a coating batch mixed with curing agent. The sample holder was then connected to a hand held *Airbrush Double-Action Air Valve*. A pre-treated PE substrate was placed in the middle of a 5x5 cm^2 square drawn onto an aluminium foil, as shown below in Figure 3.4, before the coating was evenly sprayed in the marked spraying area. The spray coating parameters are displayed in Table 3.9. All coated samples were spray coated within a week after the sol or slurry preparations.

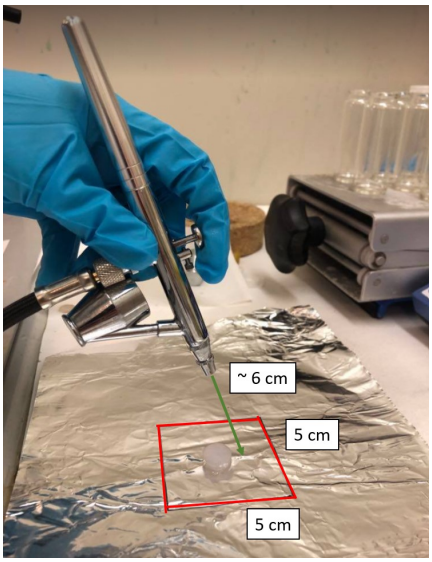

Figure 3.4: Spray coating set-up.

Table 3.9: Spray coating parameters.

Parameter	Value
Working distance	6 cm
Coating area	5x5 cm^2
Carrier gas	Nitrogen
Gas pressure	2 bar
Spraying angle	80 °

After depositing one layer of coating onto the PE-substrates, the sample was left to air-dry in a sample box for one day before the next layer was deposited. The coating deposition step and drying step were repeated one to three times until samples with two to four layers were prepared. The flow chart shown in Figure 3.5 illustrates the coating and drying procedure to achieve the desired number of coating layers. To prevent the coated substrates from being attached to the sample storage box, parafilm was left in the bottom of the sample box and possible coating material on the un-coated underside of the substrates were dried off with light duty tissue wipers. After spray coating, the spray coater was filled with acetone which were spray coated onto a paper tissue to rinse the instrument. The rinsing procedure was repeated four times.

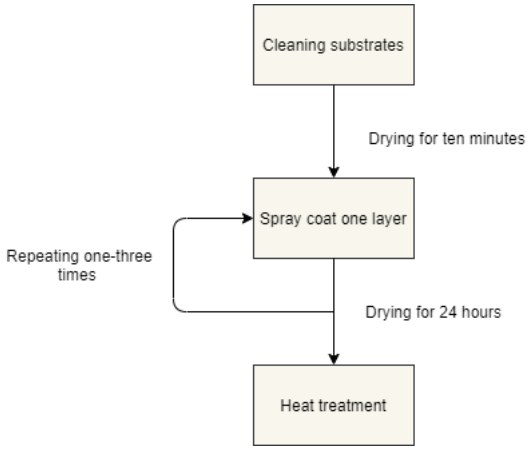

Figure 3.5: Coating procedure to prepare coated samples with two-four coating layers.

GO coatings submerged in the biofilm reactor (see section 3.4) were coated with *Cocraft Airbrush Double-Action Air Valve* with a 0.35 mm nozzle while all other coatings were coated with *BILTEMA Airbrush Lakksprøyte 9 CC* with a 0.25 mm nozzle. Two spray coaters had to be used as the spray coater with 0.35 mm nozzle became clogged and the manufacturer had stopped producing it. However, all the other instrumental parameters were the same and are given in Table 3.9.

3.3.4 Heat treatment

After the last coating layer was deposited, the coated substrates were air-dried at room temperature for one day before being placed in an alumina box and heat treated in a *PF Oven* for four hours at 60 °C. The lid was placed partially off as shown in Figure 3.6. The samples were weighed on a microscale weight with four decimals precision after the heat treatment.

Figure 3.6: Coated PE-substrates placed in an alumina box with the lid placed partially off.

3.4 Procedure for the biofilm production

To investigate the antifouling properties of the prepared coating types, two samples of each prepared coating system were submerged in biofilm reactors along with seawater, algae culture and algae nutrition. The coating system is referring to a coating type and a given number of

coating layers. A detailed explanation of the algae culture preparation, set-up of biofilm reactor and experimental procedure will be explained in the upcoming part.

3.4.1 Set-up of the biofilm reactor and algae culture

The growth inhibiting properties of the prepared coatings were tested in a biofilm reactor. The biofilm reactor was made by the fine mechanical and glassblowing workshops at NTNU with the dimensions shown in Appendix B. Samples being submerged in the biofilm reactor were placed in the sample holders of the bioreactor as shown in Figure 3.7 a).

The algae culture provided by SINTEF Ocean and the biofilm reactor were kept in a water bath as shown in Figure 3.7 b). The temperature of the water bath was kept constant at 15°C due to the connected *Julabo FT 200 Immersion* cooler, the thermostat with a *Heigar Control unit* and the plastic balls floating on the water surface. The algae culture was kept in a 2.5 L beaker. To keep the algae alive, a *Tetra Whisper 2000* air pump with air stones connected to the tube was placed in the algae culture. A glass plate was covering the beaker to limit the evaporation and thereby keep the salinity constant. A closed system was achieved by putting parafilm in the openings between the glass plate and the beaker containing the algae culture. The biofilm reactor was submerged in the same water bath as the algae culture when performing biofilm generation experiments. Sea water pumps were connected to the inlet and outlet of the biofilm reactor with plastic tubes. Metal clamps were tighten around the tube openings.

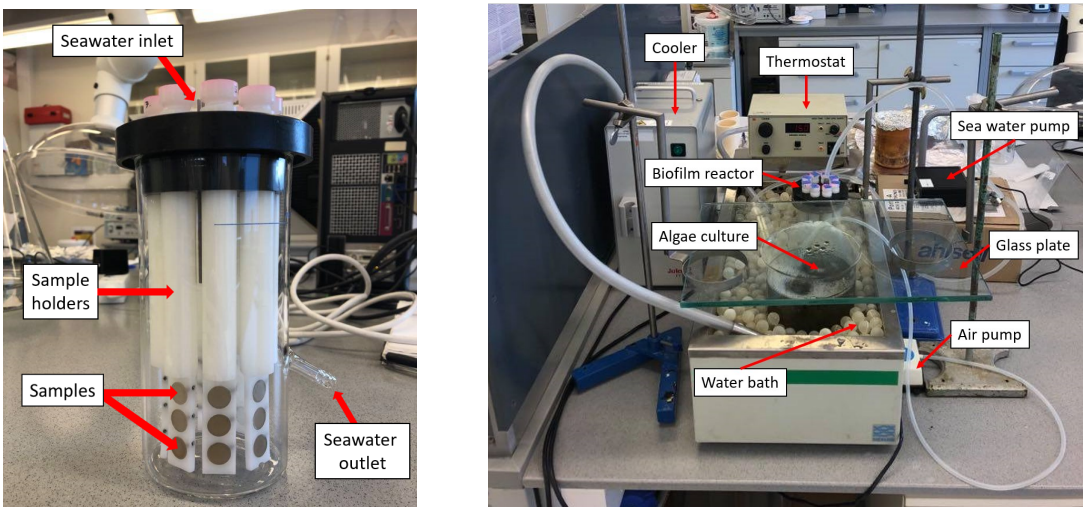

(a) Biofilm reactor with sample holders

(b) Set-up of experimental biofilm system with algae culture and a submerged biofilm reactor

Figure 3.7: The compartment of the biofilm reactor shown in a) and the experimental set-up of the biofilm reactor and the beaker containing the algae culture in b). The temperature was kept constant within the biofilm reactor and algae culture beaker due to the connected cooler and thermostat with control unit. Seawater pumps secured circulation of seawater and nutrition in the biofilm reactor. Air pumps secured water rotation within the algae culture.

3.4.2 Biofilm generation experiments

The antifouling properties of the coated samples were investigated by submerging the samples in the biofilm reactor along with algae nutrition. Two experiments were conducted so that the prepared coatings were not submerged all at once. Two samples of the DGEBA and GO coated samples with two, three and four coating layers were submerged along with two un-coated substrates. A similar experiment was carried out for the Epikote and G coatings. For each coating system and for the substrates, one of the samples were extracted after two weeks and the other one after four weeks. An overview of the two experiments performed in the biofilm reactor is provided in Table 3.10.

Several seawater pumps had to be used as some of the pumps broke down during the biofilm generation experiments. The first *RS Pro* pump used in the experiment in which GO coatings were submerged, broke down due to some electrical issues. A new *RS Pro* pump was thereafter used for the rest of the experiment. The electronic workshop at NTNU prepared a casement in which the *RS Pro* pumps were placed in. Due to the encasement, the water flow rates of the pumps could be set as 1 L/min. In the second experiment in which G coatings were submerged, the second *RS Pro* pump broke down after being used for ten days. Salt precipitation was observed within the pump casement and therefore the *Eheim* pump with a flow rate of 5 L/min had to be used until a new pump with flow rate of 1 L/min was found. The *Iwaki* pump was used for the rest of the submersion time without breaking down.

Table 3.10: Two biofilm production experiments were carried out in the biofilm reactors. Six samples (with three different coating layers) of each coating were submerged. Un-coated substrates were used as references. Half of the samples were extracted after two weeks and the rest was removed after four weeks. Different seawater pumps had to be used as they broke down during the submersion time.

Experiment	Coating system	Total number of samples # samples : # coating layers	Time submerged in reactor [weeks]	Pump type
1	Reference	2 2:0	2, 4	Day 1-10: *RS Pro* pump Day 11-12: No pump Day 12-30: *RS Pro* pump
	DGEBA sol	6 2:2, 2:3, 2:4	2,4	
	0.125 wt% GO	6 2:2, 2:3, 2:4	2,4	
	0.250 wt% GO	6 2:2, 2:3, 2:4	2,4	
2	Reference	2 2:0	2,4	Day 1-10: *RS Pro* pump Day 10-11: *Eheim* pump Day 11-30: *Iwaki* pump
	Epikote sol	6 2:2, 2:3, 2:4	2,4	
	0.125 wt% G	6 2:2, 2:3, 2:4	2,4	
	0.250 wt% G	6 2:2, 2:3, 2:4	2,4	

In each of the experiments, the biofilm reactor was filled with seawater, algae culture and algae nutrition with the volumes of each component shown in Table 3.11. The algae nutrition was extracted using micropipettes. The plastic tubes connected to the sea water pump were filled with additional sea water before the pumps were started. The algae culture in the biofilm production experiment in which the G coatings were submerged was six weeks older compared

to the algae culture used in the experiment with submerged GO coatings. After each experiment, the reactors were emptied and cleaned before being re-filled right before the start of the next experiment.

Table 3.11: Solution to be added to the biofilm reactor prior to experiments.

Medium	Volume [mL]
Fresh seawater	600
Algae culture	200
Algae nutrition	0.8

The salinity of the algae culture and solution in the reactor were measured twice a week with a *PAL SALT* refractometer. If a value larger than 4.5% had been detected, fresh water would have been added to obtain a more optimal environment for marine growth [192].

3.5 Characterization of sols and slurries

The sols and slurries were characterized with the techniques described in this part. A sample overview over which properties of the prepared sols and slurries that were characterized are shown in Table 3.12. The stabilities were observed with visual inspection as described in earlier sections (see section 3.2).

Table 3.12: Sample overview of the prepared sols and slurries displaying which properties that were characterized.

Sol or slurry type	Weight ratio epoxy/solvent [-]	Solvent	Characterized properties
DGEBA sol	0.9	Acetone-EtOH	Functional groups, viscosity, stability
0.125 wt% GO	0.9	Acetone-EtOH	Functional groups, viscosity, stability
0.250 wt% GO	0.9	Acetone-EtOH	Functional groups, viscosity, stability
0.500 wt% GO	0.9	Acetone-EtOH	-
0.750 wt% GO	0.9	Acetone-EtOH	-
Epikote sol	0.9	Acetone	Functional groups, viscosity, stability
0.125 wt% G	0.9	Acetone	Functional groups, viscosity, stability
0.250 wt% G	0.9	Acetone	Functional groups, viscosity, stability

3.5.1 Characterization of functional groups

The functional groups present within the prepared sols and slurries at different were performed using *Bruker Vertex 80v* Fourier-transform infrared spectroscopy (FTIR). The instrumental parameters are shown in Table 3.13. Two drops of each sample were deposited onto the ATR diamond using a glass pipette and were left to air-dry under a fume hood for two minutes. A background scan was performed prior to the sample scans to remove external signals. Measurements were taken one day, one week and three weeks after the sol and slurry preparations.

Table 3.13: Instrumental settings for the *Bruker Vertex 80v* instrument used to investigate the functional groups present within the prepared sols and slurries.

Parameter	Description
Spectrum mode	Transmittance
Test technique	Attenuated total reflection (ATR)
Resolution	4 cm^{-1}
Sample scan time	124 scans
Background scan time	124 scans
Measured range	350 - 4500 cm^{-1}
Aperture setting	6 mm
Detector setting	RT-DLaTGS

3.5.2 Viscosity estimations

Viscosity measurements were performed three weeks after the sol and slurry preparations in an *Anton Paar Physica MCR 301* rheometer. About 20 mL of each sol or slurry was analysed with the measurement program displayed in Table 3.14. The temperature was set to 20 °C in all the measurement steps. The measuring system consisted of the CC27 geometry and the concentric cylinder accessory.

Table 3.14: Measurement program for rheometer analysis.

Step	Measurement points	Measurement points duration	Interval duration [min]	Shear rate [1/s]
1	10	1 min	10	0
2	60	10 sec	10	1-500
3	10	1 min	10	0
4	60	10 sec	10	500-1

3.6 Characterization of surface properties

All the characterization of surface properties were performed on samples which had not been submerged in the biofilm reactor. There were only used one characterization technique per prepared sample unless something else is specified. A sample overview of the prepared coatings and which surface properties that were investigated are provided in Table 3.15.

Table 3.15: Sample overview of prepared coatings and an un-coated substrate. Surface properties that were investigated are also included. Characterization method are added in brackets if the property was measured with different methods.

Sample type	Number of coating layers [-]	Characterized surface properties
Un-coated substrate	-	Microstructure, contact angles, surface free energy, roughness (optical), roughness (profilometer)
DGEBA	2	Thickness (SEM), microstructure
	3	Microstructure
	4	Thickness (SEM), thickness (optical), microstructure, contact angles, surface free energy, roughness (optical), roughness (profilometer)
0.125 wt% GO	2	Thickness (SEM), microstructure
	3	Microstructure
	4	Thickness (SEM), thickness (optical), particle distribution, microstructure, contact angles, surface free energy, roughness (optical), roughness (profilometer)
0.250 wt% GO	2	Thickness (SEM), microstructure
	3	Microstructure
	4	Thickness (SEM), thickness (optical), particle distribution, microstructure, contact angles, surface free energy, roughness (optical), roughness (profilometer)
Epikote	2	Thickness (SEM), microstructure
	3	Microstructure
	4	Thickness (SEM), thickness (optical), microstructure, contact angles, surface free energy, roughness (optical), roughness (profilometer)
0.125 wt% G	2	Thickness (SEM), microstructure
	3	Microstructure
	4	Thickness (SEM), thickness (optical), particle distribution, microstructure, contact angles, surface free energy, roughness (optical), roughness (profilometer)
0.250 wt% G	2	Thickness (SEM), microstructure
	3	Microstructure
	4	Thickness (SEM), thickness (optical), particle distribution, microstructure, contact angles, surface free energy, roughness (optical), roughness (profilometer)

3.6.1 Coating thickness estimations

Cross-sectional analysis performed in SEM and depth range measurements in optical microscope were the characterization techniques used to investigate the coating thicknesses.

Estimations based on cross-sectional analysis

Coating thickness estimations based on cross-sectional analysis in SEM were to be performed on the prepared coatings with two and four coatings layers. A thin layer of gold had to be applied prior to the coating deposition to obtain a conductive layer between the substrate and the coating prior to the analysis. Therefore, the substrates were gold sputter coated for one minute in a *Edvards Sputter Coater S150B* before being spray coated with four coating layers of the epoxy sols, GO slurries and G slurries with the procedure explained in section 3.3. The samples were gold sputter coated again after the heat-treatment step.

The samples were placed in plastic sample holders and submerged in epoxy casting material prior to the cross-sectional analysis. Unfortunately, the sample holders tilted due to the weight of the samples during the curing time of the epoxy casting material as seen in Figure 3.8. Therefore, the grinding and polishing steps to obtain a smooth cross-section and the cross-sectional analysis itself was not performed.

Figure 3.8: Cross-sectional analysis to estimate coating thicknesses of gold-sputtered coatings were not possible to perform as the cross-sectional samples tilted during the curing of the epoxy casting material.

Estimations based on optical microscopy

Thickness estimations measured in an optical microscope was conducted as the cross-sectional analysis in SEM was not applicable. The coating thicknesses of four layer GO and G coatings with 0.125 and 0.250 wt% of GO and G were estimated using a *Zeiss LSM 800* microscopy. The coated samples were put upside down on an imaging spacer (diameter of 9 mm and depth of 0.12 mm) which were placed on cover glasses prior to the analysis. The measurements were performed using transmittance light with the Plan-Achromat 20x/0.8 objective. The thicknesses were estimated based on the depth range of the coating. The start point of the depth range was defined at the focus plane of the surface between the substrate and the coating as shown in Figure 3.9 a). The end point of the range was defined as the focus plane in which the coating no longer was in focus as illustrated in Figure 3.9 b). Five middle positions per sample were investigated and the coating thickness of each coating type was estimated based on the average value of the five measured thicknesses.

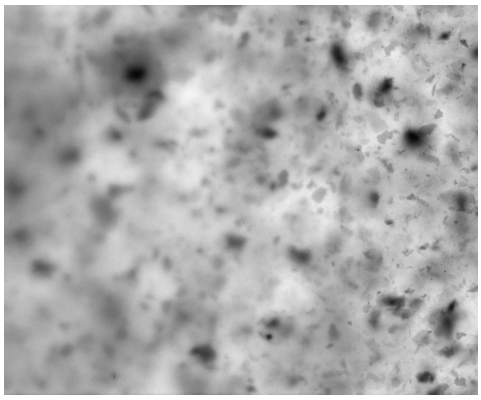

(a) Start point - surface between substrate and coating

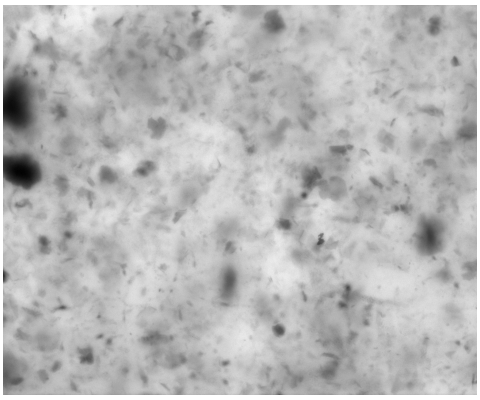

(b) End point - surface between the coating and air

Figure 3.9: Depth range with a) start position between substrate and coating and b) end position between coating and air used to estimate the coating thickness of a four layer 0.25 wt% GO coating. Start and end points were set at where the first and last GO particles appeared in focus respectively.

3.6.2 Particle distribution

The particle distribution of the GO and G particles were investigated in four layer 0.125 wt% and 0.250 wt% GO and G coatings by using transmittance light in the *Zeiss LSM 800* microscope. The objective and sample preparation were the same as explained in section 3.6.1. Images of

the particle distribution in a middle position of the coatings were captured.

Due to the fluorescent behavior of GO, the particle distribution within the GO coatings were in addition investigated using z-stacking in fluorescence mode. A blue laser (488 nm) was used with a scan speed of seven seconds. For the conducted images and z-stacks, the tile size was set as 456.4 µm x 456.4 µm, frame size of 1024 px x 1024 px and eight bits per pixel were used.

3.6.3 Investigation of surface microstructure

The non-conductive substrates coated with the epoxy, GO or G coatings and an un-coated substrate were prepared for surface topography investigation by being sputter coated with gold in a *Edvards Sputter Coater S150B* for one minute. Samples with two, three and four coating layers for all the coating types were investigated. In addition, DGEBA and GO coatings having two to four coating layers which had been coated with the *Cocraft Double-Action* spray coater were also investigated (see section 3.3.3). The substrates were covered by an aluminium foil and conductive tape prior to the sputter coating and a prepared sample can be seen in Figure 3.10.

Figure 3.10: A four layer DGEBA coated sample after being sputter coated with gold and covered in aluminum film and conductive tape prior to surface topography analysis in SEM.

The surface microstructure of the pre-treated samples were investigated by SEM-analysis performed in a *LVFESEM Zeiss Supra 55VP*. The instrumental parameters are shown below in Table 3.16.

Table 3.16: Instrumental parameters for the *LVFESEM Zeiss Supra 55VP* instrument performed on substrates coated with epoxy, GO or G coatings.

Parameter	Description
Aperture setting	30 µm
Signals	Secondary electrons
Magnification	10 000X
Accelerating voltage	10 kV
Working distance	10 µm

3.6.4 Investigation of wetting properties

Time dependency of contact angles

Changes in water contact angles over time for the prepared four layer coatings and an un-coated substrate were investigated in a *DSA25 Drop Shape Analyser* with a steel needle of diameter

0.5 mm. The measurements were performed on the coatings four weeks after preparation. One water droplet was deposited on the samples using sessile drop mode with a 0.5 mm steel needle with a delaying time of 15 seconds. The dosing volume was set as 2 µL with a dosing rate of 2.7 µL/s. The baseline was adjusted manually. The contact angle of the water droplet was measured every minute for ten minutes after the drop deposition. The time dependency of the contact angles could not be measured by using the *DSA100 Drop Shape Analyzer* due to ventilation work.

Estimation of contact angles and surface free energies

Contact angles and surface free energies of coated substrates and an un-coated substrate were estimated using sessile drop mode in a *DSA100 Drop Shape Analyser* with the procedure described in Table 3.17. All measurements were performed on the coatings six weeks after the preparation. Step four (Position syringe for deposition) was delayed with 15 seconds. The baseline was set automatically and a steel needle with diameter 0.5 mm was used.

Table 3.17: Set-up for the automation program used in a *DSA100 Drop Shape Analyser* on the prepared four layer coatings and an un-coated substrate.

Step	Action	Additional step information
1	Position syringe	Position: Standby, Speed: 320 mm/min
2	Position syringe	Position: Deposition, Speed: 320 mm/min
3	Dose	Volume: 2 µL, Rate: 2.7 µL/s
4	Position syringe	Position: Deposition, Speed: 320 mm/min
5	Position syringe	Position: Standby, Speed: 320 mm/min
6	Multiple measurement	Time: 10 seconds, Frequency: 1 fps

For each sample, the contact angle between water and coating was first estimated at a middle position of the sample before the water drop was carefully dried off. The contact angle between 1-Bromonaphtalene and the sample was then estimated at another middle position of the sample. The surface free energy was calculated based on the measured contact angles using the Advance-software of the instrument.

3.6.5 Roughness investigation

Roughness measurements were performed with two different methods: optical measurements in an optical microscope and physical measurements in a profilometer.

Optical roughness measurements

Optical roughness measurements were performed in an *Alicona Infinite Focus SL* microscope with a magnification lens of 10X. Four layer epoxy, GO and G coatings as well as an un-coated substrate were measured. Both polarizer and ring light were checked off as light sources in the control panel and the measurement type was set as 3D Dataset. First the surface focus plane was defined and set as the focus reference point before the first and last set points were defined in the upper and lower focus planes of the samples.

Roughness measurements were performed on the obtained images using the module "ProfileRoughnessMeasurements" at three middle positions per sample. The software setting type was set as mean while the measured width (number of profiles) was set as 15. In addition, roughness filtering was used.

Physical roughness measurements

Roughness measurements were also conducted on the same coatings in a *Dektak 150* profilometer. Three measurements at three middle positions on the samples were performed in the profilometer with the instrumental parameters are shown in Table 3.18.

Table 3.18: Instrumental parameters for roughness measurements performed in a profilometer.

Instrumental parameters	Value
Scan type	Standard scan
Stylus radius	12.5 µm
Scan length	2 000 µm
Scan duration	60 seconds
Resolution	0.111 µm/sample
Force	3.0 mg
Measurement range	524 µm

3.7 Characterization of biofilm production

The marine growth produced on the samples being submerged in the biofilm reactor (see section 3.4.2) was investigated with the characterization techniques explained in this section. An overview of which parts of the marine growth that were characterized on the submerged samples are found in Table 3.19. The characterization was performed on evaporated samples as the samples were investigated in the range one hour to two months after the samples had been extracted from the reactor.

Table 3.19: Overview of which parts of the marine growth that were investigated on the samples being submerged in the biofilm reactor to generate biofilms.

Sample type	Number of coating layers [-]	Marine growth characterization
Un-coated substrate	-	Two weeks: Marine growth, number of diatoms, diatom covered area, biofilm thickness, element analysis Four weeks: Marine growth, number of diatoms, diatom covered area
DGEBA, 0.125 wt% GO 0.250 wt% GO, Epikote, 0.125 wt% G and 0.250 wt% G	2	Two weeks: Marine growth, number of diatoms, diatom covered area Four weeks: Marine growth, number of diatoms, diatom covered area
	3	Two weeks: Marine growth, number of diatoms, diatom covered area, biofilm thickness Four weeks: Marine growth, number of diatoms, diatom covered area
	4	Two weeks: Marine growth, number of diatoms, diatom covered area, element analysis Four weeks: Marine growth, number of diatoms, diatom covered area

3.7.1 Estimation of marine growth on submerged samples

Marine growth in the algae culture and on the samples being submerged in the biofilm reactor was investigated in an *Alicona Infinite Focus SL*. Lateral and vertical resolution was adjusted with respect to optimal resolution for each sample. Images with a magnification of 10X and 50X were taken to investigate the observed marine growth.

Investigation of marine growth in the algae culture

Prior to the start of the biofilm reactor experiments, the marine growth in the algae culture was investigated in the optical microscope. Ten droplets of the algae culture was placed beneath the optical microscope lens of 10X using plastic pipettes before images were captured.

Estimation of number of diatoms and percent diatom covered area

The diatom growth on all the samples being submerged in the biofilm reactor were investigated in the optical microscope. The characteristic morphology of the diatoms were used to investigate the diatom growth at twelve evenly distributed middle positions per sample as shown in Figure 3.11. The measurements were performed by using a lens with magnification of 10X corresponding to a measurement area on the samples of 4.17 mm^2. For each position, number of diatoms were counted before an image was captured. The area of each diatom in the image was found by using the area estimation tool in the microscope. The average number of diatoms and average diatom covered area was calculated from the twelve measurement positions per sample.

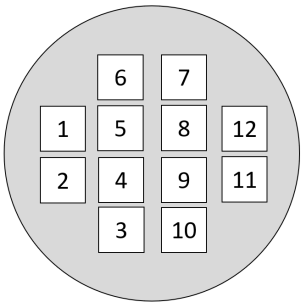

Figure 3.11: Illustration of the twelve middle positions where diatom growth was investigated on all the samples which had been submerged in the biofilm reactor.

3.7.2 Confirmation of marine growth

The different species in the produced biofilms growing on four layer epoxy, GO and G coatings as well as the un-coated substrates being submerged for two weeks were investigated by using element analysis in SEM.

Pre-treatment with carbon sputter coating

Prior to the element analysis performed in SEM with Energy dispersive X-ray Diffraction (EDS), the samples were covered with aluminum foil and conductive tape as described in section 3.6.3. Thereafter, the samples were carbon sputter coated in a *Cressingtion 208 Carbon Sputter Coater* for eight seconds with a voltage set to 5 V. The procedure was repeated two more times with a rest of ten seconds in between each sputter coating. After the sputter coating, the samples were left for degassing in a *Memmert UM 600* oven at least one hour prior to the element analysis.

Element analysis

Element analysis of the coating surfaces were performed in SEM with EDS-analysis after the samples had been carbon sputter coated. The instrumental parameters for the SEM-instrument and EDS-analysis are shown in Table 3.20.

Table 3.20: Instrumental parameters to perform element analysis by EDS-analysis in SEM on carbon sputter coated samples. The samples were un-coated substrate and four layer epoxy, GO and G coatings which had been submerged for two weeks. SEM instrumental parameters are described above the dashed line and EDS parameters are shown below.

Instrumental parameter	Value
Working distance	10.5 mm
Accelerating voltage	5 kV
Signal	Backscatter electrons
Aperture setting	120 µm
High current	On
Analysis mode	Point analysis
Number of points	Five
Frame size	1024 µm x 800 µm

Element analysis was performed on three middle positions per sample. All the particles or objects observed at each position were analysed. Carbon was removed from the resulting element spectra since all the samples had been carbon sputter coated prior to the analysis. SEM-images of the three investigated positions per sample were also captured.

3.7.3 Investigation of biofilm thicknesses

The average thickness of the biofilms produced on the three layer epoxy, GO and G coatings in addition to un-coated substrates being submerged for two weeks were estimated using *Zeiss LSM 800* confocal microscope in transmittance light and fluorescence mode. The same instrumental settings as described in section 3.6.2 were used. Three positions with algae growth of each sample were investigated first in transmittance light and then by fluorescence. An image of each position was taken when the transmittance light mode was used while z-stacks were created when using fluorescence. The beginning of the z-stack was set to the point where the first fluorescence response was observed and the last z-stack was set to the point where no fluoresce occurred. The Z-stack was saved as a czi-file and converted to a topographic image using ImageJ and MATLAB (see detailed description in Appendix C). The biofilm thicknesses were estimated at three different positions per sample.

As both the GO particles and the algae growth observed in the biofilm appeared fluorescent, the ending point of the biofilm was first found in transmittance light mode at where there were observed salt particles. The starting point was found using fluorescence microscopy and was set at the focus plane in which only GO particles and not marine growth yielded fluorescent signals.

4 Results

4.1 Characterization of sols and slurries

The sol and slurry properties as stability, functional groups and viscosity are of great importance as they will affect the final properties of the cured coatings. Therefore, such properties were measured and are characterized in the following part.

4.1.1 Stability analysis

The stability of the prepared sols and slurries were investigated by visual inspection and the stability results are seen in Figure 4.1. The GO slurries appear partly stable one week after preparation while the sols and G slurries appear stable. The stability did not change after one week for any of the sols or slurries.

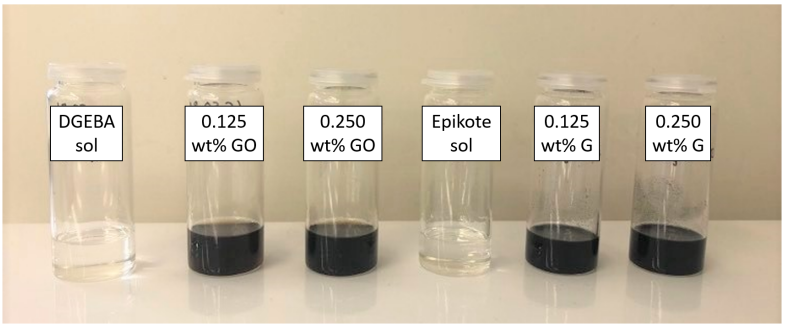

(a) One day

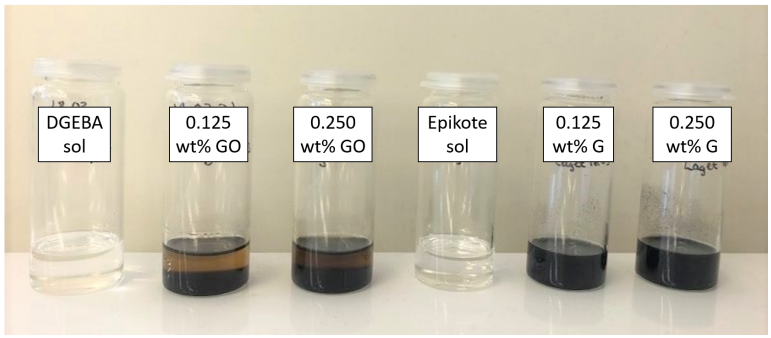

(b) One week

Figure 4.1: Visual inspection of GO and G slurries and epoxy sols at a) one day and b) one week after preparation.

4.1.2 Characterization of functional groups

Functional groups within the prepared sols and slurries were investigated using FTIR analysis and the resulting transmittance spectra are investigated in this part. The transmittance spectra of the epoxy sols and the pure epoxies are shown in Figure 4.2. A great overlap between the transmittance spectra is observed which is expected as both DGEBA and Epikote are types of bisphenol-A epoxies [194]. Differences in baseline are related to instrumental variations and

do not affect the peak positions. The most significant observed peaks and their attribution are shown in Table 4.1. The greatest difference is observed at the peak with a wavenumber of 1710 cm^{-1} as only the Epikote sol exhibits a transmittance spectra for this peak. The peak has been observed in other Epikote epoxies as well [194] and it corresponds to the vibration of the carboxyl group (-COOH) [195].

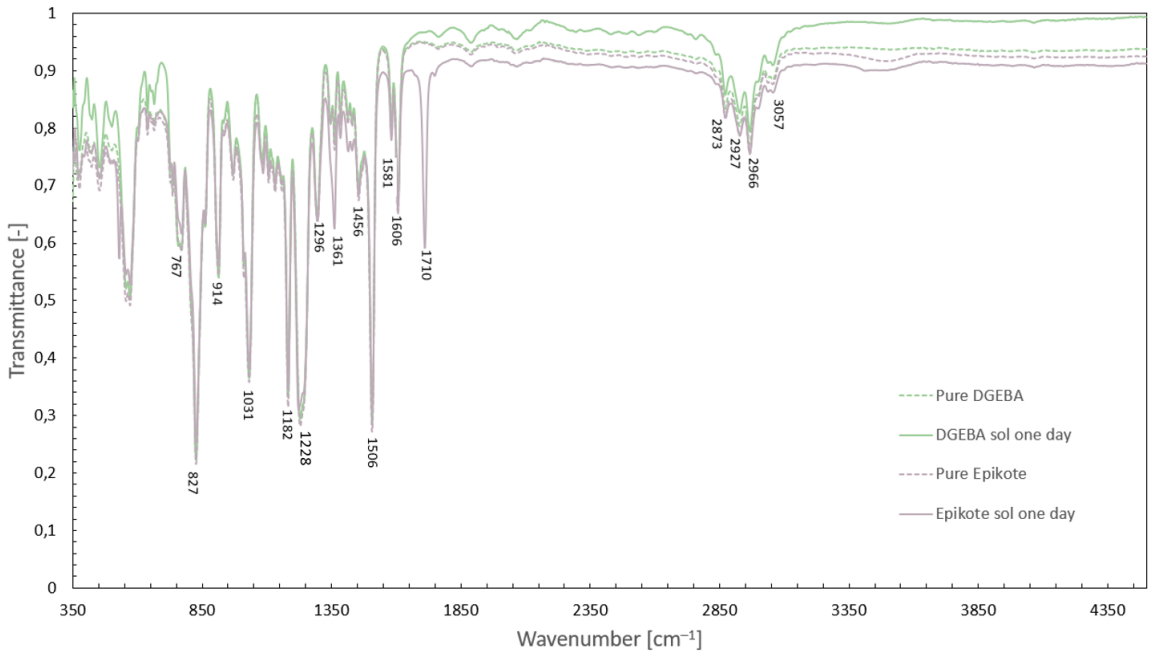

Figure 4.2: Comparison of the transmittance spectra of epoxy sols one day after preparation and pure epoxies.

Table 4.1: Wavenumbers and their corresponding attribution with respect to functional groups present within the prepared sols and slurries. Attribution explanations: γ: out-of-plane bending vibration, δ: in-plane bending vibration, ν: stretching vibration or elongation bond vibration [194, 195, 196, 197].

Wavenumber [cm^{-1}]	Attribution [-]
767	γCH_2 and γC-H of disubstituted benzene
827	γC-H for the disubstituted benzene and γCH_2 of the epoxide group
914	ν_{asym} of epoxide ring
1031	δC-H of disubstituted benzene and ν_{asym}C-O-C of aromatic ether
1182	δC-H of benzenic
1228	Vibration of -COOH
1296	γ CH_2 (wagging) and γ CH_2 (twisting)
1361	$\delta_{sym}CH_3$ doublet of gem-dimethyl groups
1456	δ CH_2 (scissoring), δ_{asym} CH_3 and νC=C of disubstituted benzene
1508, 1581 and 1606	νC=C of disubstituted benzene
1710	Vibration of -COOH
2873, 2927 and 2966	νC-H aliphatic
3057	νC-H aromatic
3211 - 3533	Vibration of -OH and H_2O

The sol compositions are assumed to be constant over time as only minor variations with

respect to the functional groups are observed as shown in Figure D.1 in Appendix D. In comparison, greater differences with respect to composition variations over time are observed for the prepared GO and G slurries as shown in Figure 4.3. The most significant changes are observed at the peaks with wavenumbers corresponding to 1710 cm^{-1} (-COOH groups) and in the area 3211-3533 cm^{-1} (-OH groups and H_2O) [198, 199, 200, 201] for the slurries. For both the GO and the G slurries, the slurry compositions appeared unchanged after three weeks.

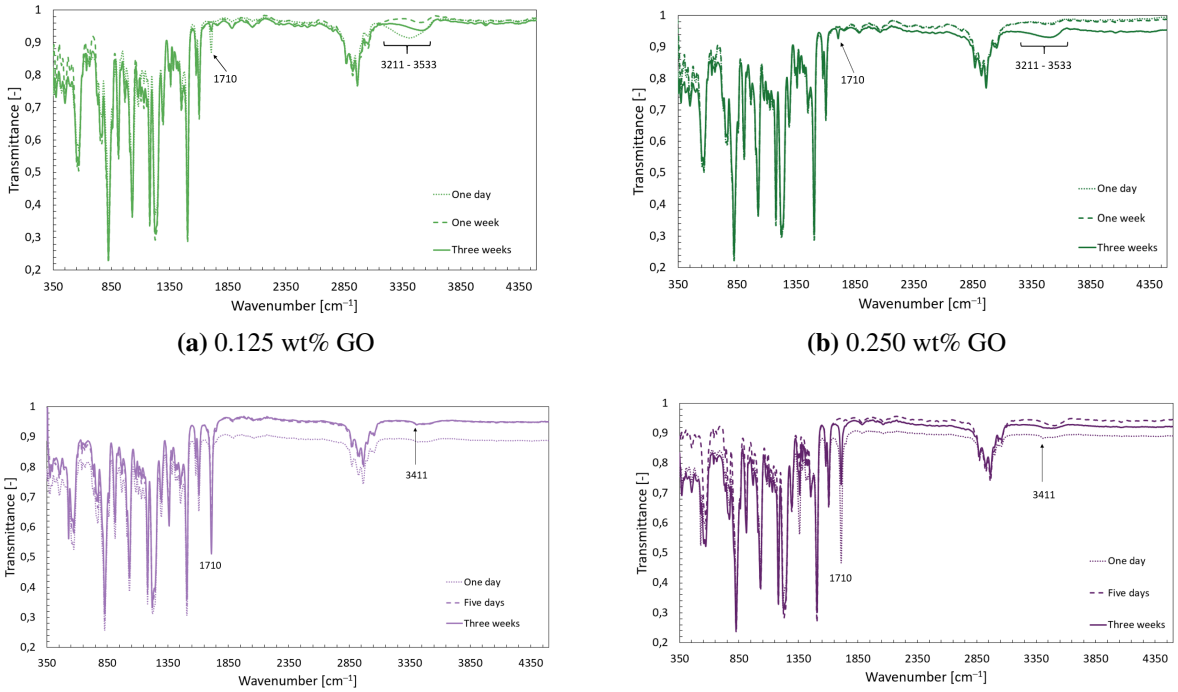

(a) 0.125 wt% GO

(b) 0.250 wt% GO

(c) 0.125 wt% G

(d) 0.250 wt% G

Figure 4.3: Transmittance spectra for GO and G slurries at different time periods after the slurry preparation. The most significant differences are observed around the peak at 1710 cm^{-1} and 3211-3533 cm^{-1} corresponding to -COOH and -OH respectively.

For the 0.125 wt% and 0.250 wt% GO slurries in Figure 4.3 a) and b) respectively, the -OH group (see Table 4.1) appears more significant three weeks after preparation compared to one week after preparation. The peak observed at 1710 cm^{-1} which corresponds to -COOH groups is not transmitted one week after preparation for both GO slurries, but appear transmitted three weeks after preparation. The 0.125 wt% GO coating had more significant peaks for both the -COOH and -OH group one day after preparation compared to the 0.250 wt% GO slurry. However, within three weeks the -COOH and -OH groups existed at similar significance for both the GO slurries.

The transmittance spectra of the G slurries shown in Figure 4.3 c) and d) exhibit only a weak transmittance peak for the -OH group at all time periods. The -COOH peak at 1710 cm^{-1} is present at all time periods in the 0.125 wt% G slurry, but is not transmitted in the measurement performed on the one week 0.250 wt% G slurry. In spite of that, the -COOH peak is present in both the 0.125 wt% and 0.250 wt% G slurries one day and three weeks after preparation.

The transmittance spectra of three weeks old GO and G slurries and epoxy sols are shown in Figure 4.4 with only wavenumbers with significant peak differences shown. At 1710 cm^{-1} only the DGEBA sol yields no transmittance. Some differences in transmittance spectra are

observed in the broad peak around 3211-3533 cm^{-1} in which the GO slurries exhibits a deeper peak compared to the other slurries and sols. This is in agree with earlier research performed by the author [22] and the literature [198, 199, 200, 201] as a broad peak corresponding to -OH groups or water often are observed for GO dispersions.

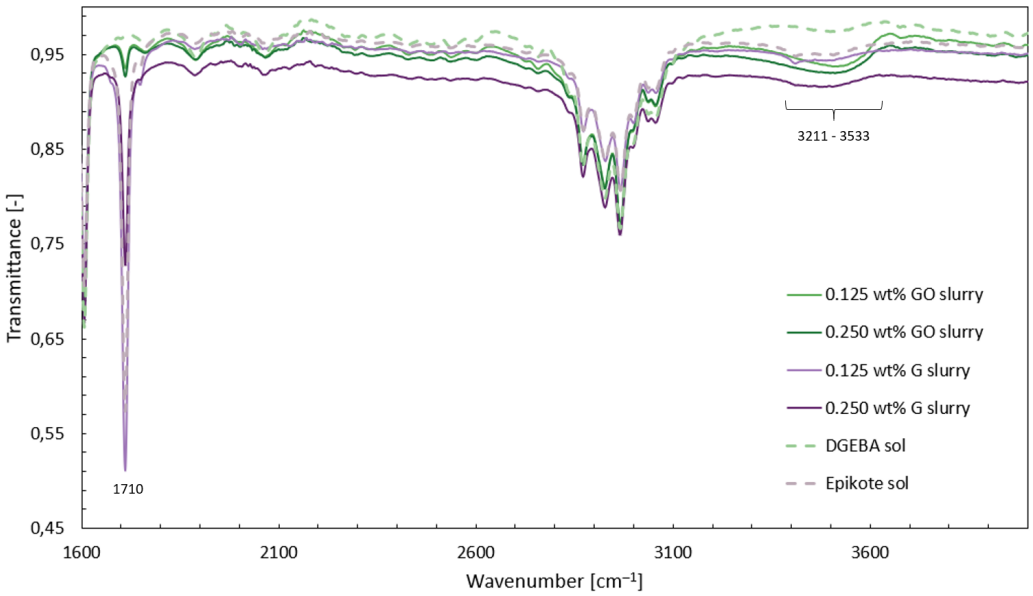

Figure 4.4: Comparison of functional groups within the epoxy sols and GO and G slurries three weeks after preparation.

The complete measured transmittance diagrams for the three weeks old slurries and sols are shown in Figure D.2 in Appendix D. There are observed no differences in functional groups at wavenumbers below 1710 cm^{-1} for all the slurries and sols.

4.1.3 Rheological properties

Fluid properties

The fluid properties of the prepared slurries before curing agent addition seem to be dependent on type of particle as shown in Figure 4.5 in which shear stress is plotted as a function of decreasing shear rates. Shear rates larger than 320 s^{-1} are not included as these shear rates resulted in extreme non-laminar flows seen as sudden increase in measured shear stress. DGEBA sol, Epikote sol and the GO slurries have a Newtonian flow behavior while the G slurries behave as shear-thinning fluids due to their changes in viscosity with shear rates [7].

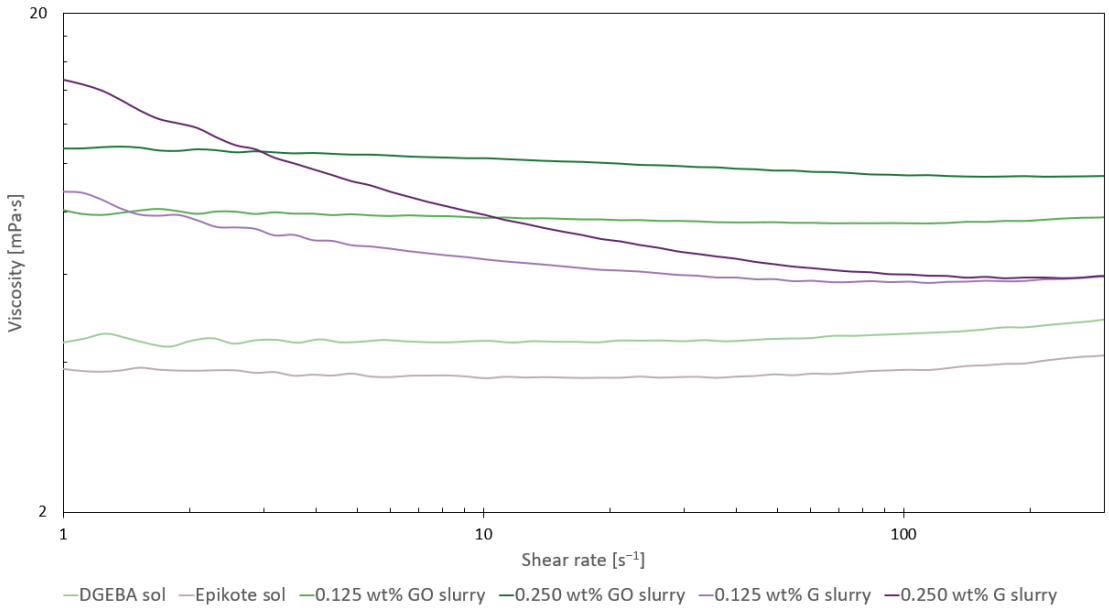

Figure 4.5: Fluid properties of the prepared sols and slurries measured three weeks after preparation and prior to addition of curing agent. The epoxy sols and GO slurries behave as Newtonian fluids, while the G slurries behave as shear-thinning fluids [7].

Viscosity estimations

Viscosity estimations were obtained by performing linear regression of the shear stresses plotted as a function of decreasing shear rates (see Appendix E) and the resulting estimations are shown in Table 4.2.

Table 4.2: Viscosity estimations of prepared sols and slurries based on linear regression of shear stress as a function of decreasing shear rates (shown in Appendix E). The uncertainties are found by the R^2 values of the linear regression.

Fluid	Viscosity [mPa · s]
DGEBA sol	4.8 ± 1.0
Epikote sol	4.1 ± 1.0
0.125 wt% GO	7.8 ± 1.0
0.250 wt% GO	9.4 ± 1.0
0.125 wt% G	5.9 ± 1.0
0.250 wt% G	5.9 ± 1.0

The DGEBA sol and the GO slurries had higher viscosities compared to the Epikote sol and the G slurries respectively. Greater difference in viscosity with respect to increasing antifouling agent content is observed for the GO slurries compared to the G slurries. There are a larger viscosity difference between the GO slurries and the DGEBA sol compared to the Epikote sol and the G slurries.

4.2 Characterization of coating surface properties

Investigation of the surface properties of the cured coatings are of great importance when investigating if the prepared coatings are suitable in marine environments. In addition,

the surface properties may alter the antifouling properties of the cured coatings. Proper characterization of the surface properties is therefore beneficial with respect to the investigation of antifouling properties.

4.2.1 Coating weights and thicknesses

Investigation of the coating extent on the substrates with respect to weight of coatings and thickness estimations are presented in the upcoming part.

Coating weights

The weight differences between un-coated substrates and coated samples after heat treatment are displayed in Figure 4.6. As expected, there is a clear trend in which the coating differences increases with an increasing number of coating layers deposited onto the substrates. This overall trend is seen for all the coatings.

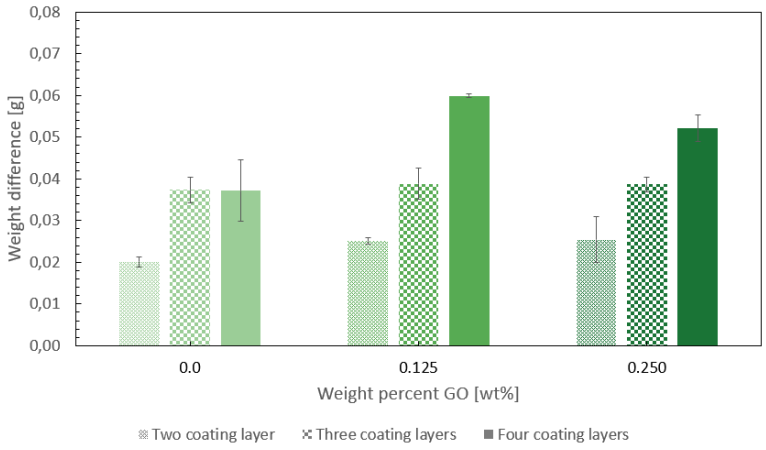

(a) GO coatings

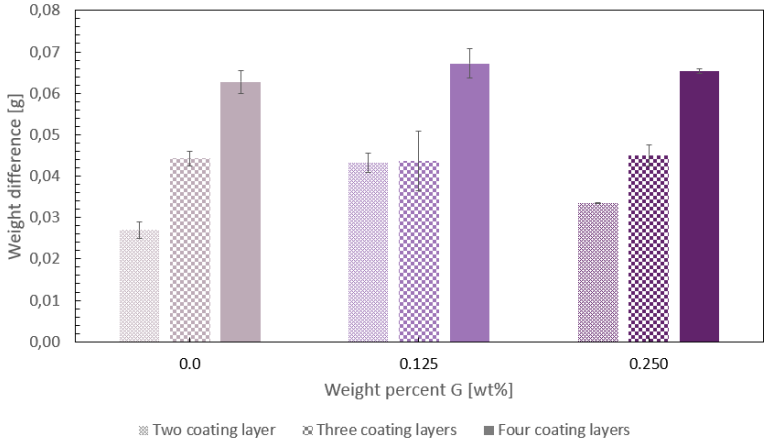

(b) G coatings

Figure 4.6: Weight differences of un-coated substrates and coated samples after the heat treatment step to remove excess solvent.

The weight differences between un-coated and coated substrates after heat treatment are also displayed in Table 4.3. Two samples per type of coating were weighed, and the given uncertainties are therefore the standard deviation of the two measured weight differences per

coating type. The overall trend is increasing weight difference with increasing weight percent of antifouling agent within the same number of coating layers for both the GO and G coatings.

Table 4.3: Weight differences of un-coated substrates and coated samples after the heat treatment step.

Coating/Number of layers	2	3	4
0 wt% GO	0.0201 ± 0.0011	0.0374 ± 0.0030	0.0371 ± 0.0074
0.125 wt% GO	0.0251 ± 0.0007	0.0388 ± 0.0037	0.0599 ± 0.0004
0.250 wt% GO	0.0255 ± 0.0056	0.0387 ± 0.0018	0.0521 ± 0.0033
0 wt% G	0.0270 ± 0.0019	0.0443 ± 0.0018	0.0627 ± 0.0027
0.125 wt% G	0.0432 ± 0.0024	0.0437 ± 0.0071	0.0672 ± 0.0035
0.250 wt% G	0.0335 ± 0.0001	0.0451 ± 0.0025	0.0654 ± 0.0006

The weight difference for the G coatings appear larger compared to the GO coatings. However, this is explained by the larger volume of curing agent added to the G coatings compared to the GO coatings due to differences in molar mass between the DGEBA resin and Epikote resin (see Table 3.8).

Estimation of coating thicknesses

Thickness estimations based on cross-sectional analysis performed in SEM were to be performed, but no results of these measurements are available. The sample holders containing the coated samples did not stabilize the samples resulting in the samples being tilted when the epoxy casting material hardened (see Figure 3.8 in Section 3.6.1). No thickness estimations in SEM were performed due to the tilted sample surfaces.

Due to the unsuccessful thickness estimations in SEM, thickness estimations based on depth range measurements in optical microscope (see Figure 3.9) were performed on the four layer GO and G coatings. The estimated thicknesses are shown in Table 4.4. Five different middle positions of each coating were investigated and the given uncertainties represent the standard deviation of the five measurements per coating type. The four layer GO and G coatings have coating thicknesses of about 130 - 140 µm. The thicknesses seem to be independent of particle content.

Table 4.4: Estimated coating thicknesses of four layered GO and G coatings based on depth range measurements performed in optical microscopy. Epoxy coatings with 0 wt% GO or G are not included as there were no measurable range due to the absent of GO and G.

Coating	Estimated thickness [µm]
0.125 wt% GO	130 ± 11
0.250 wt% GO	142 ± 7
0.125 wt% G	140 ± 10
0.250 wt% G	135 ± 5

The thickness of the epoxy coatings are not estimated as such coatings do not contain particles which must be present to perform thickness estimations by depth range measurements with transmittance light. Thickness estimations of the two and three layer GO and G coatings were not performed due to limited time and as the main focus within surface characterization have been on the four layer coatings.

4.2.2 Surface microstructure

The variations in surface microstructure with respect to number of coating layers, type of spray coater and type of coatings are investigated in this section. Figure 4.7 displays representative SEM-images of an un-coated substrate and coated substrates with respect to these parameter variations. Micro-cracks less than 200 nm are observed on all the prepared coated samples. No significant changes in the microstructure are observed with respect to spray coater used, number of coating layers and type of coatings. All the coatings seem to cover the rough substrate surface shown in a) well resulting in smoother surfaces for the coatings compared to the un-coated substrates.

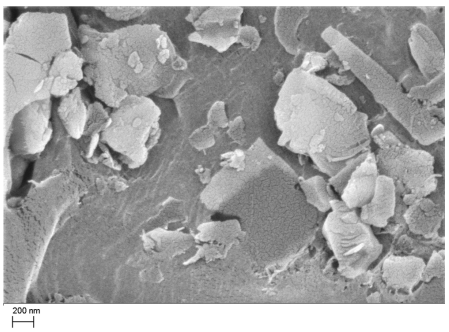

(a) Un-coated substrate

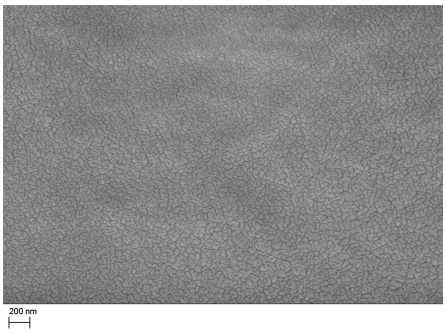

(b) Four layer Epikote coating deposited with a 0.25 mm nozzle

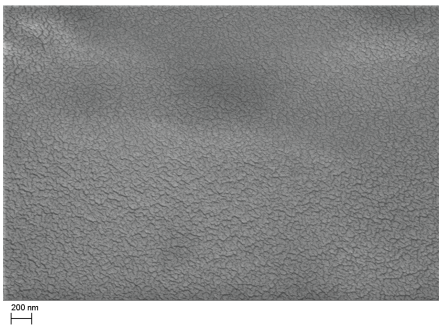

(c) Two layer 0.250 wt% G coating deposited with a 0.25 mm nozzle

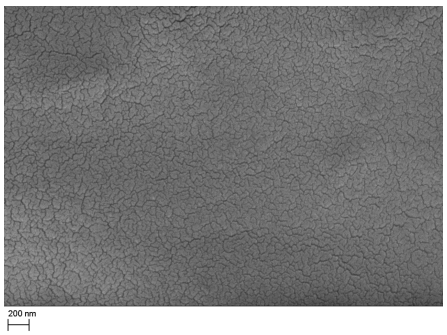

(d) Two layer 0.125 wt% GO coating deposited with a 0.25 mm nozzle

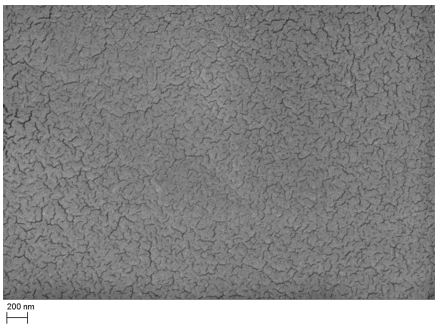

(e) Two layer 0.125 wt% GO coating deposited with a 0.35 mm nozzle

Figure 4.7: SEM-images displaying the surface microstructure of an un-coated substrate and epoxy, GO and G coated samples.

4.2.3 Particle distribution

The surface of GO and G coatings were investigated in an optical microscope to observe the distribution of GO and G within the coating surface as shown in Figure 4.8 for 0.250 wt% four layered GO and G coatings. The GO clusters and G particles seem to be evenly distributed within the coating surface. The GO clusters exhibit a length of about 50 µm while the G particles are mainly of sizes less than 10 µm.

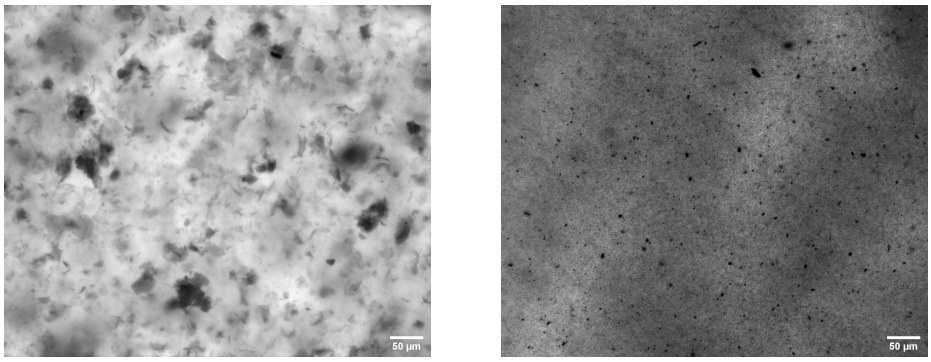

(a) Four layer 0.250 wt% GO coating **(b)** Four layer 0.250 wt% G coating

Figure 4.8: Distribution of a) GO clusters and b) G particles within coating matrix of a four layered 0.25 wt% GO and G coating respectively.

As GO is fluorescent, fluorescence microscopy could be used to investigate the GO distribution within the coating matrix as shown in Figure 4.9 for a four layered 0.250 wt% GO coating. The GO clusters appear red in the fluorescent microscope and seem to be well distributed within the coating matrix.

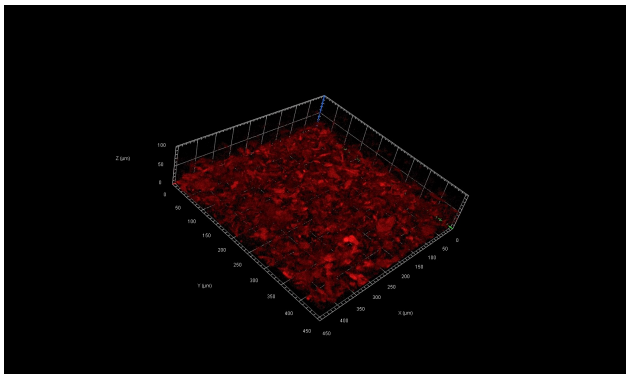

Figure 4.9: Distribution of fluorescent GO within the coating matrix of a four layered 0.250 wt% GO coating.

4.2.4 Wetting properties

The investigated wetting properties with respect to mean contact angles and surface free energies measured on four layer epoxy, GO and G coatings are displayed in this part. The time dependency of the contact angles was measured on the samples four weeks after preparation while the mean contact angles and surface free energies were measured six weeks after

preparation. As will be seen, the difference in time after preparation do not seem to have an affect as similar contact angles were measured.

Mean contact angles

All the prepared coatings exhibit a hydrophilic character based on the estimated water contact angles shown in Figure 4.10 a) while the substrate exhibits a hydrophobic character. Contact angles estimated by 1-Bromonaphthalene are shown in Figure 4.10 b). In general for the coated samples, the contact angles of both water and 1-Bromonaphthalene seem to increase with increasing weight percent of GO or G.

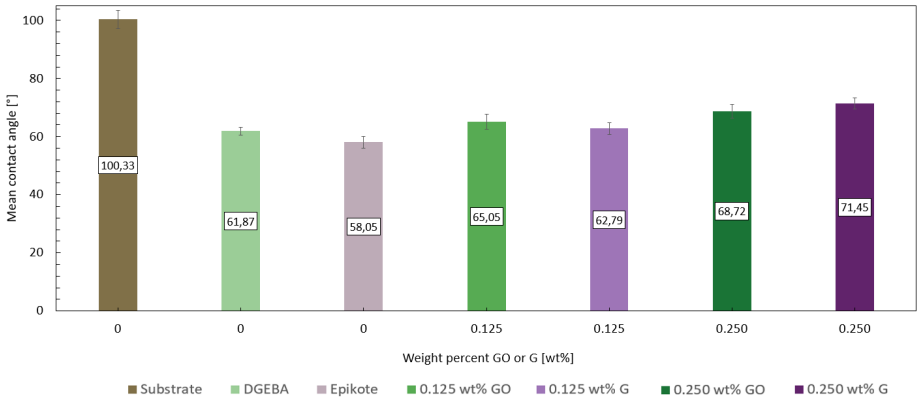

(a) Estimated water contact angles

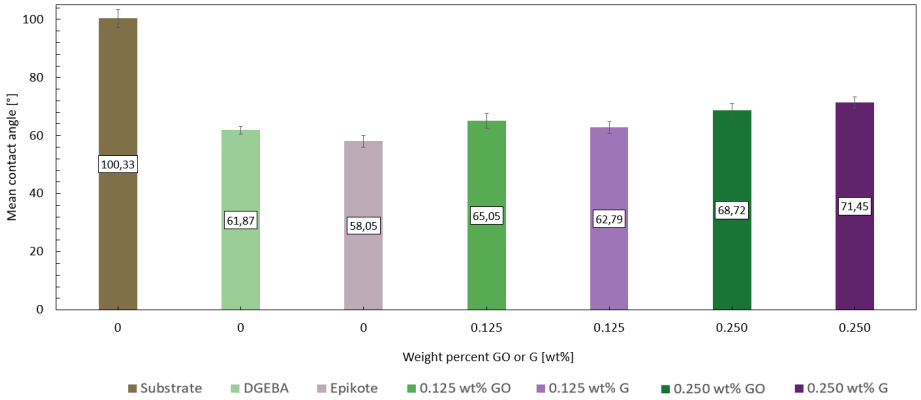

(b) Estimated 1-Bromonaphthalene contact angles

Figure 4.10: Estimated contact angles with a) water and b) 1-Bromonaphthalene on four layer epoxy, GO and G coatings.

The estimated left and right contact angles per sample differed with about 1.0 ° as represented by the water droplet position onto a 0.250 wt% GO coating in Figure 4.11. This trend is observed for all the coatings and the un-coated substrate. The mean contact angles presented in Figure 4.10 are therefore representative.

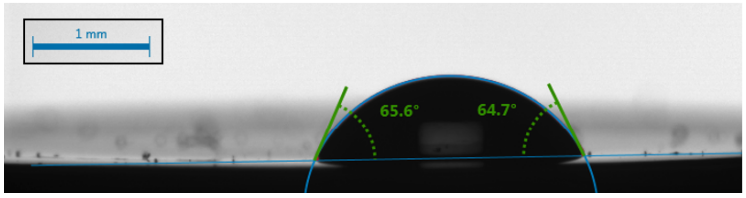

Figure 4.11: Only slight variation with respect to the contact angles measured on the left and right hand side are observed for all the coatings. This illustrative image is from the water droplet measurements performed on a 0.25 wt% GO coating.

The time dependency of water contact angles were investigated and the results are shown in Figure 4.12. All the coatings and the substrate behave in a similar manner with respect to reduction of the water contact angle with time.

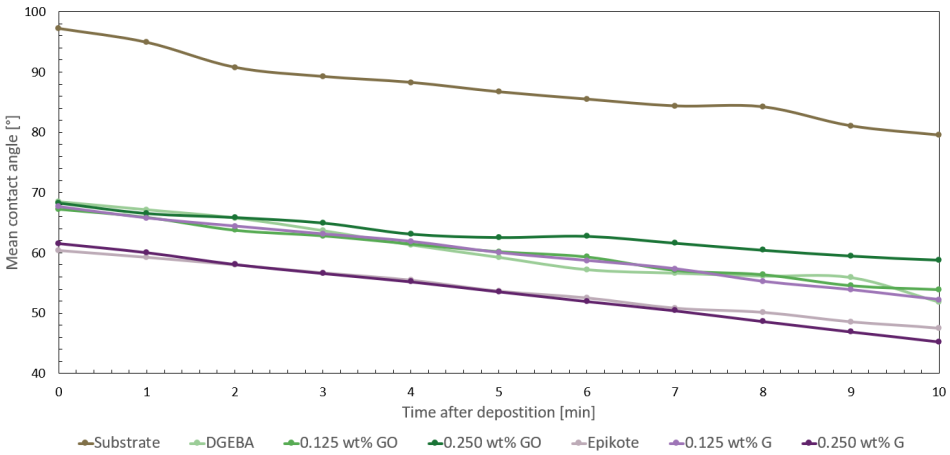

Figure 4.12: Development of water contact angles over time for the prepared four layer epoxy, GO and G coatings.

Surface free energies

The surface free energy of the prepared coatings and a substrate was estimated based on the mean contact angles of water and 1-Bromonaphthalene, and the results are displayed in Figure 4.13. The surface energy consists of a polar part (dotted bars) and a disperse part (continuous bars) which are based on permanently and temporary variations within the electron densities respectively [202, 203]. The surface free energies for the epoxy coatings are slightly higher compared to the GO and G coatings.

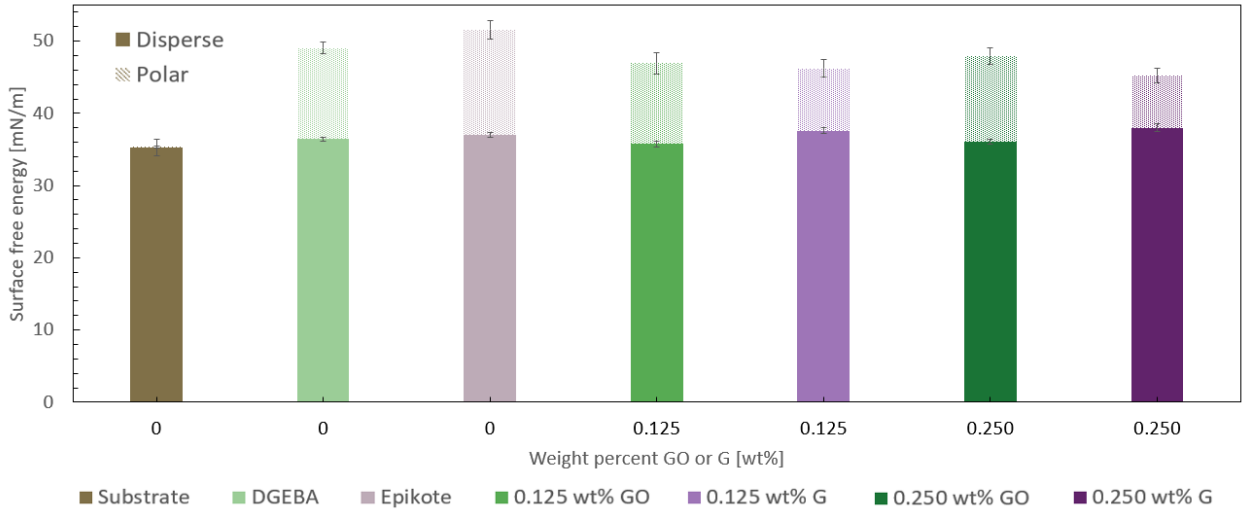

Figure 4.13: Estimated surface free energies for prepared coatings as well as a substrate. Continuous bars represent the disperse parts of the surface free energies while polar parts are indicated by dotted bars.

Relation between contact angles and surface free energies

An overview of contact angles and surface free energies are found in Table 4.5. Coatings exhibiting a low water contact angle result in a higher surface free energy. This trend is also seen for the substrate in which the substrate exhibits the highest contact angles and the lowest surface free energy which is as expected by the literature [50].

Table 4.5: Mean contact angles (CA) for water and 1-Bromonaphthalene as well as the estimated surface free energy for the prepared coatings and the substrate.

Sample	Water CA [°]	1-Bromonaphthalene CA [°]	Surface free energy [mN/m]
Substrate	100 ± 3	38 ± 2	35 ± 1
DGEBA	62 ± 1	20 ± 1	49 ± 1
Epikote	58 ± 2	15 ± 1	52 ± 2
0.125 wt% GO	65 ± 3	24 ± 1	47 ± 2
0.125 wt% G	63 ± 2	18 ± 1	48 ± 2
0.250 wt% GO	69 ± 2	19 ± 1	46 ± 2
0.250 wt% G	71 ± 2	19 ± 2	45 ± 1

4.2.5 Surface roughness

Surface roughnesses of four layer coatings and an un-coated substrate were estimated by using optical microscopy as well as profilometer.

Optical roughness measurements

The roughness measurements performed in the optical microscope appear non-reliable as no automatic planar reference plane was applied in the workpiece coordinate system. As can be seen in Figure 4.14 which displays an obtained surface topography image of a four layer 0.125 wt% G coating, the sample surface appears non-planar as no automatic planar reference plane

was defined.

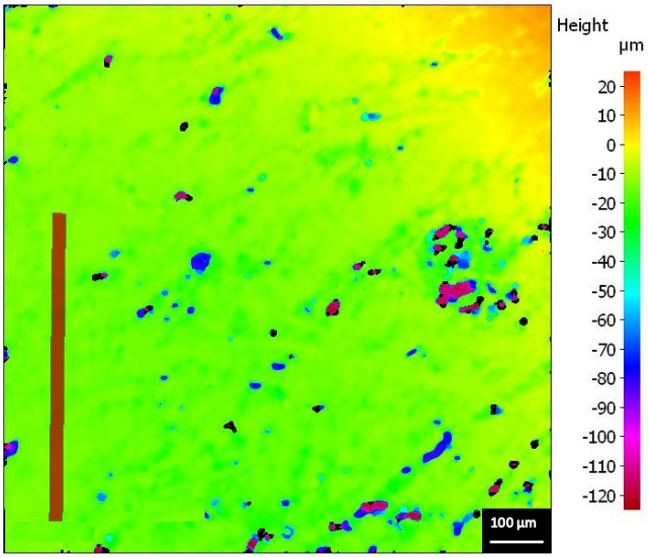

Figure 4.14: Illustration of optical roughness measurements performed on a four layer 0.125 wt% G coating with no automatic planar reference plane defined.

Physical roughness measurements

The surface roughness average (Ra) values for the prepared four layer coatings and an un-coated substrate were estimated at three different middle positions per sample in a profilometer and the results are shown in Table 4.6. Only two positions for the Epikote and 0.125 wt% G coatings were used as the third positions deviated a lot from the others with respect to the estimated Ra values. All the coatings exhibit surfaces with significantly less roughness compared to the un-coated substrate. The G coatings and epoxy coatings exhibit similar surface roughnesses, while the GO coatings have higher Ra values compared to the other coatings.

Table 4.6: Estimated surface roughness average (Ra) values of the un-coated substrate and the prepared four layer coatings.

Sample [-]	Estimated roughness, Ra [nm]
Substrate	627.8 ± 277.4
DGEBA	3.4 ± 1.3
Epikote	3.5 ± 0.2
0.125 wt% GO	16.6 ± 4.8
0.250 wt% GO	24.9 ± 10.5
0.125 wt% G	3.1 ± 0.3
0.250 wt% G	3.9 ± 1.4

Similar trends are seen when investigating the surface profiles shown in Figure 4.15 of the a) un-coated substrate and b) four layer 0.250 wt% GO coating which is representative for the other coatings. The hills and valleys observed in the surface profile of the substrate are significantly reduced after coating deposition with any of the coatings. Surface profiles of the other coatings are found in Figure F.1 in Appendix F.

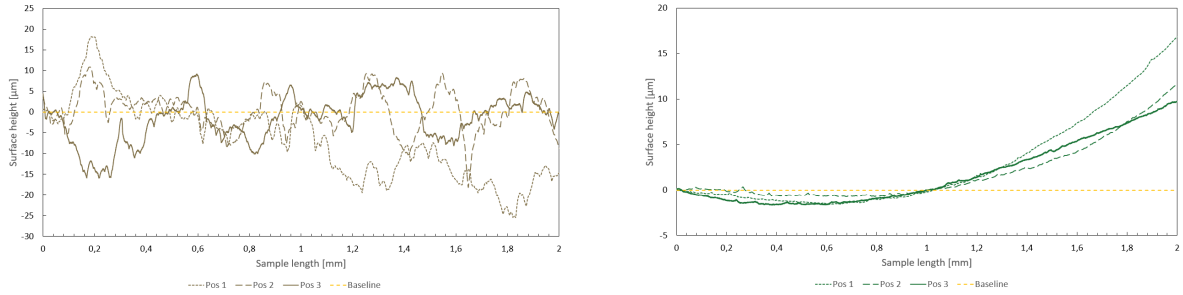

(a) Un-coated substrate

(b) 0.250 wt% GO coating

Figure 4.15: Surface profiles obtained from profilometer measurements. Three positions were measured per sample.

4.3 Characterization of antifouling properties

In the following part the antifouling properties of samples being submerged in the biofilm reactor for two and four weeks will be investigated. In section 4.3.1, the algae tribal culture used in the biofilm reactor are investigated with respect to presence of fouling organisms. Fouling organisms present on the submerged samples are investigated in section 4.3.2. In section 4.3.3, parameters as diatom size, number of diatoms and percentage of diatom covered area which all are related to diatom growth on the submerged samples are investigated. The effect of antifouling agents, number of coating layers, submersion time and type of coating are also evaluated. The thickness of the biofilms growing on the submerged samples are estimated in section 4.3.4. Finally, a short summary of the antifouling findings are reported i section 4.3.5.

4.3.1 Investigation of algae culture

Investigation of the algae culture with algae nutrition prior to transferring to the biofilm rector and the start of the biofilm reactor experiments were performed in an optical microscope, and the investigated algae growth is shown in Figure 4.16. Yellow frames are marked around diatoms to illustrate their characteristic rectangular shape. The diatoms were found growing both single, in pairs and in longer chains. Other algae as well as bacteria were also found to be present in the algae culture and are seen as particles with a non-rectangular shape in Figure 4.16.

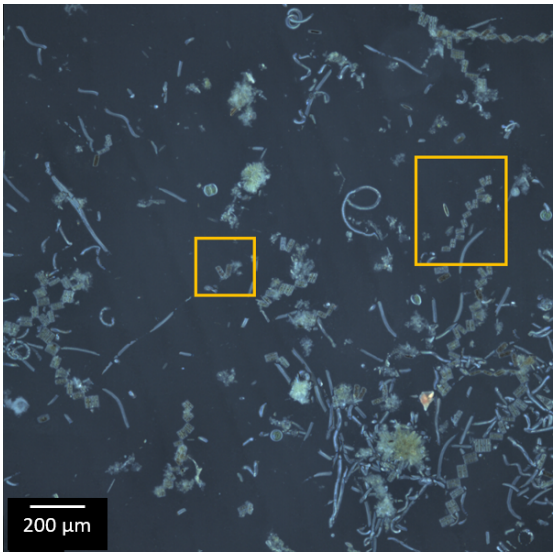

Figure 4.16: Algae growth in the algae culture with algae nutrition prior to the start of the biofilm reactor experiments. Yellow frames highlight some diatoms which exhibit the characteristic rectangular shape.

4.3.2 Investigation of algae growth on coated samples

As illustrated with yellow frames in Figure 4.17 for a representative selection of samples, algae growth was observed on all the submerged samples while using a 10X lens. Un-coated substrates submerged along with GO and G coatings are used as references for algae growth on GO and G coatings respectively. The characteristic rectangular shape of diatom growth are shown in Figure 4.17 a)-d) while bacterial growth or non-diatomic growth are observed in e). The algae growth on the submerged samples is heavily dominated by diatom growth. Salt particles precipitated on the samples after the extraction out of the biofilm reactor and are seen as small, white particles on the samples.

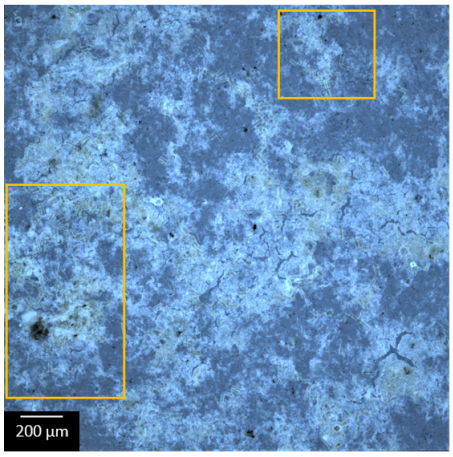

(a) Un-coated substrate reference for GO coatings with submersion time of two weeks

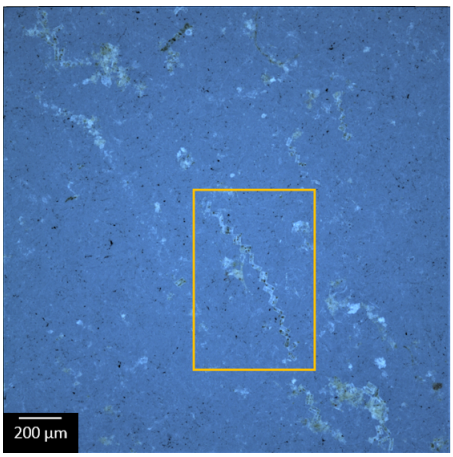

(b) Un-coated substrate reference for G coatings with submersion time of two weeks

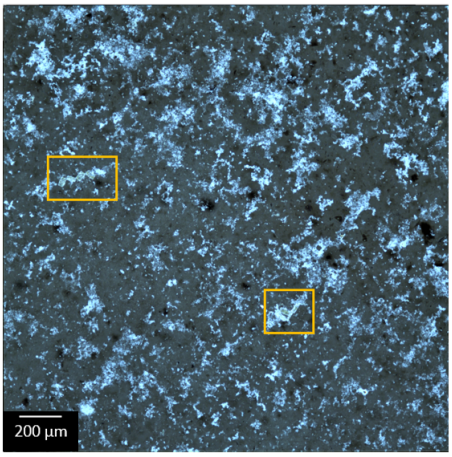

(c) Four layered 0.125 wt% GO coating with submersion time of four weeks

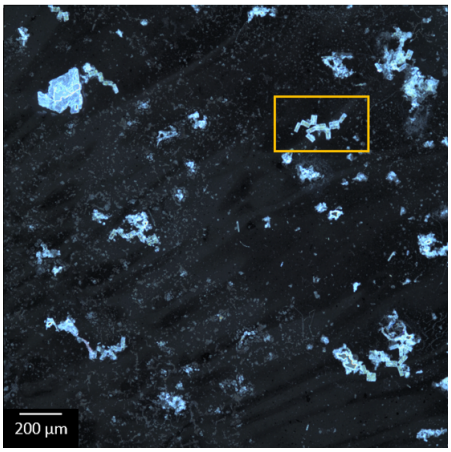

(d) Two layered 0.125 wt% G coating with submersion time of two weeks

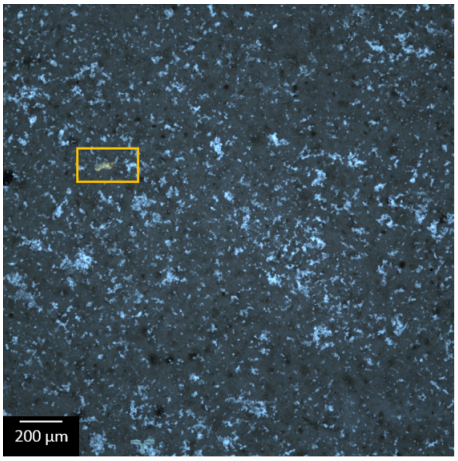

(e) Three layered 0.125 wt% GO coating with submersion time of four weeks

Figure 4.17: Algae growth marked in yellow frames on submerged samples with diatom growth shown in a)-d) while bacterial or non-diatomic growth is shown in e).

Confirmation of algae growth

To investigate the algae growth further, element analysis of the marine growth observed on the samples being submerged for two weeks was performed. Similar findings were found for all samples and therefore the further analysis only includes a representative case. EDS-analysis of the points displayed in Figure 4.18 was performed on the four layer 0.125 wt% GO coating being submerged for two weeks. The corresponding element content of the different objects are shown in Table 4.7. The element contents at each points are reported as the average value of three similar objects measured at three different positions on the coating surface. The uncertainties are given as the standard deviation of the three similar objects. Carbon is subtracted from the element analysis since the samples were sputter coated with carbon prior to the analysis.

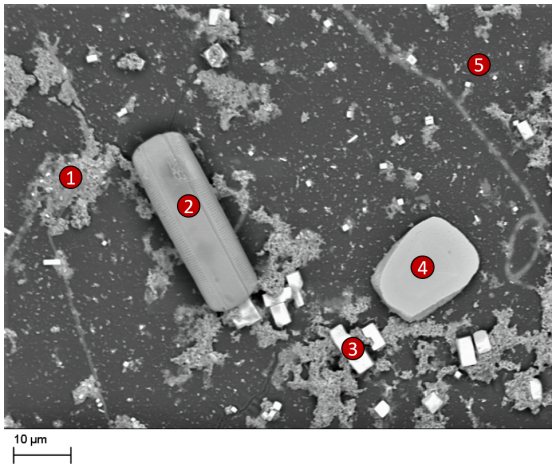

Figure 4.18: EDS point analysis performed in SEM of a four layer 0.125 wt% GO coating which had been submerged in the biofilm reactor for two weeks. The numbered points marks the points measured during the point analysis, and their corresponding element contents are found in Table 4.7.

Due to the colour changes seen in the backscattered SEM-image displayed in Figure 4.18 and the corresponding element content in Table 4.7, it appears clear that the objects do not exhibit the same chemical composition. The first object is most likely biofilm or decaying cell content which is commonly found in the sea and known as marine snow [204]. The significant content of magnesium indicates the presence of chlorophyll pigments within the marine snow as chlorophyll pigment consist of some magnesium [205]. The second object is characterized as a diatom due to the characteristic rectangular shape and the large silicon content reported in the object [206]. The third object is classified as a typical sea salt particle as the dominating elements are sodium and chlorine [207]. Due to the smooth surface and morphology, the fourth object is most likely a sea water bacteria which can contain sulfur and calcium [208]. However, the fourth object could also be a smaller sea organism or parts of limestone shells which are commonly found in the sea. The fifth object represent the coating surface itself and would have consisted of primarily carbon if the carbon element had not been removed.

Table 4.7: Element compositions of the points measured in the point analysis shown in Figure 4.18 on a four layer 0.125 wt% GO coating being submerged for two weeks. Carbon is removed from the element analysis and the element weight percents are estimated from the three positions measured at similar objects. The uncertainties are the standard deviation of the values.

Object	Element	Weight percent [wt%]
1	O	46.3 ± 7.4
1	Cl	13.7 ± 6.3
1	Mg	15.3 ± 5.1
2	O	49.5 ± 2.0
2	Si	41.9 ± 4.7
2	Cl	4.9 ± 3.6
2	Mg	2.8 ± 1.7
3	Cl	55.5 ± 0.3
3	Na	43.6 ± 0.5
3	O	1.0 ± 0.3
4	O	2.3 ± 0.9
4	S	49.4 ± 22.7
4	Ca	10.4 ± 11.3
4	Na	52.4 ± 5.9
4	Cl	43.9 ± 7.6
5	O	97.3 ± 4.7
5	Cl	8.3 ± 0.3

4.3.3 Diatom growth on submerged samples

Diatom growth with respect to preferred growth position, diatom size and morphology are to be investigated in this paragraph. Figure 4.19 illustrates diatoms (marked in yellow frames) found on a four layer 0.125 wt% GO coating and a three layer 0.125 wt% G coating which were submerged for two weeks. The major parts of the diatoms on all surfaces had a length of about 40 µm which is in good agreement with similar experiments performed by Chauton et al. [186]. However, a few diatoms exhibit a length of about 17 µm. The size of the diatoms appear independent with respect to which surface they grew on and submersion time in the biofilm reactor. Diatoms were observed growing single, in pairs and in larger chains, but were mainly observed in larger flocs for the un-coated substrates and flocs or chains for the coatings. As seen in Figure 4.19, the encasement of the diatoms do not seem damaged when growing on coatings with GO or G content. No damages in diatom morphology were observed for diatoms growing on coatings or substrates.

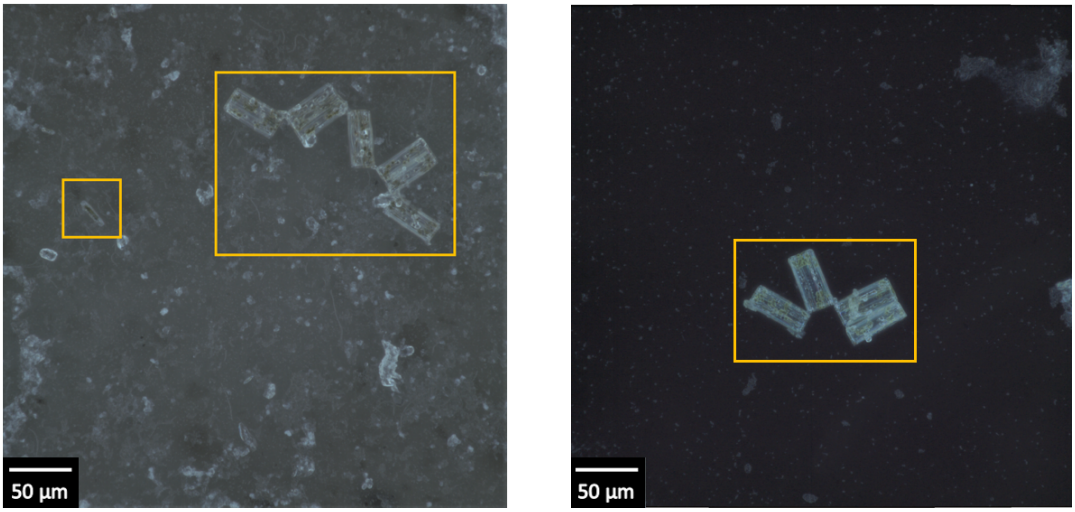

(a) Four layer 0.125 wt% GO coating **(b)** Three layer 0.125 wt% G coating

Figure 4.19: Diatom growth marked in yellow frames observed on a) 0.125 wt% GO coating and b) 0.125 wt% G coating being submerged for two weeks.

In the further part, the average number of diatoms as well as the average percent diatom covered area will be investigated. The values are given as the average of measurements performed in optical microscopy on twelve sample positions with a measured area of 4.17 mm^2 resulting in 40% of the sample area being measured.

Un-coated reference substrates

Un-coated substrates were submerged in the biofilm reactor along with either GO coatings or G coatings and are used as references for the coatings they were submerged with. The average number of diatoms (hereby referred to as number of diatoms) and estimated diatom covered area are shown in Table 4.8.

Table 4.8: Diatom growth observed on the un-coated reference substrates for GO and G coatings in which the references were submerged with the GO and G coatings respectively.

Reference system	Submersion period [weeks]	Number of diatoms [-]	Estimated diatom covered area [%]
GO	2	94	4.0
	4	34	0.9
G	2	72	2.3
	4	151	5.1

The difference in diatom growth between the GO and G references appear as the GO and G coatings were submerged in separate biofilm reactors with algae cultures of different age (see Section 3.4). There is no logical explanation to why there is observed less diatom growth for the GO reference substrate with submersion time of four weeks compared to two weeks. The uncertainty is difficult to estimate as the algae growth relies heavily on the measured surface positions as the algae is not evenly distributed throughout the sample surface.

Coated samples

The number of diatoms and estimated diatom covered area on the coated samples are shown in Table G.1 and G.2 in Appendix G. The diatom covered area is not proportional with number

of diatoms and is therefore not used in the further analysis of diatom growth. The four layer 0 wt% GO coating (DGEBA coating) and 0.125 wt% GO coating which were submerged for four and two weeks respectively are considered as unrealistic representations since they exhibit a significantly higher growth compared to similar coatings. These samples are therefore not included in the further analysis. The same matter appears for the two layer 0 wt% G (Epikote) and four layer 0.250 wt% G coatings which were submerged for four weeks. The number of diatoms will be analysed with respect to effect of weight percent of antifouling agent, number of coating layers, submersion time and coating type in the following part.

Effect of GO and G content

The coatings containing GO and G exhibited significantly less diatom growth in terms of number of diatoms compared to their corresponding reference substrates. In addition, the coatings with no GO and G content did also obtain less growth compared to the reference growth (see Table 4.8). These findings are visually displayed in Figure 4.20.

(a) Two layer GO coatings

(b) Three layer GO coatings

(c) Four layer GO coatings

(d) Two layer G coatings

(e) Three layer G coatings

(f) Four layer G coatings

Figure 4.20: Number of diatoms measured on 0.0 - 0.250 wt% GO coatings with a) two, b) three and c) four coating layers and 0.0 - 0.250 wt% G coatings with d) two, e) three and f) four coatings layers. Diatom growth after submersion for two weeks (dotted bars) and four weeks (continuous bars) are shown. Unrepresentative data points are removed and marked with a cross.

The diatom growth is significantly larger for the G reference substrate compared to the GO reference substrate which is also seen in the figure for the coatings. The GO coatings have in general less growth compared to the G coatings. Within the same number of coating layers for the same coating type, the overall trend is reduction in diatom growth with increasing GO or G content in the coatings. The trend appears more significant for the GO and G coatings being submerged for two weeks compared to four weeks.

Effect of number of coating layers

The effect of number of coating layers for the GO and G coatings are shown in Figure 4.21. As can be seen, there is no clear correlation between number of diatoms and number of coating layers for either the epoxy, GO or G coatings. This is seen as the number of diatoms vary randomly within each weight percent of GO and G. Therefore, the number of coating layers do not seem to affect the diatom growth significantly.

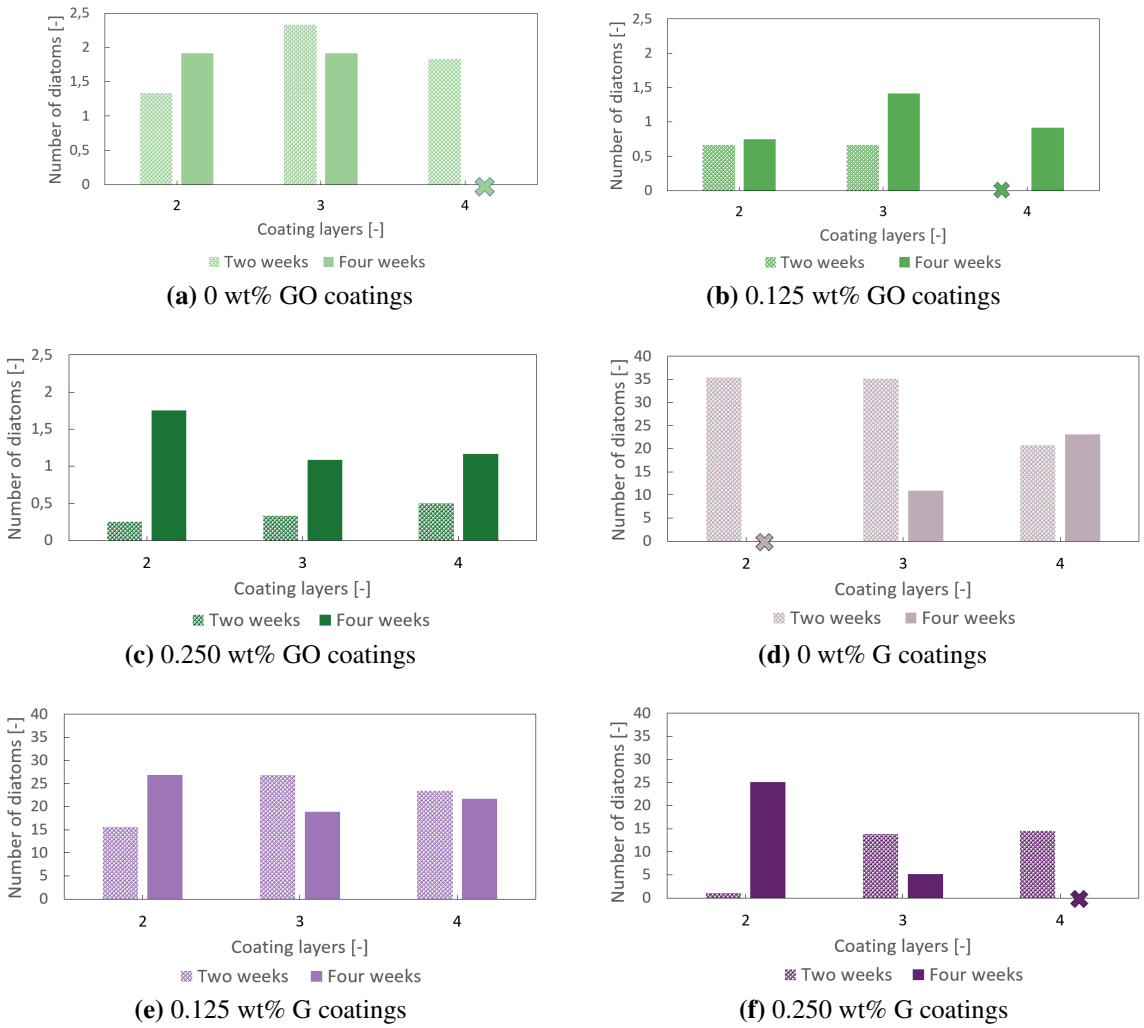

(a) 0 wt% GO coatings

(b) 0.125 wt% GO coatings

(c) 0.250 wt% GO coatings

(d) 0 wt% G coatings

(e) 0.125 wt% G coatings

(f) 0.250 wt% G coatings

Figure 4.21: Number of diatoms after submersion for two and four weeks measured on a) 0 wt%, b) 0.125 wt% and c) 0.250 wt% GO coatings and d) 0 wt%, e) 0.125 wt% and f) 0.250 wt% G coatings. Unrealistic data points are removed and marked with crosses in the Figure.

Effect of submersion time

Coated samples were submerged for two or four weeks and the investigation of the effect of

submersion time with respect to number of diatoms are based on Figure 4.22. More algae growth was observed on the DGEBA and GO coatings being submerged for four weeks compared to two weeks when comparing the number of diatoms on similar coatings with the same number of coating layers. The largest difference in number of diatoms with respect to submersion time are observed for the 0.250 wt% GO coatings. However, this trend is not observed for the Epikote and G coatings. The algae growth of the Epikote and G coatings is inconclusive when comparing samples with the same number of coating layers being submerged for two and four weeks.

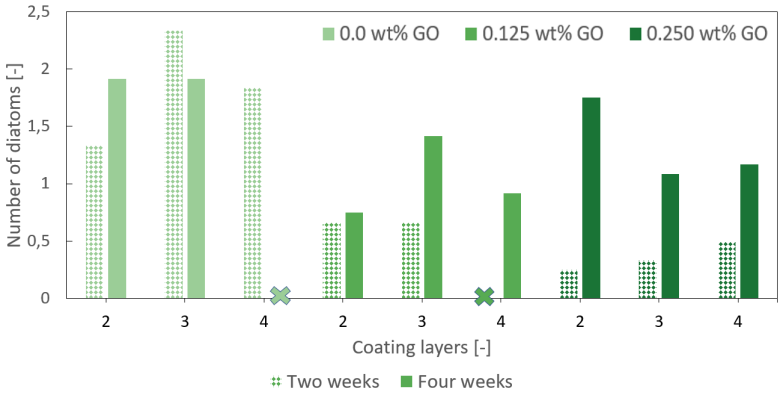

(a) GO coatings

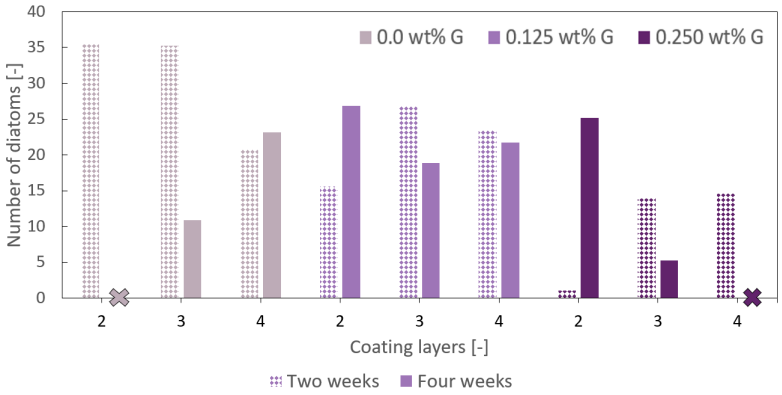

(b) G coatings

Figure 4.22: Number of diatoms measured on a) GO coatings and b) G coatings. Unrealistic data points are removed and marked with crosses in the Figure.

Effect of coating type

The DGEBA and GO coatings appear to be significantly more efficient antifouling coatings compared to the Epikote and G coatings after submersion of two and four weeks. This is seen from Figure 4.23 in which the percent of diatom growth observed on the coated samples compared to their corresponding reference substrates (see Table 4.8) are investigated. It should be mention that the increase in diatom growth observed on the DGEBA and GO coatings being submerged for four weeks are related to the un-natural low diatom growth found on the GO reference substrate. Therefore no further analysis of the percent diatom growth on the GO coatings being submerged for four weeks will be performed. When comparing the percent growth occurring on the Epikote and G coatings submerged for two and four weeks, there is observed significantly less growth after four weeks.

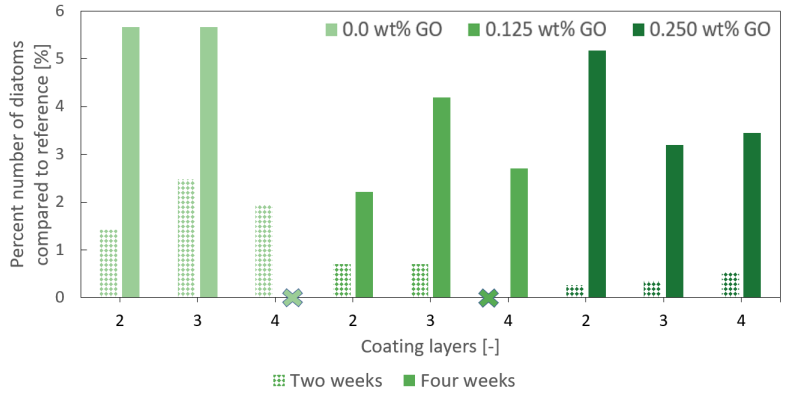

(a) GO coatings submerged for two and four weeks

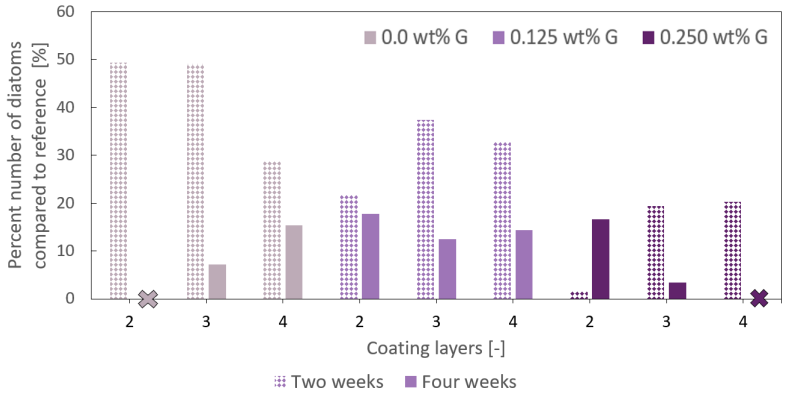

(b) G coatings submerged for two and four weeks

Figure 4.23: Number of diatoms measured on a) GO coatings and b) G coatings as percent of the growth observed on reference substrates. Unrealistic data points are removed and marked with crosses in the Figure.

4.3.4 Estimation of biofilm thickness

Biofilms consist of both diatoms, bacteria and other algae material. The thickness of the biofilms growing on the references and three layer samples being submerged for two weeks were investigated by using fluorescence microscopy and the average biofilm thicknesses of three positions per sample are displayed in Table 4.9. The uncertainties are given as the standard deviation of these three positions. As can be seen, the biofilm thickness of the reference substrates are larger compared to the coated samples. The biofilm on the GO reference exhibits half as thick biofilm as the G reference. The number of diatoms on the GO reference is however larger compared to the G reference submerged for two weeks (see Table 4.8). The biofilm thicknesses on the GO coatings seem to increase with increasing GO content while the opposite matter is seen for the G coatings.

Table 4.9: Estimated biofilm thicknesses based on three middle positions per sample on three layer GO and G coatings with references which all had been submerged for two weeks. The biofilms include all algae growth observed on the samples and were estimated using fluorescence microscopy.

Coating type [-]	Weight percent GO or G [wt%]	Biofilm thickness [um]
GO	Ref	5.3 ± 1.7
	0.0	2.7 ± 0.2
	0.125	2.8 ± 0.3
	0.250	4.1 ± 1.2
G	Ref	10.3 ± 3.1
	0.0	6.3 ± 0.9
	0.125	4.4 ± 3.7
	0.250	3.9 ± 1.1

Figure 4.24 displays pictures of the biofilm found growing on a three layer 0.250 wt% GO coating taken with transmittance light and fluorescence as well as the calculated topography image of the biofilm. An image illustrating the fluorescence properties of GO particles are also included. As can be seen, the algae growth is easily distinguished from the GO particles due to its characteristic shape, having more significant fluorescence and optical illumination. The biofilm thicknesses given in Table 4.9 are therefore assumed to be non-affected by the presence of fluorescence GO particles in the coatings. As can be seen, the biofilm is not evenly distributed throughout the coating surface. Differences in the reported biofilm thickness and the height profile of the topography image appear as the biofilm are growing in stacks and thereby may not lie on the coating surface itself. This issue is taken care of in the calculation (see Appendix C) of the biofilm thicknesses and the estimated values shown in Table 4.9 are therefore realistic.

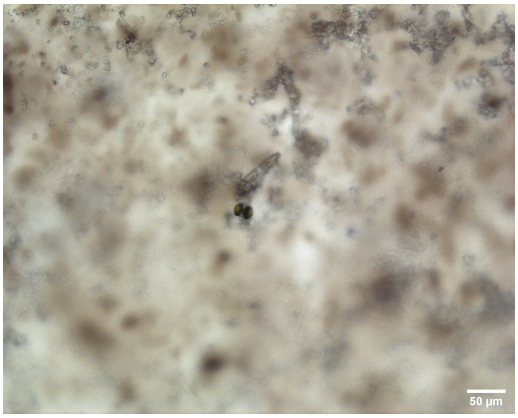

(a) Biofilm shown in transmittance light mode

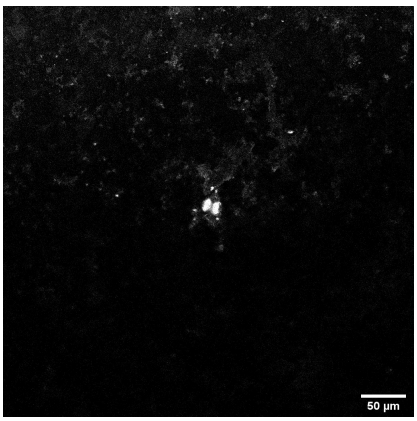

(b) Biofilm shown in fluorescence mode

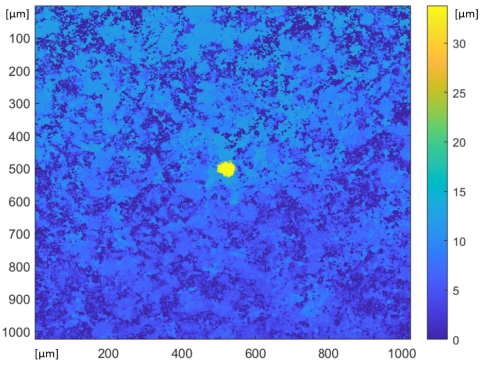

(c) Calculated biofilm topography

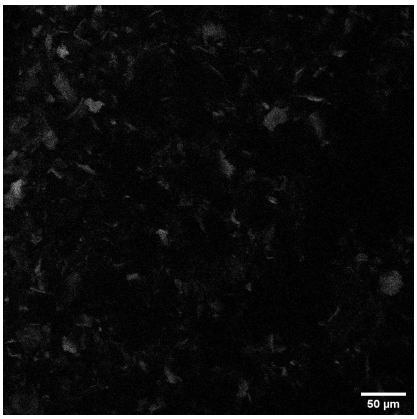

(d) GO particles shown in fluorescence mode

Figure 4.24: Investigation of the biofilm growing on a three layer 0.250 wt% GO coating which had been submerged for two weeks in a) transmittance light, b) fluorescence and c) the calculated biofilm topography. A fluorescence image of GO particles observed in a 0.250 wt% GO coating are shown in d).

The G coatings and epoxy coatings themselves did not appear fluorescent. However, algae growth on these coatings are also visible in fluorescence microscopy and Figure 4.25 illustrates the biofilm in a) transmittance light mode, b) fluorescence mode and c) the calculated biofilm topography image on a three layer 0.250 wt% G coating being submerged for two weeks.

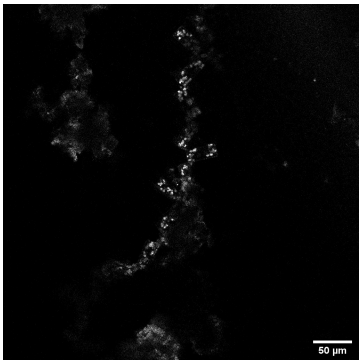

(a) Fluorescence mode

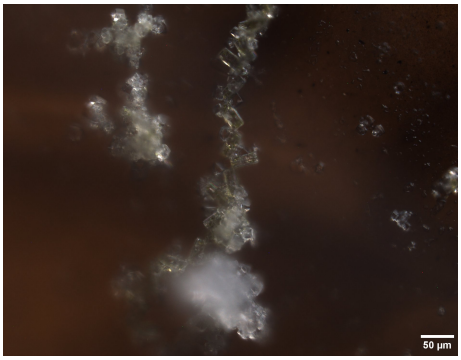

(b) Transmittance light mode

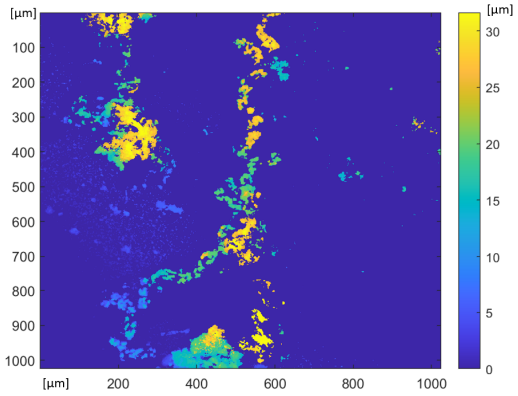

(c) Calculated biofilm topography image

Figure 4.25: Biofilm observed on a three layer 0.250 wt% G coating being submerged for two weeks with a) transmittance light mode, b) fluorescence mode and c) the corresponding calculated topography image of the biofilm.

4.3.5 Summary of antifouling properties of GO and G coatings

A short summary of the antifouling properties is provided in the following part.

- The algae growth observed on the submerged reference substrates and coatings is dominated by diatom growth.
- The majority of the diatoms have a length of about 40 µm.
- No physical damage of the diatom encasments are observed.
- The diatoms are often found growing in flocs which make estimation of algae growth based on percent area covered with algae difficult.
- All coated samples exhibited significantly less number of diatoms compared to their corresponding references.
- More diatom growth were observed for the GO coatings and their references compared to the G coating and their reference.

- Reduction in number of diatoms are observed with increasing GO or G content in the coatings.
- The diatom growth seems to be independent of number of coating layers for all the coatings.
- More diatom growth is observed for the GO coatings being submerged for four weeks compared to two weeks. No correlation is seen between the diatom growth on G coatings and submersion time.
- The GO coatings appear significantly more effective as antifouling coatings compared to the G coatings. For coatings being submerged for two weeks, the diatom growth as percent of the growth observed on the references were below 3 % and 50 % for the 0 - 0.250 wt% GO and G coatings respectively.
- The references being submerged for two weeks exhibit thicker biofilms compared to the coated samples. The GO reference exhibits a biofilm with half the thickness of the G reference.
- Biofilm thickness increases with increasing GO content and decreases with increasing G content.

5 Discussion

The aim of this master's thesis was to prepare epoxy based coatings with GO or G additions and investigate their antifouling properties. In the following part, the combined effects of the surface and antifouling properties are considered. Thereby, the characterization techniques used to investigate the antifouling properties will be evaluated. Next, the antifouling mechanism of the GO and G coatings being submerged in the biofilm reactor will be discussed. The experimental procedure for the biofilm generation and synthesis of the coatings are also discussed. Finally, a comment of the mechanical properties and last evaluation of the result will be made.

5.1 Combined effect of surface properties and antifouling properties

Overall, some surface properties have enhanced the antifouling properties while the presence of others may have induced more biofouling than what would have been expected. The combined effects of surface and antifouling properties will therefore be discussed in this part.

5.1.1 Effect of surface roughness and wettability

When investigating the roughness of the prepared samples, it was seen that all the coatings exhibited significantly less roughness compared to the un-coated substrate (see Table 4.6). The reduced roughness and limited irregularities on the coated samples can make it more difficult for algae or bacteria to attach. As a consequence, significantly less biofouling were observed on all the coated samples compared to the un-coated substrates. The antifouling properties of the epoxy coatings are therefore most likely related to their smooth surfaces rather than any of the mechanisms discussed in the former section. However, as seen further on, the wettability should also be taken into consideration when investigating the effect roughness had on the biofouling [145].

The G and epoxy coatings exhibited similar roughnesses, but the GO coatings had slightly higher roughness which may be related to the stability and viscosity of the GO slurries. The GO slurries exhibited both poorer stability and higher viscosity compared to the epoxy sols and G slurries. This may have influenced the way the GO slurries were spray coated onto the substrates. However, the stability of the GO slurries did not affect the distribution of GO within the cured coatings as GO sheets were found evenly distributed within the coating matrix as shown in Figure 4.8 a). The higher viscosity of the GO slurries compared to the other sols and slurries (see Table 4.2) may better explain the difference in roughness. Consequently, the GO slurries were most likely harder to spray evenly throughout the spray coater. In addition, the GO sheets within the coatings exhibited a size of about 50 µm while the G particles were of size 10 µm or even smaller making the G slurries being easier to spray coat. The higher viscosity of the GO slurries did although not affect the coating thicknesses significantly as both the GO and G coatings exhibit similar thicknesses.

According to the Wenzel equation [155], the roughness influences the wettability of the coatings in which increased roughness enhance the wettability for hydrophilic surfaces. However, no clear correlation is found between the surface roughnesses and the water contact angles for the prepared coatings. Due to the increased roughness observed on the GO coatings, they should exhibit a more hydrophilic surface compared to the G coatings according to Wenzel's

equation. This was the case for the 0.250 wt% GO and G coatings, but not the 0.125 wt% coatings. The reason for this deviation may be related to uncertainties within the measurements methods or limitations regarding the definition of roughness in the Wenzel equation [209]. The rougher surfaces found on the GO surfaces probably appeared due to the large GO particles being distributed in the coatings. The presence of the GO sheets has most likely increased the roughness of the coatings due to their bulky morphology. The increased surface area due to the increased roughness in combination with an even distribution of GO particles resulted in more GO particles being in contact with the fouling organisms. Hence, the GO exhibited better antifouling properties compared to the G coatings.

5.1.2 Effect of coating coverage and thickness

The number of coating layers did not seem to affect the antifouling properties of the coatings significantly as no correlation was found between number of coating layers and number of diatoms (see Figure 4.21). Similar trends were also reported by Wendt et al. [175]. The thicknesses of the four layer GO and G coatings with addition of GO or G were estimated to be 130 - 140 µm. Due to the good correlation between increasing coating masses and number of coating layers shown in Figure 4.6, it seems reasonable that the coating thicknesses of the two layer coatings were about half the thickness of the four layer coatings. Therefore, the two layer coatings exhibited assumingly coating thicknesses of 65-70 µm (half the thickness of the four layer coatings). As seen in the SEM investigation of the coatings shown in Figure 4.7, the rough substrate surface were well covered for all numbers of coating layers. It seems therefore reasonable to conclude with the number of coating layers having minor affect on the antifouling properties as the substrate surfaces were well covered even for a low number of coating layers.

5.1.3 Effect of surface free energies

With respect to surface free energies, the substrate exhibited less surface energy compared to the coated samples. In fact, the difference in surface free energies for the substrate compared to the coated samples arise because the substrate has significantly less polar contribution. This is well explained as the substrate exhibited a significantly more hydrophobic character compared to the coated samples (see Figure 4.10). The functional groups of the substrate were not investigated, but hydrophobic functional groups were assumingly dominating. The hydrophilic character of the coated samples were probably related to the presence of polar functional groups as -COOH groups for the Epikote, DGEBA and G coatings and -OH groups for the GO coatings (see Figure 4.2 and 4.3).

The coated samples had surface free energies in the range 45 - 52 mN/m while the substrate exhibited a surface free energy of 35 mN/m (see Table 4.5). As seen in Figure 2.13, minimum biofouling have been reported on surfaces with a surface free energy of about 25 mN/m [50]. Above this value, the amount of bacterial adhesion increases with increasing surface free energy. However, this trend is not seen for the prepared coatings. All the coated samples exhibited less biofouling compared to the substrates even though their surface free energies were larger as shown in Table 4.5. Therefore, it seems like the surface free energies of the coatings had less impact on the antifouling behavior compared to the presence of GO and G particles in the coatings and the reduced coating surface roughness.

5.1.4 Effect of microcracks within the coatings

Microcracks were observed on all the prepared coatings regardless of number of coating layers, coating type or amount of antifouling agents (see Figure 4.7). The presence of microcracks may have initiated more biofouling than what would have occurred without the cracks. The effect the small microcracks had on the marine growth is uncertain as the cracks were less than 200 nm. The presence of cracks should however be avoided with respect to the barrier properties of the coatings. Water can penetrate the coatings more easily if cracks are present which can result in corrosion of the substrate if the substrate is switched out with metals in further experiments. Therefore, further optimization of the coating with respect to reducing the presence of microcracks should be performed in further work.

The microcracks presumably appeared due to the significant amount of solvent content within the coatings. Acetone and ethanol were used as solvents within the DGEBA based coatings and acetone was used as solvent for the Epikote based coatings. Both acetone and ethanol are very volatile solvents and the cracks have most likely occurred due to too rapid evaporation of the volatile solvents. The presence of microcracks will most likely have a negative effect on the mechanical coating properties and further investigation of the mechanical properties are therefore required.

5.2 Evaluation of the characterization of antifouling properties

The antifouling properties of the submerged samples were investigated with respect to type of fouling organisms, average number of diatoms, average percent of sample area covered with diatom growth and thickness of biofilm layers. Some marine growth may have been detached from the sample surfaces during the extraction from the biofilm reactor. However, uncertainties in relation to possible detachment of marine growth was neglected in the antifouling analysis as the samples were all extracted with the same careful procedure.

5.2.1 Investigation of diatom growth

The dominating fouling organism on all submerged samples was found to be diatoms. However, smaller fragments of accumulated bacteria cell material (called marine snow) was also found growing to a large extent on the surfaces as illustrated in Figure 4.18. It was decided to use number of diatoms rather than accumulation of marine snow as an indication of marine growth on the submerged samples. This was beneficial with respect to limiting the uncertainties within the characterization technique as diatoms were easier to quantify compared to the tiny bacteria cell fragments in the optical microscope.

Diatom growth in terms of number of diatoms and percent diatom covered area were used to compare the antifouling properties of the un-coated substrates and coated samples after submersion in the biofilm reactor. Diatoms were often found clinging together in large flocs making the area of each of them hard to measure. In addition, the size of diatoms were found to vary between 17-40 µm. As a consequence, the estimation based on diatom covered area appeared more uncertain compared to number of diatoms (see Table G.1 and G.2 for values).

The number of diatoms was found by counting the number of diatoms at twelve middle positions per sample (see Figure 3.11) by using an optical microscope and calculating the average value.

The uncertainty could may have been reduced by using a 50X lens instead, however more than twelve positions would then have had to be measured to investigate the major part of the sample surfaces. The best compromise with respect to limiting the uncertainties and measurement time was found to be the former method. It should be mentioned that further analysis may benefit from increasing the number of measurement positions to investigate a greater area of the sample surface. With the diatom quantifying procedure used in this thesis, only 40% of the sample surfaces were investigated when using twelve measurement positions. However, the measured positions should not be chosen too near the sample edges due to coating edge effects.

Salt particles were found precipitated at the sample surfaces after the extraction out of the biofilm reactor. Salt particle precipitation did however not affect the quantification of number of diatoms significantly. The diatoms laying beneath salt particles were counted by adjusting the z-position of the optical microscope until the algae, rather than the salt particles, appeared in focus. Nevertheless, this was a time consuming procedure which would benefit from removal of the salt particles. The extracted samples could have been washed gently with freshwater to remove the salt particles, although that could result in detachment of marine growth or deteriorating the characteristic diatom structure [192]. Therefore, the best compromise was to let the salt precipitate at the sample surfaces.

5.2.2 Investigation of biofilm thicknesses

The biofilm thicknesses were estimated by using fluorescence microscopy and converting the obtain images to binary images which were analyzed in MATLAB. The diatoms and chlorophyll present within the biofilms appeared fluorescent. In addition, GO sheets were found fluorescent (see Figure 4.24) while G sheets were not (see Figure 4.25) which is in good agreement with the literature [70]. The GO sheets in the coatings exhibited a characteristic sheet morphology which was easily distinguished from the fluorescent signals of the marine growth. This fact becomes clear when comparing the thickness of the biofilms growing on GO coatings with the GO coating thicknesses since there is a significantly thickness difference. In addition, GO and G coatings exhibited relatively similar biofilm thicknesses. Therefore, the conducted method to investigate biofilm thicknesses seems reliable.

The biofilm thicknesses of the GO coatings were lesser compared to the G coatings as shown in Table 4.9. This correlates well with the fact that more marine growth in general was observed on the samples being submerged along with the G coatings. As more marine growth occurred, the biofilm thickness was likely to increase. However, different trends were observed in the biofilm thicknesses for GO and G coatings as the GO or G content increased. The biofilm thicknesses of the GO coatings seemed to increase with increasing GO content while the opposite matter was seen for the G coatings. For comparison, Lee et al. [81] reported reduction in biofilm thickness with increasing GO content within the coatings. Number of diatoms decreased with increasing GO or G content for the three layer coatings being submerged for two weeks (see Figure 4.20 b) and e)). The biofilm thicknesses measurements given in Table 4.9 are based on those samples. However, the trend observed for the biofilm thicknesses did not correspond with how the number of diatoms changed with increasing GO or G content in the coatings. It seems reasonable to assume that the biofilm thicknesses should reduce as the number of diatoms decreases. As a result, the unexpected increase in biofilm thickness for the GO coatings with increasing GO content is most likely linked to the different age or composition of the algae cultures used in the two biofilm reactor experiments.

5.3 Antifouling mechanisms

The dominating antifouling mechanism for both the GO and G coatings was most likely oxidative stress induced by reactive oxygen species. There were observed no physical damage on the diatoms growing on the GO or G coated samples (see Figure 4.19) which would have been expected if the antifouling properties could have been explained by cell disruption alone [87]. The antifouling mechanism lipid extraction occurs in combination with the cell disruption mechanism and was therefore not expected to occur at a significant degree either. Diatoms were found growing unevenly throughout the surface which may be related to the trapping mechanism performed by the nanosheets of GO or G. However, diatoms have been reported to settle on their preferred areas [38] which may explain the unevenly distribution of diatoms. Diatoms were found growing unevenly on the coatings with and without GO or G additions as well as the substrate. Therefore, the contribution from the trapping mechanism of the GO and G sheets seemed limited. Oxidative stress was therefore assumingly the main antifouling mechanism which is in good agreement with similar experiments [78].

It should be noted that the epoxy coatings with no GO or G additions did also exhibit better antifouling properties compared to the un-coated substrate. However, their antifouling properties are most likely linked to the reduced surface roughness compared to the un-coated substrates rather than the antifouling mechanisms discussed above. In addition, diatoms have been reported to attach more easily to hydrophobic surfaces compared to hydrophilic surfaces [167], which may also explain why there was more biofouling found on the substrates.

5.4 Assessment of the antifouling experiments

Overall the set-up of the biofilm reactor experiments using an algae tribal culture, water pumps and algae nutrition served useful with regards to the investigation of the antifouling properties of submerged samples. The submersion times of two and four weeks were long enough time periods to grow a sufficient level of biomaterial on the submerged samples. Undoubtedly, the methods used to investigate the antifouling properties of the submerged samples appeared more accurate compared to the methods used in earlier work performed by the author [22].

5.4.1 Effect of algae tribal culture

Using the algae tribal culture distributed by SINTEF Ocean in combination with the silica algae nutrition medium resulted in marine growth on all the samples. The algae tribal culture was a heterogeneous system which represented a realistic sea environment within the biofilm reactor. Using the silica algae nutrition accelerated the growth of diatoms especially [31].

To gain even more marine growth within the biofilm reactors, more efficient light sources may be applied. In addition, removal of the plastic balls present on the water bath surface (see Figure 3.7) could further enhance the light access. However, removal of the plastic balls could have resulted in water temperature changes which could have reduced the growth of fouling organisms [2, 23, 24].

Regarding reproducibility, the algae culture should have been further analysed with respect to composition over time. The algae culture was a realistic heterogeneous system consisting of primary colonizers and the composition is likely to have changed over time. Making use of

flow cytometry or other algae characterization methods [183] would have been beneficial with respect to investigating the dominating fouling species and the composition of the algae culture over time. Analysis of the seawater solution within the biofilm reactors would also have been beneficial with respect to controlling the silica content. As diatom growth is dependent on silica content, a reduction in the silica content in the seawater solution is likely to have affected the diatom growth negatively. The preferred settlement surface varies with fouling specie [48] which may have affected the results as GO coatings were submerged with a younger algae culture compared to the G coatings. The composition of the algae culture is likely to have changed over time. Therefore, it would probably have been easier to investigate the antifouling effect of the coatings based on one type of algae rather than the heterogeneous population used in this study. Using a tribal culture with mainly one type of bacteria or algae may also be an advantage with respect to characterization as it can be based on only one fouling organism. It may also be beneficial to carry out antifouling experiments with algae tribal cultures of the same age and thereby with the same composition to easier compare the results.

5.4.2 Effect of releasing antifouling agents

Un-coated samples were submerged along with the coated samples to serve as references for marine growth. However, GO is significantly more soluble in water compared to G [72, 75] which may explain the reduced overall growth on the samples being submerged along with the GO coatings compared to G coatings. The release of GO into the seawater solution may have had a negative impact on the biosystem as the GO sheets exhibit antifouling properties. Release of GO into the algae solution in the biofilm reactor may also explain why it was observed reduced growth on the reference sample being submerged for four weeks for the GO coatings compared to the one being submerged for two weeks (see Table 4.8). In contrast, more growth was observed on the GO coated samples with a submersion time of four weeks compared to two weeks as seen in Figure 4.22. The reduced growth observed on the GO reference being submerged for four weeks are therefore most likely attributed to the reference substrate exhibiting a deviating surface rather than release of GO.

With respect to further work, un-coated substrates should be submerged along with epoxy coatings with no GO or G addition to avoid possible reduction in growth due to biocidal emissions. In addition, references should be submerged along with the coatings as performed in this study to investigate to what extent possible release of GO or G may have had on the overall growth within the biosystem.

5.4.3 Effect of seawater pumps

The antifouling properties of the coatings should be tested in realistic marine environments to investigate their applicability for future use in the marine industry. Using water pumps in the biofilm reactor resulted in a dynamic water flow within the biofilm reactor. It was desirable using a sea water pump with sufficient enough pump speed to secure some rotation of oxygen and nutrition medium. Thereby, the growth medium were distributed evenly within the biofilm reactor. A too large flow rate was undesirable as it may have reduced the marine growth as reported in the literature [2, 23]. However, the experiment suffered from some obstacles regarding the sea water pump stability which could have affected the results of marine growth. Within the first two weeks of both the biofilm reactor experiments, the seawater pumps broke

down resulting in abrupt changes in the environment for a few days before a new pump with the same pump speed was connected. This, in combination with the algae tribal cultures in the two experiments, may explain the difference in amount of marine growth observed within the experiment with GO coatings submerged and with G coatings submerged.

It should be mentioned that the algae tribal culture and set-up of biofilm reactor experiments used in this master's thesis proved useful to investigate the antifouling properties even though there were some limitations which have been discussed above.

5.5 Sol-gel procedure

Overall, the sol-gel method used in this master's thesis was a successful method with regards to achieving sols and slurries suitable for spray coating deposition. Some of the features and aspects of the preparation parameters will be discussed in the following section.

5.5.1 Sol and slurry preparations

Time dependency of the sol and slurry compositions

The epoxy sol compositions did not seem to be changing significantly over time. However, more significant changes with respect to time were found for the slurry compositions as shown in Figure 4.3. This indicates that the polycondensation reactions with GO or G particles were time dependent. The sols and slurries were spray coated within a week after they were prepared, but the composition were stable three weeks after the preparation. Therefore, the degree of each functional group present within the different coatings may have slight variations. It should be mentioned that no curing agent were added to any of the sols or slurries prior to the analysis of the functional groups. Addition of the curing agent resulted in more -OH groups being attached to the polymeric network building up the coating matrix according to the chemical reactions shown in Figure 2.7. Addition of curing agent will accelerate the polymerization. Therefore, there might not have been too large differences in the prepared coatings with respect to functional groups after all.

Slurry stabilities over time

The GO slurries were found to be partly stable over time whereas the epoxy sols and G slurries appeared stable for more than three weeks as shown in Figure 4.1. The GO slurry stabilities could have been improved by increasing the sonication time. However, that may have had a negative effect on the antifouling properties of GO. With increasing sonication time the GO sheets would have became more separated and smaller, but might as well be damaged. Damaged GO sheets in terms of less sharp sheets could have resulted in a worse cutting mechanisms. The optimal sonication time for GO sheets have been reported as two minutes by Ye et al. [210] regarding optimized stability, chemical bonds and mechanical properties. In addition, larger lateral size of GO sheets have been reported to be beneficial with respect to the antifouling properties [82]. This trend may explain why the prepared GO coatings exhibited better antifouling properties compared to G coatings since the GO particles were significantly larger.

The stability of the GO slurries could have been enhanced by adjusting the GO concentration rather than increasing the sonication time. As can be seen in Figure 4.1 b), the stability improved

with increasing GO content. Similar trends have been reported by others as well [81]. As the epoxy resin DGEBA appeared unstable in ethanol and stable in acetone while GO was unstable in acetone, the slurry stability with respect to ethanol is enhanced by increasing the GO content. The presence of carboxyl, hydroxyl and epoxy groups within the GO sheets are beneficial with respect to stability as these groups can form bonds to the organic polymer matrix through condensation reactions [74, 75]. G did not appear stable in the DGEBA resin, but appeared stable within the Epikote resin [191]. There is limited information on the procedure of the preparation of G-Epikote dispersion as this was performed by CealTech AS. However, both the G and GO slurries were most likely stabilized by polymeric stabilization mechanisms as depletion or steric hindrance due to the large polymer content within the slurries. The stability of GO in the Epikote resin was not investigated, but could be useful with regards to further work to maybe prepare more stable GO slurries which can further enhance the coating properties. Preparing GO and G coatings with the same polymer matrix would be beneficial when comparing their antifouling properties.

Time dependency of slurry viscosities

The rheology of the slurries were measured ten days after the preparation. The time dependency of the slurries with respect to rheological properties were not investigated. However, no viscosity changes were observed by eye when depositing the slurries within the first week after preparation. Therefore, it is likely that the viscosities of the slurries were kept relatively constant during the spray coating deposition. It should be mention that the G slurries were classified as shear-thinning fluids. For that reason, their viscosities may have changed more during the coating deposition compared to the other slurry and sols which can have affected the cured properties.

5.5.2 Heat treatment procedure

As explained in the former section, the coatings were all found having hydrophilic surfaces. However, a more hydrophilic character of the cured coatings could maybe have been achieved by increasing the temperature in the heat treatment step. It was decided to keep the temperature at 60 °C during the heat treatment as polyethylene substrates have a maximal operation temperature of about 65 °C. If instead using steel substrates, the heat treatment could have been performed at higher temperatures. As a result, the removal of hydrophobic functional groups could have increased as reported by Ye et al. [211]. Reducing the hydrophobicity of the coatings would possibly reduce the surface free energies of the coatings. As a consequence, the surface free energies may come closer to about 25 mN/m which have been reported as the optimal value with respect to minimize biofouling [50]. However, corrosion issues arise if using steel substrates as steel easily corrodes when being submerged in seawater [96].

5.5.3 Spray coating deposition

Spray coating was used as the deposition technique and all the sols and slurries exhibited a low enough viscosity to be spray coated. However, difficulties regarding proper cleaning of the spray coater occurred. During the laboratory work, a new spray coater with another nozzle size had to be used as the former type were no longer for sale. Leftovers of polymeric substances were probably the reason for the damaged spray coater. Acetone was used to wash the spray coater in between depositions of different sols or slurries as well as after use. The spray coaters

were also sonicated in acetone for some minutes, but unfortunately plastic rings within the spray coater then broke. For future use, a proper cleaning material should be used to avoid clogging the spray coater.

Another alternative would be to use another coating deposition technique. Dip-coating may be a beneficial method as less dilution of the slurries would be needed. Hence, the solvent content within the coatings would reduce which is an advantage with respect to achieving less microcracks in the cured coatings. In addition, the volatile organic compounds content within the coatings would be reduced with is beneficial with respect to environmental emissions. However, dip coating may not be the optimal deposition method for large marine constructions [96]. Therefore, an optimizing of the coating system with respect to amount of resin compared to the antifouling agents and solvents is necessary for further work.

5.6 Comments on the mechanical properties

No hardness test or other investigations of the mechanical properties of the coatings have been performed. However, the prepared coatings were found to adhere well to the substrates even after being submerged in the biofilm reactor. As marine coatings are susceptible to scratches when being exposed to sand particles, during docking or when being in direct contact with other constructions, the scratch resistance is of great interest. Unfortunately no scratch tests were performed on the prepared coatings as the scratch tester was out of use. However, this is a property that should be investigated for the further work. The mechanical hardness of the coatings are another parameter of great importance for marine industries and it should therefore be investigated to evaluate if the prepared coatings are suitable for marine environments.

5.7 Final evaluation of the results

All the prepared coatings exhibited significantly less marine growth compared to the reference substrates. This is most likely related to the decreased surface roughness obtained after coating deposition in addition to the more hydrophilic character of the coated samples. Furthermore, the GO coatings were reported to exhibit the best antifouling properties among all the prepared coatings and their antifouling behavior increased with increasing GO content.

By depositing the substrates with the 0.250 wt% GO coating, the diatom growth reduced with 99% compared to the reference substrate. The great difference in diatom growth were related to the more hydrophilic character, evenly distributed GO fragments and lower surface roughness of the GO coatings compared to the substrate surface. The better antifouling properties of GO coatings compared to G coatings are most likely due to the larger particle size of GO which results in a greater surface contact area between GO clusters and the marine species.

Overall, both GO and G appeared as promising antifouling agents. Further research regarding their antifouling behavior against other fouling species than those used in this study are of great interest. Investigations of the particle size of GO and G with respect to antifouling properties should be performed. A sheet size of GO particles of about 50 µm seemed to prevent marine growth well. It may seem like the G particles could gain better antifouling properties if the particle size of G was increased. Lowering the sonication time in the preparation of the slurries could be a way to obtain a more applicable particle size. An alternative to changing the lateral size of GO or G, is to prepare hybrid nanocomposites by utilizing an epoxy-silicone elastomer

backbone. The combined effect of the low viscous silicone elastomer compared to the epoxy resin and higher dispersibility of GO and G in such coatings [119, 122], make them promising alternatives. However, the mechanical strengths of such coatings must be performed as well to evaluate if they are comparable with other marine coatings. In addition, functionalization of GO and G can be performed to make them dispersible in other coating systems or less volatile solvents.

With respect to deposition time and antifouling properties, the lowest number of coating numbers are preferable as the antifouling properties of the prepared coatings appeared independent of number of coating layers. Therefore, the two layer 0.250 wt% GO coating may serve as the optimal choice with respect to antifouling properties among the prepared coatings in this master's thesis. However, the mechanical properties must be investigated before making a final conclusion to evaluate if the prepared coatings are suitable for marine environments.

6 Conclusion

In this work, epoxy based coatings with GO and G additions have been successfully deposited by using the spray coating deposition technique. The epoxy sols and G slurries appeared stable over time. The GO slurries were found to be partly stable, although the stability increased with increasing GO content. Polymeric stabilization seemed to be the dominating stabilization mechanism due to the significant polymer content within the slurries.

Antifouling properties of the prepared coatings were investigated after submerging coated samples and un-coated reference substrates in a biofilm reactor with an algae culture and algae nutrition. A realistic algae environment was obtained by using an algae tribal culture in which the major fouling organism was characterized as diatoms. All the coated samples exhibited significantly less biofouling compared to un-coated substrates. This was most likely due to the reduced surface roughness on the coatings and diatoms favoring the hydrophobic substrate surfaces rather than the hydrophilic coating surfaces. The difference in wettability is most likely related to the presence of more polar groups within the coatings.

The GO and G coatings exhibited better antifouling properties compared to the epoxy coatings most likely because of an additional antifouling mechanism. Oxidative stress induced by reactive oxygen species was assumingly the dominating additional antifouling mechanism. The antifouling behavior of the coated samples increased with GO and G content within the coatings and was found to be independent of number of deposited coating layers. After submersion for two weeks, the diatom growth occurring on GO coatings and G coatings compared to their un-coated reference substrates were less than 1% and 40%. The significantly greater antifouling properties of GO is most likely related to the larger lateral sheet size of GO within the coatings. Due to the larger GO particles, the surface roughness of GO coatings were slightly increased which resulted in greater surface contact between GO and the marine growth. The antifouling properties of the G coatings may be enhanced by increasing the lateral sheet size or utilizing an epoxy-silicone elastomer coating matrix.

The algae growth occurring on submerged samples was quantified with respect to average number of diatoms and percent diatom covered area. Estimation of marine growth based on number of diatoms was found to be the best quantification method as the area of each diatom was hard to estimate. In addition, the biofilm thicknesses were successfully estimated using fluorescence microscopy in combination with the software MATLAB. However, the quantification methods could benefit from investigating a larger percent of the sample area and using a bacteria or algae culture of known composition in the biofilm generation experiments.

With respect to surface properties, small microcracks were observed on all the coated samples and are most likely attributed to the use of volatile solvents in the sols and slurries. Therefore, optimization of the coatings with respect to obtaining crack-free surfaces should be performed. However, the coatings remained well-adhered to the substrates even during the biofilm generation experiments.

Among all the prepared coatings, the 0.250 wt% GO coatings exhibited the best antifouling properties in addition to great surface properties. Two coating layers seems to be optimal with respect to antifouling properties and environmental emissions, but further investigation of their surface and mechanical properties should be performed to evaluate their marine applicability. In addition, the promising antifouling properties of GO and G coatings should be investigated further to optimize their antibacterial behavior.

7 Further work

The prepared coatings exhibited promising antifouling properties after being submerged in the biofilm reactor to generate biofilms. However, further biofilm assessments should be performed to confirm the findings of this experimental work. In addition, biofilm generation experiments should be conducted for un-coated and epoxy coated samples without the presence of GO or G containing coatings. Thereby, the antifouling properties can be investigated without any effects of possible GO or G emissions in the seawater within the biofilm reactor.

The quantification method based on number of diatoms can be improved by measuring more than 40% of the sample surface as the diatoms was found growing unevenly on the sample surfaces. In addition, the biofilm thickness estimations based on fluorescence microscopy and utilization of MATLAB can be more accurate by estimating the biofilm thickness at a larger number of sample positions.

With respect to characterization of antifouling properties, it will be beneficial to use a bacteria or algae culture of primary colonizers with known composition. The diatom *Amphora* has been reported to settle easily on most surfaces and may therefore serve as a suitable option for the algae tribal culture. In further work, an algae or bacteria culture of known composition could be favorable with respect to the quantification methods regarding number of diatoms and biofilm thickness developed in this thesis. The composition should be measured before and after the biofilm generation experiments by using for instance flow cytometry. The fluorescence signal of the algae growth could benefit from inducing staining markers in the algae culture within the biofilm reactor. To optimize the biofilm assessment basis, the prepared samples should be investigated in parallel experiments with bacteria or algae cultures of the same age or within the same growth cycle.

Even though the prepared coatings exhibited promising antifouling properties, the mechanical properties of the coatings must be characterized to evaluate the applicability in marine environments. Scratch resistance, coating hardness and elastic modulus are properties which should be evaluated in the further work as these properties are of great interest for marine coatings. In addition, the water uptake of the prepared coatings should be considered by measuring the weight difference of submerged samples. It would also be beneficial to investigate the properties of the prepared coating when being deposited onto steel substrates which are more commonly used in marine industries compared to the polyethylene substrates.

The coating system should be optimized with respect to the combined effects of mechanical, surface and antifouling properties as well as consumption of sols and slurries due to environmental emissions. Utilizing epoxy-silicone elastomer coatings may enhance the antifouling properties of G in addition to lowering the required solvent content. Increasing the GO content seems promising with respect to slurry stability and antifouling properties. The solvent content could be reduced to avoid less microcracks as long as it does not affect the sprayability of the coatings significantly. Another approach could be to use a coating deposition technique as dip coating which is suitable for higher viscous coating slurries. Finally, the promising antifouling properties of GO and G could probably be enhanced by optimizing the lateral sheet sizes within the coatings.

Bibliography

[1] Simone Dürr and Jeremy C Thomason. *Biofouling*. John Wiley & Sons, 2009. ISBN 9781405169264.

[2] Diego Meseguer Yebra, Søren Kiil, and Kim Dam-Johansen. Antifouling technology—past, present and future steps towards efficient and environmentally friendly antifouling coatings. *Progress in Organic Coatings*, 50(2):75 – 104, 2004. ISSN 0300-9440. doi: https://doi.org/10.1016/j.porgcoat.2003.06.001. URL http://www.sciencedirect.com/science/article/pii/S0300944003001644.

[3] FoundOcean. Foundocean Expands its Subsea and Offshore Services with Introduction of Marine Growth Prevention and Control Products (UK). https://www.offshorewind.biz/. Accessed: 2021-05-04.

[4] Cathelco marine growth prevention systems technology description. Accessed: 2021-05-04.

[5] Nylon net, Shinynet In Aquaculture Cage. https://shinynets.com/about-shinynet/. Accessed: 2021-05-04.

[6] Asger Lindholdt, Kim Dam-Johansen, SM Olsen, Diego Meseguer Yebra, and Søren Kiil. Effects of biofouling development on drag forces of hull coatings for ocean-going ships: a review. *Journal of Coatings Technology and Research*, 12(3):415–444, 2015. doi: 10.1007/s11998-014-9651-2. URL https://link.springer.com/content/pdf/10.1007/s11998-014-9651-2.pdf.

[7] Alastair Marrion. *The chemistry and physics of coatings*. Royal Society of Chemistry, 2004.

[8] Qingyi Xie, Jiansen Pan, Chunfeng Ma, and Guangzhao Zhang. Dynamic surface antifouling: mechanism and systems. *Soft Matter*, 15(6):1087–1107, 2019. doi: 10.1039/c8sm01853g. URL https://pubs.rsc.org/en/content/articlepdf/2019/sm/c8sm01853g.

[9] Richard F. Piola, Katherine A. Dafforn, and Emma L. Johnston. The influence of antifouling practices on marine invasions. *Biofouling*, 25(7):633–644, 2009. doi: 10.1080/08927010903063065. URL https://doi.org/10.1080/08927010903063065. PMID: 20183122.

[10] Daniel J. Blackwood, Chin Sing Lim, Serena L.M. Teo, Xiaoping Hu, and Jianjun Pang. Macrofouling induced localized corrosion of stainless steel in singapore seawater. *Corrosion Science*, 129:152–160, 2017. ISSN 0010-938X. doi: https://doi.org/10.1016/j.corsci.2017.10.008. URL https://www.sciencedirect.com/science/article/pii/S0010938X17307837.

[11] Isla Fitridge, Tim Dempster, Jana Guenther, and Rocky de Nys. The impact and control of biofouling in marine aquaculture: a review. *Biofouling*, 28(7):649–669, 2012. doi: 10.1080/08927014.2012.700478. URL https://doi.org/10.1080/08927014.2012.700478. PMID: 22775076.

[12] John Hearin, Kelli Z. Hunsucker, Geoffrey Swain, Abraham Stephens, Harrison Gardner, Kody Lieberman, and Michael Harper. Analysis of long-term mechanical grooming on large-scale test panels coated with an antifouling and a fouling-release coating. *Biofouling*, 31(8):625–638, 2015. doi: 10.1080/08927014.2015.1081687. URL https://doi.org/10.1080/08927014.2015.1081687. PMID: 26359541.

[13] Hitoshi Wake, Hiromichi Takahashi, Toshihiro Takimoto, Hirokazu Takayanagi, Kinichi Ozawa, Hideo Kadoi, Mina Okochi, and Tadashi Matsunaga. Development of an electrochemical antifouling system for seawater cooling pipelines of power plants using titanium. *Biotechnology and bioengineering*, 95(3):468–473, 2006. doi: 10.1002/bit.21022. URL https://onlinelibrary.wiley.com/doi/abs/10.1002/bit.21022.

[14] I Kviatkovski, H Mamane, A Lakretz, I Sherman, D Beno-Moualem, and D Minz. Resistance of a multiple-isolate marine culture to ultraviolet c irradiation: inactivation vs biofilm formation. *Letters in applied microbiology*, 67(3):278–284, 2018. doi: 10.1111/lam.13032. URL https://sfamjournals.onlinelibrary.wiley.com/doi/full/10.1111/lam.13032.

[15] M. Legg, M.K. Yücel, I. Garcia de Carellan, V. Kappatos, C. Selcuk, and T.H. Gan. Acoustic methods for biofouling control: A review. *Ocean Engineering*, 103:237–247, 2015. ISSN 0029-8018. doi: https://doi.org/10.1016/j.oceaneng.2015.04.070. URL https://www.sciencedirect.com/science/article/pii/S0029801815001572.

[16] Modern approaches to marine antifouling coatings. *Surface and Coatings Technology*, 201(6):3642–3652, 2006. ISSN 0257-8972. doi: https://doi.org/10.1016/j.surfcoat.2006.08.129. URL https://www.sciencedirect.com/science/article/pii/S0257897206009364.

[17] Richard T. Carson, Maria Damon, Leigh T. Johnson, and Jamie A. Gonzalez. Conceptual issues in designing a policy to phase out metal-based antifouling paints on recreational boats in san diego bay. *Journal of Environmental Management*, 90(8):2460–2468, 2009. ISSN 0301-4797. doi: https://doi.org/10.1016/j.jenvman.2008.12.016. URL https://www.sciencedirect.com/science/article/pii/S0301479708003873.

[18] Shaobin Liu, Andrew Keong Ng, Rong Xu, Jun Wei, Cher Ming Tan, Yanhui Yang, and Yuan Chen. Antibacterial action of dispersed single-walled carbon nanotubes on escherichia coli and bacillus subtilis investigated by atomic force microscopy. *Nanoscale*, 2(12):2744–2750, 2010. doi: 10.1039/C0NR00441C. URL https://pubs.rsc.org/--/content/articlehtml/2010/nr/c0nr00441c.

[19] Omid Akhavan and Elham Ghaderi. Toxicity of graphene and graphene oxide nanowalls against bacteria. *ACS nano*, 4(10):5731–5736, 2010. doi: 10.1021/nn101390x. URL https://pubs.acs.org/doi/abs/10.1021/nn101390x.

[20] Changgu Lee, Xiaoding Wei, Jeffrey W. Kysar, and James Hone. Measurement of the elastic properties and intrinsic strength of monolayer graphene. *Science*, 321(5887):385–388, 2008. ISSN 0036-8075. doi: 10.1126/science.1157996. URL https://science.sciencemag.org/content/321/5887/385.

[21] Sasha Stankovich, Dmitriy A Dikin, Geoffrey HB Dommett, Kevin M Kohlhaas, Eric J Zimney, Eric A Stach, Richard D Piner, SonBinh T Nguyen, and Rodney S Ruoff. Graphene-based composite materials. *nature*, 442(7100):282–286, 2006. doi: 10.1038/nature04969. URL https://www.nature.com/articles/nature04969.

[22] Marita Kyllingstad. Coatings with anti-fouling properties. Specialisation project, Norwegian University of Science and Technology, 2020.

[23] Vicente J.D. Rascio. Antifouling coatings: Where do we go from here. *Corrosion Reviews*, 18(2-3):133–154, 2000. doi: doi:10.1515/CORRREV.2000.18.2-3.133. URL https://doi.org/10.1515/CORRREV.2000.18.2-3.133.

[24] Dr M Candries, Prof M Atlar, and Dr C D Anderson. Estimating the impact of new-generation antifoulings on ship performance: the presence of slime. *Journal of Marine Engineering & Technology*, 2(1):13–22, 2003. doi: 10.1080/20464177.2003.11020165. URL https://doi.org/10.1080/20464177.2003.11020165.

[25] Maria Salta, Julian A. Wharton, Yves Blache, Keith R. Stokes, and Jean-Francois Briand. Marine biofilms on artificial surfaces: structure and dynamics. *Environmental Microbiology*, 15(11):2879–2893, 2013. doi: https://doi.org/10.1111/1462-2920.12186. URL https://sfamjournals.onlinelibrary.wiley.com/doi/abs/10.1111/1462-2920.12186.

[26] Ji-Dong Gu. Microbiological deterioration and degradation of synthetic polymeric materials: recent research advances. *International Biodeterioration & Biodegradation*, 52(2):69–91, 2003. ISSN 0964-8305. doi: https://doi.org/10.1016/S0964-8305(02)00177-4. URL https://www.sciencedirect.com/science/article/pii/S0964830502001774.

[27] W.G. Characklis and K.E. Cooksey. Biofilms and microbial fouling. In Allen I. Laskin, editor, *Advances in applied microbiology*, volume 29 of *Advances in Applied Microbiology*, pages 93 – 138. Academic Press, 1983. doi: https://doi.org/10.1016/S0065-2164(08)70355-1. URL http://www.sciencedirect.com/science/article/pii/S0065216408703551.

[28] Mary Ellen Davey and George A. O'toole. Microbial biofilms: from ecology to molecular genetics. *Microbiology and Molecular Biology Reviews*, 64(4):847–867, 2000. ISSN 1092-2172. doi: 10.1128/MMBR.64.4.847-867.2000. URL https://mmbr.asm.org/content/64/4/847.

[29] Sibylle Abarzua and Sabiene Jakubowski. Biotechnological investigation for the prevention of biofouling. i. biological and biochemical principles for the prevention of biofouling. *Marine Ecology Progress Series*, 123:301–312, 1995. doi: 10.3354/meps123301. URL http://www.int-res.com/abstracts/meps/v123/p301-312/.

[30] Maria Salta, Julian A. Wharton, Yves Blache, Keith R. Stokes, and Jean-Francois Briand. Marine biofilms on artificial surfaces: structure and dynamics. *Environmental Microbiology*, 15(11):2879–2893, 2013. doi: https://doi.org/10.1111/1462-2920.12186. URL https://sfamjournals.onlinelibrary.wiley.com/doi/abs/10.1111/1462-2920.12186.

[31] Maureen E Callow and James A Callow. Marine biofouling: a sticky problem. *Biologist*, 49(1):1–5, 2002. ISSN 0006-3347. URL http://biosciences-labs.bham.ac.uk/callowj/PDF%20files/iob.pdf.

[32] KE Cooksey and B Wigglesworth-Cooksey. Adhesion of bacteria and diatoms to surfaces in the sea: a review. *Aquatic microbial ecology*, 9(1):87–96, 1995. ISSN 1616-1564. doi: https://doi.org/10.3354/ame009087. URL https://www.int-res.com/abstracts/ame/v09/n1/p87-96/.

[33] D. Roberts, D. Rittschof, E. Holm, and A.R. Schmidt. Factors influencing initial larval settlement: temporal, spatial and surface molecular components. *Journal of Experimental Marine Biology and Ecology*, 150(2):203–221, 1991. ISSN 0022-0981. doi: https://doi.org/10.1016/0022-0981(91)90068-8. URL https://www.sciencedirect.com/science/article/pii/0022098191900688.

[34] George O'Toole, Heidi B. Kaplan, and Roberto Kolter. Biofilm formation as microbial development. *Annual Review of Microbiology*, 54(1):49–79, 2000. doi: 10.1146/annurev.micro.54.1.49. URL https://doi.org/10.1146/annurev.micro.54.1.49. PMID: 11018124.

[35] Sharron Mceldowney and Madilyn Fletcher. Effect of growth conditions and surface characteristics of aquatic bacteria on their attachment to solid surfaces. *Microbiology*, 132(2):513–523, 1986. ISSN 1350-0872. doi: https://doi.org/10.1099/00221287-132-2-513. URL https://www.microbiologyresearch.org/content/journal/micro/10.1099/00221287-132-2-513.

[36] P-Y Qian, Stanley CK Lau, H-U Dahms, Sergey Dobretsov, and Timm Harder. Marine biofilms as mediators of colonization by marine macroorganisms: implications for antifouling and aquaculture. *Marine Biotechnology*, 9(4):401, 2007. doi: 10.1007/s10126-007-9001-9. URL https://link.springer.com/content/pdf/10.1007/s10126-007-9001-9.pdf.

[37] A A Massol-Deyá, J Whallon, R F Hickey, and J M Tiedje. Channel structures in aerobic biofilms of fixed-film reactors treating contaminated groundwater. *Applied and Environmental Microbiology*, 61(2):769–777, 1995. ISSN 0099-2240. URL https://aem.asm.org/content/61/2/769.

[38] Paul J. Molino and Richard Wetherbee. The biology of biofouling diatoms and their role in the development of microbial slimes. *Biofouling*, 24(5):365–379, 2008. doi: 10.1080/08927010802254583. URL https://doi.org/10.1080/08927010802254583.

[39] Luanne Hall-Stoodley, J William Costerton, and Paul Stoodley. Bacterial biofilms: from the natural environment to infectious diseases. *Nature reviews microbiology*, 2(2):95–108, 2004. ISSN 1740-1534. doi: 10.1038/nrmicro821. URL https://doi.org/10.1038/nrmicro821.

[40] Trishul Artham, M. Sudhakar, R. Venkatesan, C. Madhavan Nair, K.V.G.K. Murty, and Mukesh Doble. Biofouling and stability of synthetic polymers in sea water. *International Biodeterioration and Biodegradation*, 63(7):884–890, 2009. ISSN 0964-8305. doi: https://doi.org/10.1016/j.ibiod.2009.03.003. URL https://www.sciencedirect.com/science/article/pii/S0964830509000420. 14th International Biodeterioration and BiodegradationSymposium.

[41] Franck Cassé and Geoffrey W. Swain. The development of microfouling on four commercial antifouling coatings under static and dynamic immersion. *International Biodeterioration & Biodegradation*, 57(3): 179–185, 2006. ISSN 0964-8305. doi: https://doi.org/10.1016/j.ibiod.2006.02.008. URL https://www.sciencedirect.com/science/article/pii/S0964830506000394.

[42] Inga Hense and Aike Beckmann. A theoretical investigation of the diatom cell size reduction–restitution cycle. *Ecological Modelling*, 317:66–82, 2015. ISSN 0304-3800. doi: https://doi.org/10.1016/j.ecolmodel.2015.09.003. URL https://www.sciencedirect.com/science/article/pii/S030438001500410X.

[43] David G Mann and F Round. Why didn't lund see sex in asterionella? a discussion of the diatom life cycle in nature. *Algae and the aquatic environment*, 29: 385–412, 1988. URL https://www.researchgate.net/profile/David-Mann-12/publication/262417363_Why_didn%27t_Lund_see_sex_in_Asterionella_A_discussion_of_the_diatom_life_cycle_in_nature/links/545393c60cf26d5090a54771/Why-didnt-Lund-see-sex-in-Asterionella-A-discussion-of-the-diatom-life-cycle-in-nature.pdf.

[44] D R Absolom, F V Lamberti, Z Policova, W Zingg, C J van Oss, and A W Neumann. Surface thermodynamics of bacterial adhesion. *Applied and Environmental Microbiology*, 46(1):90–97, 1983. doi: 10.1128/aem.46.1.90-97.1983. URL https://journals.asm.org/doi/abs/10.1128/aem.46.1.90-97.1983.

[45] Y.S. Cao and G.J. Alaerts. Influence of reactor type and shear stress on aerobic biofilm morphology, population and kinetics. *Water Research*, 29(1):107 – 118, 1995. ISSN 0043-1354. doi: https://doi.org/10.1016/0043-1354(94)00136-U. URL http://www.sciencedirect.com/science/article/pii/004313549400136U.

[46] Tarek Ahmed. Chapter 4 - fundamentals of rock properties. In Tarek Ahmed, editor, *Reservoir Engineering Handbook (Fifth Edition)*, pages 167–281. Gulf Professional Publishing, fifth edition edition, 2019. ISBN 978-0-12-813649-2. doi: https://doi.org/10.1016/B978-0-12-813649-2.00004-9. URL https://www.sciencedirect.com/science/article/pii/B9780128136492000049.

[47] Madilyn Fletcher and G. I. Loeb. Influence of substratum characteristics on the attachment of a marine pseudomonad to solid surfaces. *Applied and Environmental Microbiology*, 37(1):68–71, 1979. ISSN 0099-2240. URL https://aem.asm.org/content/37/1/67.

[48] C Shea, JW Nunley, JC Williamson, and HE Smith-Somerville. Comparison of the adhesion properties of deleya marina and the exopolysaccharide-defective mutant strain dmr. *Applied and environmental microbiology*, 57(11):3107–3113, 1991. URL https://aem.asm.org/content/57/11/3107.short.

[49] Diego Meseguer Yebra, Søren Kiil, Claus E. Weinell, and Kim Dam-Johansen. Presence and effects of marine microbial biofilms on biocide-based antifouling paints. *Biofouling*, 22(1):33–41, 2006. doi: 10.1080/08927010500519097. URL https://doi.org/10.1080/08927010500519097. PMID: 16551559.

[50] Q. Zhao, Y. Liu, C. Wang, S. Wang, and H. Müller-Steinhagen. Effect of surface free energy on the adhesion of biofouling and crystalline fouling. *Chemical Engineering Science*, 60(17):4858–4865, 2005. ISSN 0009-2509. doi: https://doi.org/10.1016/j.ces.2005.04.006. URL https://www.sciencedirect.com/science/article/pii/S0009250905002976.

[51] Michael P Schultz. Frictional resistance of antifouling coating systems. *J. Fluids Eng.*, 126(6):1039–1047, 2004. doi: https://doi.org/10.1115/1.1845552. URL https://asmedigitalcollection.asme.org/fluidsengineering/article/126/6/1039/463691/Frictional-Resistance-of-Antifouling-Coating?casa_token=Ej3Zj4m-IMwAAAAA:bRb8rGKXA2RNxZsQJs5XrvwQtx3xZTtsJB4BZ-AlcdXL3rI_Jgbd4H2kFNcgAqyttUoCdB_xug.

[52] Richard Elsmore. Biocide regulation in the eu–past, present and future. *Chim OGGI Chem Today*, 30:58–60, 2012. URL https://www.teknoscienze.com/Contents/Riviste/PDF/CO3_2012_RGB_60-63.pdf.

[53] Yu Ping Su, Lee Nuang Sim, Xin Li, Hans G.L. Coster, and Tzyy Haur Chong. Anti-fouling piezoelectric pvdf membrane: Effect of morphology on dielectric and piezoelectric properties. *Journal of Membrane Science*, 620:118818, 2021. ISSN 0376-7388. doi: https://doi.org/10.1016/j.memsci.2020.118818. URL https://www.sciencedirect.com/science/article/pii/S0376738820313934.

[54] *Anti-Fouling Silicone Elastomers for Offshore Structures*, volume All Days of *NACE CORROSION*, 03 2006.

[55] Michael A Champ. The status of the treaty to ban tbt in marine antifouling paints and alternatives. In *Proceedings of the 24th UJNR (US/Japan) Marine Facilities Panel Meeting, Hawaii*, 2001.

[56] Michael A Champ. Economic and environmental impacts on ports and harbors from the convention to ban harmful marine anti-fouling systems. *Marine Pollution Bulletin*, 46(8):935 – 940, 2003. ISSN 0025-326X. doi: https://doi.org/10.1016/S0025-326X(03)00106-1. URL http://www.sciencedirect.com/science/article/pii/S0025326X03001061.

[57] D Claisse and Cl Alzieu. Copper contamination as a result of antifouling paint regulations? *Marine Pollution Bulletin*, 26(7):395–397, 1993. ISSN 0025-326X. doi: https://doi.org/10.1016/0025-326X(93)90188-P. URL https://www.sciencedirect.com/science/article/pii/0025326X9390188P.

[58] Gregor Grass, Christopher Rensing, and Marc Solioz. Metallic copper as an antimicrobial surface. *Applied and Environmental Microbiology*, 77(5):1541–1547, 2011. doi: 10.1128/AEM.02766-10. URL https://journals.asm.org/doi/abs/10.1128/AEM.02766-10.

[59] M.J Cowling, T Hodgkiess, A.C.S Parr, M.J Smith, and S.J Marrs. An alternative approach to antifouling based on analogues of natural processes. *Science of The Total Environment*, 258(1):129–137, 2000. ISSN 0048-9697. doi: https://doi.org/10.1016/S0048-9697(00)00513-1. URL https://www.sciencedirect.com/science/article/pii/S0048969700005131. TBT Costs and Benefits- A.

[60] Nimisha Singh and Andrew Turner. Leaching of copper and zinc from spent antifouling paint particles. *Environmental Pollution*, 157(2):371–376, 2009. ISSN 0269-7491. doi: https://doi.org/10.1016/j.envpol.2008.10.003. URL https://www.sciencedirect.com/science/article/pii/S0269749108005186.

[61] Haiqun Chen, Marc B Müller, Kerry J Gilmore, Gordon G Wallace, and Dan Li. Mechanically strong, electrically conductive, and biocompatible graphene paper. *Advanced Materials*, 20(18):3557–3561, 2008. doi: 10.1002/adma.200800757. URL https://onlinelibrary.wiley.com/doi/epdf/10.1002/adma.200800757.

[62] Wenbing Hu, Cheng Peng, Weijie Luo, Min Lv, Xiaoming Li, Di Li, Qing Huang, and Chunhai Fan. Graphene-based antibacterial paper. *ACS Nano*, 4(7):4317–4323, 2010. doi: 10.1021/nn101097v. URL https://doi.org/10.1021/nn101097v. PMID: 20593851.

[63] Wei Gao. *The Chemistry of Graphene Oxide*, pages 61–95. Springer International Publishing, Cham, 2015. ISBN 978-3-319-15500-5. doi: 10.1007/978-3-319-15500-5_3. URL https://doi.org/10.1007/978-3-319-15500-5_3.

[64] Konstantin S Novoselov, VI Fal, L Colombo, PR Gellert, MG Schwab, K Kim, et al. A roadmap for graphene. *nature*, 490(7419):192–200, 2012. doi: 10.1038/nature11458. URL https://www.nature.com/articles/nature11458.

[65] Agnieszka Iwan and Andrzej Chuchmała. Perspectives of applied graphene: Polymer solar cells. *Progress in Polymer Science*, 37(12):1805–1828, 2012. ISSN 0079-6700. doi: https://doi.org/10.1016/j.progpolymsci.2012.08.001. URL https://www.sciencedirect.com/science/article/pii/S0079670012000822.

[66] A. K. Geim. Graphene: Status and prospects. *Science*, 324(5934):1531, 2009. ISSN 0036-8075. doi: 10.1126/science.1158877. URL https://science.sciencemag.org/content/324/5934/1530.

[67] Yanwu Zhu, Shanthi Murali, Weiwei Cai, Xuesong Li, Ji Won Suk, Jeffrey R. Potts, and Rodney S. Ruoff. Graphene and graphene oxide: Synthesis, properties, and applications. *Advanced Materials*, 22 (35):3906–3924, 2010. doi: https://doi.org/10.1002/adma.201001068. URL https://onlinelibrary.wiley.com/doi/abs/10.1002/adma.201001068.

[68] Kostya S Novoselov, Andre K Geim, Sergei Vladimirovich Morozov, Dingde Jiang, Michail I Katsnelson, IVa Grigorieva, SVb Dubonos, and A. A. Firsov. Two-dimensional gas of massless dirac fermions in graphene. *nature*, 438(7065):199, 2005. doi: https://doi.org/10.1038/nature04233. URL https://www.nature.com/articles/nature04233.

[69] Alexander A. Balandin, Suchismita Ghosh, Wenzhong Bao, Irene Calizo, Desalegne Teweldebrhan, Feng Miao, and Chun Ning Lau. Superior thermal conductivity of single-layer graphene. *Nano Letters*, 8 (3):902–907, 2008. doi: 10.1021/nl0731872. URL https://doi.org/10.1021/nl0731872. PMID: 18284217.

[70] Haiming Huang, Zhibing Li, Juncong She, and Weiliang Wang. Oxygen density dependent band gap of reduced graphene oxide. *Journal of Applied Physics*, 111(5):054317, 2012. doi: 10.1063/1.3694665. URL https://doi.org/10.1063/1.3694665.

[71] Dimitrios G. Papageorgiou, Ian A. Kinloch, and Robert J. Young. Mechanical properties of graphene and graphene-based nanocomposites. *Progress in Materials Science*, 90:75–127, 2017. ISSN 0079-6425. doi: https://doi.org/10.1016/j.pmatsci.2017.07.004. URL https://www.sciencedirect.com/science/article/pii/S0079642517300968.

[72] Renju Zacharia, Hendrik Ulbricht, and Tobias Hertel. Interlayer cohesive energy of graphite from thermal desorption of polyaromatic hydrocarbons. *Phys. Rev. B*, 69:155406, Apr 2004. doi: 10.1103/PhysRevB.69.155406. URL https://link.aps.org/doi/10.1103/PhysRevB.69.155406.

[73] Anton Lerf, Heyong He, Michael Forster, and Jacek Klinowski. Structure of graphite oxide revisited. *The Journal of Physical Chemistry B*, 102(23):4477–4482, 1998. doi: 10.1021/jp9731821. URL https://doi.org/10.1021/jp9731821.

[74] Vasilios Georgakilas, Michal Otyepka, Athanasios B. Bourlinos, Vimlesh Chandra, Namdong Kim, K. Christian Kemp, Pavel Hobza, Radek Zboril, and Kwang S. Kim. Functionalization of graphene: Covalent and non-covalent approaches, derivatives and applications. *Chemical Reviews*, 112(11):6156–6214, 2012. doi: 10.1021/cr3000412. URL https://doi.org/10.1021/cr3000412. PMID: 23009634.

[75] Dimitrios Konios, Minas M. Stylianakis, Emmanuel Stratakis, and Emmanuel Kymakis. Dispersion behaviour of graphene oxide and reduced graphene oxide. *Journal of Colloid and Interface Science*, 430:108–112, 2014. ISSN 0021-9797. doi: https://doi.org/10.1016/j.jcis.2014.05.033. URL https://www.sciencedirect.com/science/article/pii/S0021979714003397.

[76] Wei Gao, Lawrence B Alemany, Lijie Ci, and Pulickel M Ajayan. New insights into the structure and reduction of graphite oxide. *Nature chemistry*, 1(5):403–408, 2009. doi: https://doi.org/10.1038/nchem.281. URL https://www.nature.com/articles/nchem.281.

[77] Cecilia Mattevi, Goki Eda, Stefano Agnoli, Steve Miller, K. Andre Mkhoyan, Ozgur Celik, Daniel Mastrogiovanni, Gaetano Granozzi, Eric Garfunkel, and Manish Chhowalla. Evolution of electrical, chemical, and structural properties of transparent and conducting chemically derived graphene thin films. *Advanced Functional Materials*, 19(16):2577–2583, 2009. doi: https://doi.org/10.1002/adfm.200900166. URL https://onlinelibrary.wiley.com/doi/abs/10.1002/adfm.200900166.

[78] Shaobin Liu, Tingying Helen Zeng, Mario Hofmann, Ehdi Burcombe, Jun Wei, Rongrong Jiang, Jing Kong, and Yuan Chen. Antibacterial activity of graphite, graphite oxide, graphene oxide, and reduced graphene oxide: Membrane and oxidative stress. *ACS Nano*, 5(9):6971–6980, 2011. doi: 10.1021/nn202451x. URL https://doi.org/10.1021/nn202451x. PMID: 21851105.

[79] Juanni Chen, Hui Peng, Xiuping Wang, Feng Shao, Zhaodong Yuan, and Heyou Han. Graphene oxide exhibits broad-spectrum antimicrobial activity against bacterial phytopathogens and fungal conidia by intertwining and membrane perturbation. *Nanoscale*, 6(3):1879–1889, 2014. doi: 10.1039/C3NR04941H. URL https://pubs.rsc.org/en/content/articlehtml/2014/nr/c3nr04941h?casa_token=PGcOsqZ5yKIAAAAA:rkZNEp3mb-9AFTppu4G7DZqsh31BjxpiZHuVuvcvd_AvGgGkJ0RFpiwI2Tm1i4vq0OcEfcT0GBW1u7s.

[80] Yusong Tu, Min Lv, Peng Xiu, Tien Huynh, Meng Zhang, Matteo Castelli, Zengrong Liu, Qing Huang, Chunhai Fan, Haiping Fang, et al. Destructive extraction of phospholipids from escherichia coli membranes by graphene nanosheets. *Nature nanotechnology*, 8(8):594, 2013. doi: 10.1038/NNANO.2013.125. URL https://www.nature.com/articles/nnano.2013.125.pdf?origin=ppub.

[81] Jaewoo Lee, Hee-Ro Chae, Young June Won, Kibaek Lee, Chung-Hak Lee, Hong H. Lee, In-Chul Kim, and Jong min Lee. Graphene oxide nanoplatelets composite membrane with hydrophilic and antifouling properties for wastewater treatment. *Journal of Membrane Science*, 448:223–230, 2013. ISSN 0376-7388. doi: https://doi.org/10.1016/j.memsci.2013.08.017. URL https://www.sciencedirect.com/science/article/pii/S0376738813006637.

[82] Shaobin Liu, Ming Hu, Tingying Helen Zeng, Ran Wu, Rongrong Jiang, Jun Wei, Liang Wang, Jing Kong, and Yuan Chen. Lateral dimension-dependent antibacterial activity of graphene oxide sheets. *Langmuir*, 28(33):12364–12372, 2012. doi: 10.1021/la3023908. URL https://doi.org/10.1021/la3023908. PMID: 22827339.

[83] Haiwei Ji, Hanjun Sun, and Xiaogang Qu. Antibacterial applications of graphene-based nanomaterials: Recent achievements and challenges. *Advanced Drug Delivery Reviews*, 105:176–189, 2016. ISSN 0169-409X. doi: https://doi.org/10.1016/j.addr.2016.04.009. URL https://www.sciencedirect.com/science/article/pii/S0169409X16301089. Graphene-based materials in nanomedicine.

[84] Xiaoming Sun, Zhuang Liu, Kevin Welsher, Joshua Tucker Robinson, Andrew Goodwin, Sasa Zaric, and Hongjie Dai. Nano-graphene oxide for cellular imaging and drug delivery. *Nano research*, 1(3):203–212, 2008. doi: 10.1007/s12274-008-8021-8. URL https://link.springer.com/article/10.1007%252Fs12274-008-8021-8#citeas.

[85] Zhuang Liu, Joshua T. Robinson, Xiaoming Sun, and Hongjie Dai. Pegylated nanographene oxide for delivery of water-insoluble cancer drugs. *Journal of the American Chemical Society*, 130(33):10876–10877, 2008. doi: 10.1021/ja803688x. URL https://doi.org/10.1021/ja803688x. PMID: 18661992.

[86] Ken-Hsuan Liao, Yu-Shen Lin, Christopher W. Macosko, and Christy L. Haynes. Cytotoxicity of graphene oxide and graphene in human erythrocytes and skin fibroblasts. *ACS Applied Materials & Interfaces*, 3(7):2607–2615, 2011. doi: 10.1021/am200428v. URL https://doi.org/10.1021/am200428v. PMID: 21650218.

[87] Vy T. H. Pham, Vi Khanh Truong, Matthew D. J. Quinn, Shannon M. Notley, Yachong Guo, Vladimir A. Baulin, Mohammad Al Kobaisi, Russell J. Crawford, and Elena P. Ivanova. Graphene induces formation of pores that kill spherical and rod-shaped bacteria. *ACS Nano*, 9(8):8458–8467, 2015. doi: 10.1021/acsnano.5b03368. URL https://doi.org/10.1021/acsnano.5b03368. PMID: 26166486.

[88] O. Akhavan, E. Ghaderi, and A. Esfandiar. Wrapping bacteria by graphene nanosheets for isolation from environment, reactivation by sonication, and inactivation by near-infrared irradiation. *The Journal of Physical Chemistry B*, 115(19):6279–6288, 2011. doi: 10.1021/jp200686k. URL https://doi.org/10.1021/jp200686k. PMID: 21513335.

[89] Karthikeyan Krishnamoorthy, Murugan Veerapandian, Ling-He Zhang, Kyusik Yun, and Sang Jae Kim. Antibacterial efficiency of graphene nanosheets against pathogenic bacteria via lipid peroxidation. *The Journal of Physical Chemistry C*, 116(32):17280–17287, 2012. doi: 10.1021/jp3047054. URL https://doi.org/10.1021/jp3047054.

[90] Sangiliyandi Gurunathan, Jae Woong Han, Ahmed Abdal Dayem, Vasuki Eppakayala, Mi-Ryung Park, Deug-Nam Kwon, and Jin-Hoi Kim. Antibacterial activity of dithiothreitol reduced graphene oxide. *Journal of Industrial and Engineering Chemistry*, 19(4):1280–1288, 2013. ISSN 1226-086X. doi: https://doi.org/10.1016/j.jiec.2012.12.029. URL https://www.sciencedirect.com/science/article/pii/S1226086X12004492.

[91] Jinhua Li, Gang Wang, Hongqin Zhu, Miao Zhang, Xiaohu Zheng, Zengfeng Di, Xuanyong Liu, and Xi Wang. Antibacterial activity of large-area monolayer graphene film manipulated by charge transfer. *Scientific reports*, 4(1):1–8, 2014. doi: 10.1038/srep04359. URL https://www.nature.com/articles/srep04359.

[92] Jian Gao, Fang Liu, Yiliu Liu, Ning Ma, Zhiqiang Wang, and Xi Zhang. Environment-friendly method to produce graphene that employs vitamin c and amino acid. *Chemistry of Materials*, 22(7):2213–2218, 2010. doi: 10.1021/cm902635j. URL https://doi.org/10.1021/cm902635j.

[93] H. W. Harris, M. Y. El-Naggar, O. Bretschger, M. J. Ward, M. F. Romine, A. Y. Obraztsova, and K. H. Nealson. Electrokinesis is a microbial behavior that requires extracellular electron transport. *Proceedings of the National Academy of Sciences*, 107(1):326–331, 2010. ISSN 0027-8424. doi: 10.1073/pnas.0907468107. URL https://www.pnas.org/content/107/1/326.

[94] Florian Banhart and Pulickel M Ajayan. Carbon onions as nanoscopic pressure cells for diamond formation. *Nature*, 382(6590):433–435, 1996. doi: 10.1038/382433a0. URL https://doi.org/10.1038/382433a0.

[95] Alfonso Pompella, Athanase Visvikis, Aldo Paolicchi, Vincenzo De Tata, and Alessandro F. Casini. The changing faces of glutathione, a cellular protagonist. *Biochemical Pharmacology*, 66(8):1499–1503, 2003. ISSN 0006-2952. doi: https://doi.org/10.1016/S0006-2952(03)00504-5. URL https://www.sciencedirect.com/science/article/pii/S0006295203005045. Apoptosis - from Signalling Pathways to Therapeutic Tools.

[96] Ole Øystein Knudsen and Amy Forsgren. *Corrosion control through organic coatings*, pages 11–16, 26–27, 89–104, 149–151. CRC Press, second edition, 2017.

[97] Phuong Nguyen-Tri, Tuan Anh Nguyen, Pascal Carriere, and Cuong Ngo Xuan. Nanocomposite coatings: preparation, characterization, properties, and applications. *International Journal of Corrosion*, 2018, 2018. doi: 10.1155/2018/4749501. URL https://www.hindawi.com/journals/ijc/2018/4749501/.

[98] Massimo Guglielmi, Guido Kickelbick, and Alessandro Martucci. *Sol-Gel Nanocomposites*. Springer, 2014.

[99] Paul J Flory. *Principles of polymer chemistry*. Cornell University Press, 1953.

[100] L.E.S. Brink, S.J.G. Elbers, T. Robbertsen, and P. Both. The anti-fouling action of polymers preadsorbed on ultrafiltration and microfiltration membranes. *Journal of Membrane Science*, 76(2):281–291, 1993. ISSN 0376-7388. doi: https://doi.org/10.1016/0376-7388(93)85225-L. URL https://www.sciencedirect.com/science/article/pii/037673889385225L.

[101] Mohammad Moniruzzaman and Karen I. Winey. Polymer nanocomposites containing carbon nanotubes. *Macromolecules*, 39(16):5194–5205, 2006. doi: 10.1021/ma060733p. URL https://doi.org/10.1021/ma060733p.

[102] J. Zhu, H. Peng, F. Rodriguez-Macias, J.L. Margrave, V.N. Khabashesku, A.M. Imam, K. Lozano, and E.V. Barrera. Reinforcing epoxy polymer composites through covalent integration of functionalized nanotubes. *Advanced Functional Materials*, 14(7):643–648, 2004. doi: https://doi.org/10.1002/adfm.200305162. URL https://onlinelibrary.wiley.com/doi/abs/10.1002/adfm.200305162.

[103] L. S. Schadler, S. C. Giannaris, and P. M. Ajayan. Load transfer in carbon nanotube epoxy composites. *Applied Physics Letters*, 73(26):3842–3844, 1998. doi: 10.1063/1.122911. URL https://doi.org/10.1063/1.122911.

[104] Jiang Zhu, JongDae Kim, Haiqing Peng, John L. Margrave, Valery N. Khabashesku, and Enrique V. Barrera. Improving the dispersion and integration of single-walled carbon nanotubes in epoxy composites through functionalization. *Nano Letters*, 3(8):1107–1113, 2003. doi: 10.1021/nl0342489. URL https://doi.org/10.1021/nl0342489.

[105] Guozhong Cao and Ying Wang. *Nanostructures and nanomaterials*, volume 2. World Scientific, 2011.

[106] Paul Calvert. A recipe for strength. *Nature*, 399(6733):210–211, 1999. doi: 10.1038/20326. URL https://www.nature.com/articles/20326#citeas.

[107] J Sandler, M.S.P Shaffer, T Prasse, W Bauhofer, K Schulte, and A.H Windle. Development of a dispersion process for carbon nanotubes in an epoxy matrix and the resulting electrical properties. *Polymer*, 40(21): 5967–5971, 1999. ISSN 0032-3861. doi: https://doi.org/10.1016/S0032-3861(99)00166-4. URL https://www.sciencedirect.com/science/article/pii/S0032386199001664.

[108] P. M. Ajayan, L. S. Schadler, C. Giannaris, and A. Rubio. Single-walled carbon nanotube–polymer composites: Strength and weakness. *Advanced Materials*, 12(10):750–753, 2000. doi: https://doi.org/10.1002/(SICI)1521-4095(200005)12:10<750::AID-ADMA750>3.0.CO;2-6. URL https://onlinelibrary.wiley.com/doi/abs/10.1002/%28SICI%291521-4095%28200005%2912%3A10%3C750%3A%3AAID-ADMA750%3E3.0.CO%3B2-6.

[109] P. Kuzhir, A. Paddubskaya, D. Bychanok, A. Nemilentsau, M. Shuba, A. Plusch, S. Maksimenko, S. Bellucci, L. Coderoni, F. Micciulla, I. Sacco, G. Rinaldi, J. Macutkevic, D. Seliuta, G. Valusis, and J. Banys. Microwave probing of nanocarbon based epoxy resin composite films: Toward electromagnetic shielding. *Thin Solid Films*, 519(12):4114–4118, 2011. ISSN 0040-6090. doi: https://doi.org/10.1016/j.tsf.2011.01.198. URL https://www.sciencedirect.com/science/article/pii/S0040609011002574. Carbon- or Nitrogen-Containing Nanostructured Composite Films.

[110] S. Chatterjee, J.W. Wang, W.S. Kuo, N.H. Tai, C. Salzmann, W.L. Li, R. Hollertz, F.A. Nüesch, and B.T.T. Chu. Mechanical reinforcement and thermal conductivity in expanded graphene nanoplatelets reinforced epoxy composites. *Chemical Physics Letters*, 531:6–10, 2012. ISSN 0009-2614. doi: https://doi.org/10.1016/j.cplett.2012.02.006. URL https://www.sciencedirect.com/science/article/pii/S0009261412001789.

[111] Olga A. Amariutei, Roderick Ramsdale-Capper, Mariana Correa Álvarez, Louise K.Y. Chan, and Joel P. Foreman. Modelling the properties of a difunctional epoxy resin cured with aromatic diamine isomers. *Polymer*, 156:203–213, 2018. ISSN 0032-3861. doi: https://doi.org/10.1016/j.polymer.2018.10.016. URL https://www.sciencedirect.com/science/article/pii/S0032386118309327.

[112] T.H. Wu, A. Foyet, A. Kodentsov, L.G.J. van der Ven, R.A.T.M. van Benthem, and G. de With. Wet adhesion of epoxy–amine coatings on 2024-t3 aluminum alloy. *Materials Chemistry and Physics*, 145(3): 342–349, 2014. ISSN 0254-0584. doi: https://doi.org/10.1016/j.matchemphys.2014.02.022. URL https://www.sciencedirect.com/science/article/pii/S0254058414001126.

[113] K. Dušek, M. Ilavský, and S. Luňak. Curing of epoxy resins. i. statistics of curing of diepoxides with diamines. *Journal of Polymer Science: Polymer Symposia*, 53(1):29–44, 1975. doi: https://doi.org/10.1002/polc.5070530107. URL https://onlinelibrary.wiley.com/doi/abs/10.1002/polc.5070530107.

[114] D. J. Plazek and Z. N. Frund Jr. Epoxy resins (dgeba): The curing and physical aging process. *Journal of Polymer Science Part B: Polymer Physics*, 28(4):431–448, 1990. doi: https://doi.org/10.1002/polb.1990.090280401. URL https://onlinelibrary.wiley.com/doi/abs/10.1002/polb.1990.090280401.

[115] A.S. Argon and R.E. Cohen. Toughenability of polymers. *Polymer*, 44(19):6013–6032, 2003. ISSN 0032-3861. doi: https://doi.org/10.1016/S0032-3861(03)00546-9. URL https://www.sciencedirect.com/science/article/pii/S0032386103005469. In Honour of Ian Ward's 75th Birthday.

[116] Suneev Anil Bansal, Amrinder Pal Singh, Anil Kumar, Suresh Kumar, Navin Kumar, and Jatinder Kumar Goswamy. Improved mechanical performance of bisphenol-a graphene-oxide nano-composites. *Journal of Composite Materials*, 52(16):2179–2188, 2018. doi: 10.1177/0021998317741952. URL https://doi.org/10.1177/0021998317741952.

[117] Ye Fu, Wencai Wang, Liqun Zhang, Vladimir Vinokurov, Anna Stavitskaya, and Yuri Lvov. Development of marine antifouling epoxy coating enhanced with clay nanotubes. *Materials*, 12(24), 2019. ISSN 1996-1944. doi: 10.3390/ma12244195. URL https://www.mdpi.com/1996-1944/12/24/4195.

[118] T.P. Nguyen, C.W. Lee, S. Hassen, and H.C. Le. Hybrid nanocomposites for optical applications. *Solid State Sciences*, 11(10):1810–1814, 2009. ISSN 1293-2558. doi: https://doi.org/10.1016/j.solidstatesciences.2009.05.011. URL https://www.sciencedirect.com/science/article/pii/S1293255809001794. E-MRS Spring Meeting 2008.

[119] Shatakshi Verma, Smita Mohanty, and SK Nayak. Preparation of hydrophobic epoxy–polydimethylsiloxane–graphene oxide nanocomposite coatings for antifouling application. *Soft Matter*, 16(5):1211–1226, 2020. doi: 10.1039/C9SM01952A. URL https://pubs.rsc.org/en/content/articlehtml/2020/sm/c9sm01952a.

[120] Stephanie M. Bennett, John A. Finlay, Nikhil Gunari, David D. Wells, Anne E. Meyer, Gilbert C. Walker, Maureen E. Callow, James A. Callow, Frank V. Bright, and Michael R. Detty. The role of surface energy and water wettability in aminoalkyl/fluorocarbon/hydrocarbon-modified xerogel surfaces in the control of marine biofouling. *Biofouling*, 26(2):235–246, 2009. doi: 10.1080/08927010903469676. URL https://doi.org/10.1080/08927010903469676. PMID: 19960390.

[121] R Holland, T M Dugdale, R Wetherbee, A B Brennan, J A Finlay, J A Callow, and Maureen E Callow. Adhesion and motility of fouling diatoms on a silicone elastomer. *Biofouling*, 20(6):323–329, 2004. doi: 10.1080/08927010400029031. URL https://doi.org/10.1080/08927010400029031. PMID: 15804716.

[122] Rasheed Atif, Islam Shyha, and Fawad Inam. Mechanical, thermal, and electrical properties of graphene-epoxy nanocomposites—a review. *Polymers*, 8(8), 2016. ISSN 2073-4360. doi: 10.3390/polym8080281. URL https://www.mdpi.com/2073-4360/8/8/281.

[123] Scott Gilje, Song Han, Minsheng Wang, Kang L. Wang, and Richard B. Kaner. A chemical route to graphene for device applications. *Nano Letters*, 7(11):3394–3398, 2007. doi: 10.1021/nl0717715. URL https://doi.org/10.1021/nl0717715. PMID: 17944523.

[124] S.K. Singh, S.P. Tambe, V.S. Raja, and Dhirendra Kumar. Thermally sprayable polyethylene coatings for marine environment. *Progress in Organic Coatings*, 60(3):186–193, 2007. ISSN 0300-9440. doi: https://doi.org/10.1016/j.porgcoat.2007.07.028. URL https://www.sciencedirect.com/science/article/pii/S0300944007001592.

[125] Viet Hung Pham, Tran Viet Cuong, Seung Hyun Hur, Eun Woo Shin, Jae Seong Kim, Jin Suk Chung, and Eui Jung Kim. Fast and simple fabrication of a large transparent chemically-converted graphene film by spray-coating. *Carbon*, 48(7):1945–1951, 2010. ISSN 0008-6223. doi: https://doi.org/10.1016/j.carbon.2010.01.062. URL https://www.sciencedirect.com/science/article/pii/S0008622310000965.

[126] Dainius Perednis and Ludwig J Gauckler. Thin film deposition using spray pyrolysis. *Journal of electroceramics*, 14(2):103–111, 2005. doi: 10.1007/s10832. URL https://link.springer.com/content/pdf/10.1007/s10832-005-0870-x.pdf.

[127] Sneha Sheokand, Vishruth Reddy, and Arvind K Bansal. Pharmaceutical nanocrystals: From fundamentals to advances. *Pharma Times*, 50:20–25, 2018. URL https://www.researchgate.net/profile/Sneha-Sheokand-2/publication/324475605_Pharmaceutical_Nanocrystals_From_Fundamentals_to_Advances/links/5acf06684585154f3f457f52/Pharmaceutical-Nanocrystals-From-Fundamentals-to-Advances.pdf.

[128] Jingkun Jiang, Günter Oberdörster, and Pratim Biswas. Characterization of size, surface charge, and agglomeration state of nanoparticle dispersions for toxicological studies. *Journal of Nanoparticle Research*, 11(1):77–89, 2009. doi: 10.1007/s11051-008-9446-4. URL https://doi.org/10.1007/s11051-008-9446-4.

[129] Laura J. Cote, Franklin Kim, and Jiaxing Huang. Langmuir-blodgett assembly of graphite oxide single layers. *Journal of the American Chemical Society*, 131(3):1043–1049, 2009. doi: 10.1021/ja806262m. URL https://doi.org/10.1021/ja806262m. PMID: 18939796.

[130] Abdulla Muththalib and Béatrice Baudet. Effect of heavy metal contamination on the plasticity of kaolin-bentonite clay mixtures and an illite-smectite rich natural clay. *E3S Web of Conferences*, 92:10005, 01 2019. doi: 10.1051/e3sconf/20199210005.

[131] Robert J Hunter. *Zeta potential in colloid science: principles and applications*, volume 2. Academic press, 2013.

[132] Athanasios B Bourlinos, Vasilios Georgakilas, Radek Zboril, Theodore A Steriotis, and Athanasios K Stubos. Liquid-phase exfoliation of graphite towards solubilized graphenes. *small*, 5(16):1841–1845, 2009. doi: 10.1002/smll.200900242. URL https://www.rcptm.com/wp-content/uploads/2012/08/2009-SMALL-Liquid-Phase-Exfoliation-of-Graphite-Towards-Solubilized-Graphenes.pdf.

[133] Yenny Hernandez, Valeria Nicolosi, Mustafa Lotya, Fiona M Blighe, Zhenyu Sun, Sukanta De, IT McGovern, Brendan Holland, Michele Byrne, Yurii K Gun'Ko, et al. High-yield production of graphene by liquid-phase exfoliation of graphite. *Nature nanotechnology*, 3(9):563–568, 2008. doi: 10.1038/nnano.2008.215. URL https://doi.org/10.1038/nnano.2008.215.

[134] Sajini Vadukumpully, Jinu Paul, and Suresh Valiyaveettil. Cationic surfactant mediated exfoliation of graphite into graphene flakes. *Carbon*, 47(14):3288–3294, 2009. ISSN 0008-6223. doi: https://doi.org/10.1016/j.carbon.2009.07.049. URL https://www.sciencedirect.com/science/article/pii/S0008622309004849.

[135] Mustafa Lotya, Paul J King, Umar Khan, Sukanta De, and Jonathan N Coleman. High-concentration, surfactant-stabilized graphene dispersions. *ACS Nano*, 4(6):3155–3162, 2010. doi: 10.1021/nn1005304. URL https://doi.org/10.1021/nn1005304. PMID: 20455583.

[136] Sungjin Park, Jinho An, Richard D. Piner, Inhwa Jung, Dongxing Yang, Aruna Velamakanni, SonBinh T. Nguyen, and Rodney S. Ruoff. Aqueous suspension and characterization of chemically modified graphene sheets. *Chemistry of Materials*, 20(21):6592–6594, 2008. doi: 10.1021/cm801932u. URL https://doi.org/10.1021/cm801932u.

[137] Henk N. W. Lekkerkerker and Remco Tuinier. *Depletion Interaction*, pages 57–108. Springer Netherlands, Dordrecht, 2011. ISBN 978-94-007-1223-2. doi: 10.1007/978-94-007-1223-2_2. URL https://doi.org/10.1007/978-94-007-1223-2_2.

[138] Xu Zhang, Mark R. Servos, and Juewen Liu. Ultrahigh nanoparticle stability against salt, ph, and solvent with retained surface accessibility via depletion stabilization. *Journal of the American Chemical Society*, 134(24):9910–9913, 2012. doi: 10.1021/ja303787e. URL https://doi.org/10.1021/ja303787e. PMID: 22646098.

[139] Robert J. Hunter. *Zeta potential in colloid science*, pages 239–245. Academic Press, Australia, 1981.

[140] Epikote Resin 828 Product Data Sheet. https://www.hexion.com/en-US/product/epikote-resin-828, 2007. Accessed: 2020-03-02.

[141] Bisphenol A Diglycidyl Ether Product Specification Sheet. https://www.sigmaaldrich.com/catalog/product/SIGMA/D3415?lang=en&region=NO&gclid=Cj0KCQjwyZmEBhCpARIsALIzmnIT9j_pT3ggPFF0nm-KDlbfwNB6_xksDrn6PLqn6QwurKwpdEf9AX0aAvIxEALw_wcB. Accessed: 2020-03-02.

[142] Catalina H Musinoi Hagen, Alexander Kristoffersen, and Ole Øystein Knudsen. The effect of surface profile on coating adhesion and corrosion resistance. In *NACE International Corrosion Conference Proceedings*, page 1. NACE International, 2016. URL https://search.proquest.com/conference-papers-proceedings/effect-surface-profile-on-coating-adhesion/docview/1863196741/se-2?accountid=12870.

[143] N.N.A.H. Meis, L.G.J. van der Ven, R.A.T.M. van Benthem, and G. de With. Extreme wet adhesion of a novel epoxy-amine coating on aluminum alloy 2024-t3. *Progress in Organic Coatings*, 77(1): 176–183, 2014. ISSN 0300-9440. doi: https://doi.org/10.1016/j.porgcoat.2013.09.001. URL https://www.sciencedirect.com/science/article/pii/S030094401300235X.

[144] A. J. Scardino, H. Zhang, D. J. Cookson, R. N. Lamb, and R. de Nys. The role of nano-roughness in antifouling. *Biofouling*, 25(8):757–767, 2009. doi: 10.1080/08927010903165936. URL https://doi.org/10.1080/08927010903165936. PMID: 20183134.

[145] Eric Holm, Michael Schultz, Elizabeth Haslbeck, Walter Talbott, and Andrew Field. Evaluation of hydrodynamic drag on experimental fouling-release surfaces, using rotating disks. *Biofouling*, 20(4-5):219–226, 2004. doi: 10.1080/08927010400011245. URL https://doi.org/10.1080/08927010400011245. PMID: 15621643.

[146] E.S. Gadelmawla, M.M. Koura, T.M.A. Maksoud, I.M. Elewa, and H.H. Soliman. Roughness parameters. *Journal of Materials Processing Technology*, 123(1):133–145, 2002. ISSN 0924-0136. doi: https://doi.org/10.1016/S0924-0136(02)00060-2. URL https://www.sciencedirect.com/science/article/pii/S0924013602000602.

[147] DA Lange, HM Jennings, and Surendra P Shah. Analysis of surface roughness using confocal microscopy. *Journal of Materials Science*, 28(14):3879–3884, 1993. doi: 10.1007/BF00353195. URL https://doi.org/10.1007/BF00353195.

[148] Simon Dennington, Ponkrit Mekkhunthod, Martin Rides, David Gibbs, Maria Salta, Victoria Stoodley, Julian Wharton, and Paul Stoodley. Miniaturized rotating disc rheometer test for rapid screening of drag reducing marine coatings. *Surface Topography: Metrology and Properties*, 3(3):034004, 2015. doi: 10.1088/2051-672X/3/3/034004. URL https://iopscience.iop.org/article/10.1088/2051-672X/3/3/034004/meta.

[149] Abraham Marmur, Claudio Della Volpe, Stefano Siboni, Alidad Amirfazli, and Jaroslaw W. Drelich. Contact angles and wettability: towards common and accurate terminology. *Surface Innovations*, 5(1): 3–8, 2017. doi: 10.1680/jsuin.17.00002. URL https://doi.org/10.1680/jsuin.17.00002.

[150] Boaz Mizrahi, Xiaojuan Khoo, Homer H. Chiang, Katalina J. Sher, Rose G. Feldman, Jung-Jae Lee, Silvia Irusta, and Daniel S. Kohane. Long-lasting antifouling coating from multi-armed polymer. *Langmuir*, 29(32):10087–10094, 2013. doi: 10.1021/la4014575. URL https://doi.org/10.1021/la4014575. PMID: 23855875.

[151] Mark C.M. Van Loosdrecht, W. Norde, and A.J.B. Zehnder. Physical chemical description of bacterial adhesion. *Journal of Biomaterials Applications*, 5(2):91–106, 1990. doi: 10.1177/088532829000500202. URL https://doi.org/10.1177/088532829000500202. PMID: 2266489.

[152] Fereshte Taherian, Valentina Marcon, Nico F. A. van der Vegt, and Frédéric Leroy. What is the contact angle of water on graphene? *Langmuir*, 29(5):1457–1465, 2013. doi: 10.1021/la304645w. URL https://doi.org/10.1021/la304645w. PMID: 23320893.

[153] Ning Wei, Cunjing Lv, and Zhiping Xu. Wetting of graphene oxide: A molecular dynamics study. *Langmuir*, 30(12):3572–3578, 2014. doi: 10.1021/la500513x. URL https://doi.org/10.1021/la500513x. PMID: 24611723.

[154] Dmitriy A Dikin, Sasha Stankovich, Eric J Zimney, Richard D Piner, Geoffrey HB Dommett, Guennadi Evmenenko, SonBinh T Nguyen, and Rodney S Ruoff. Preparation and characterization of graphene oxide paper. *Nature*, 448(7152):457–460, 2007. doi: https://doi.org/10.1038/nature06016. URL https://www.nature.com/articles/nature06016.

[155] Robert N Wenzel. Resistance of solid surfaces to wetting by water. *Industrial & Engineering Chemistry*, 28(8):988–994, 1936. doi: 10.1021/ie50320a024. URL https://pubs.acs.org/doi/pdf/10.1021/ie50320a024.

[156] Anna Rudawska and Elżbieta Jacniacka. Analysis for determining surface free energy uncertainty by the owen–wendt method. *International Journal of Adhesion and Adhesives*, 29(4):451–457, 2009. ISSN 0143-7496. doi: https://doi.org/10.1016/j.ijadhadh.2008.09.008. URL https://www.sciencedirect.com/science/article/pii/S0143749608001048.

[157] D.E Packham. Surface energy, surface topography and adhesion. *International Journal of Adhesion and Adhesives*, 23(6):437–448, 2003. ISSN 0143-7496. doi: https://doi.org/10.1016/S0143-7496(03)00068-X. URL https://www.sciencedirect.com/science/article/pii/S014374960300068X.

[158] Christopher Rulison. So you want to measure surface energy. *Charlotte NC (cf. p. 99)*, 1999.

[159] D. K. Owens and R. C. Wendt. Estimation of the surface free energy of polymers. *Journal of Applied Polymer Science*, 13(8):1741–1747, 1969. doi: https://doi.org/10.1002/app.1969.070130815. URL https://onlinelibrary.wiley.com/doi/abs/10.1002/app.1969.070130815.

[160] Dimitri Janssen, Randy De Palma, Stijn Verlaak, Paul Heremans, and Wim Dehaen. Static solvent contact angle measurements, surface free energy and wettability determination of various self-assembled monolayers on silicon dioxide. *Thin Solid Films*, 515(4):1433–1438, 2006. ISSN 0040-6090. doi: https://doi.org/10.1016/j.tsf.2006.04.006. URL https://www.sciencedirect.com/science/article/pii/S0040609006005372.

[161] D. H. Kaelble. Dispersion-polar surface tension properties of organic solids. *The Journal of Adhesion*, 2(2):66–81, 1970. doi: 10.1080/0021846708544582. URL https://doi.org/10.1080/0021846708544582.

[162] M Żenkiewicz. Methods for the calculation of surface free energy of solids. *Journal of Achievements in Materials and Manufacturing Engineering*, 24(1):137–145, 2007. doi: 10.1.1.508.3775. URL http://citeseerx.ist.psu.edu/viewdoc/download?doi=10.1.1.508.3775&rep=rep1&type=pdf.

[163] Frederick M Fowkes. Dispersion force contributions to surface and interfacial tensions, contact angles, and heats of immersion. ACS Publications, 1964.

[164] LA Girifalco and Robert J Good. A theory for the estimation of surface and interfacial energies. i. derivation and application to interfacial tension. *The Journal of Physical Chemistry*, 61(7):904–909, 1957.

[165] Alexander I Railkin. *Marine biofouling: colonization processes and defenses*. CRC press, 2003.

[166] A. Hamza, V.A. Pham, T. Matsuura, and J.P. Santerre. Development of membranes with low surface energy to reduce the fouling in ultrafiltration applications. *Journal of Membrane Science*, 131(1):217–227, 1997. ISSN 0376-7388. doi: https://doi.org/10.1016/S0376-7388(97)00050-1. URL https://www.sciencedirect.com/science/article/pii/S0376738897000501.

[167] James A Callow and Maureen E Callow. Trends in the development of environmentally friendly fouling-resistant marine coatings. *Nature communications*, 2(1):1–10, 2011. doi: 10.1038/ncomms1251. URL https://www.nature.com/articles/ncomms1251#citeas.

[168] Stephen C Dexter. Influence of substratum critical surface tension on bacterial adhesion—in situ studies. *Journal of Colloid and Interface Science*, 70(2):346–354, 1979. ISSN 0021-9797. doi: https://doi.org/10.1016/0021-9797(79)90038-9. URL https://www.sciencedirect.com/science/article/pii/0021979779900389.

[169] William D. Callister and David G. Rethwisch. *Materials Science and Engineering*, pages 496–503. Wiley & Sons, Asia, 2015. ISBN 978-1-118-31922-2.

[170] A.A Volinsky, N.R Moody, and W.W Gerberich. Interfacial toughness measurements for thin films on substrates. *Acta Materialia*, 50(3):441–466, 2002. ISSN 1359-6454. doi: https://doi.org/10.1016/S1359-6454(01)00354-8. URL https://www.sciencedirect.com/science/article/pii/S1359645401003548.

[171] Shakeel A. Shahdad, John F. McCabe, Steven Bull, Sandra Rusby, and Robert W. Wassell. Hardness measured with traditional vickers and martens hardness methods. *Dental Materials*, 23(9):1079–1085, 2007. ISSN 0109-5641. doi: https://doi.org/10.1016/j.dental.2006.10.001. URL https://www.sciencedirect.com/science/article/pii/S0109564106002600.

[172] Jean-Marc Schneider, Maxence Bigerelle, and Alain Iost. Statistical analysis of the vickers hardness. *Materials Science and Engineering: A*, 262(1):256–263, 1999. ISSN 0921-5093. doi: https://doi.org/10.1016/S0921-5093(98)01000-4. URL https://www.sciencedirect.com/science/article/pii/S0921509398010004.

[173] Juhani Valli and Ulla Mäkelä. Applications of the scratch test method for coating adhesion assessment. *Wear*, 115(1):215–221, 1987. ISSN 0043-1648. doi: https://doi.org/10.1016/0043-1648(87)90211-0. URL https://www.sciencedirect.com/science/article/pii/0043164887902110.

[174] A. R. Di Sarli and C. I. Elsner. Influence of coating thickness on the barrier effect of marine paint binders: An assessment using impedance measurements. *Journal of Chemical Technology & Biotechnology*, 55(3): 285–292, 1992. doi: https://doi.org/10.1002/jctb.280550314. URL https://onlinelibrary.wiley.com/doi/abs/10.1002/jctb.280550314.

[175] D. E. Wendt, G. L. Kowalke, J. Kim, and I. L. Singer. Factors that influence elastomeric coating performance: the effect of coating thickness on basal plate morphology, growth and critical removal stress of the barnacle balanus amphitrite. *Biofouling*, 22(1):1–9, 2006. doi: 10.1080/08927010500499563. URL https://doi.org/10.1080/08927010500499563. PMID: 16551556.

[176] A. Kosari, P. Visser, F. Tichelaar, S. Eswara, J-N. Audinot, T. Wirtz, H. Zandbergen, H. Terryn, and J.M.C. Mol. Cross-sectional characterization of the conversion layer formed on aa2024-t3 by a lithium-leaching coating. *Applied Surface Science*, 512:145665, 2020. ISSN 0169-4332. doi: https://doi.org/10.1016/j.apsusc.2020.145665. URL https://www.sciencedirect.com/science/article/pii/S0169433220304219.

[177] Runze Chen, Yunsheng Zhang, Qingyi Xie, Zixin Chen, Chunfeng Ma, and Guangzhao Zhang. Transparent polymer-ceramic hybrid antifouling coating with superior mechanical properties. *Advanced Functional Materials*, 31(19):2011145, 2021. doi: https://doi.org/10.1002/adfm.202011145. URL https://onlinelibrary.wiley.com/doi/abs/10.1002/adfm.202011145.

[178] Effendi Widjaja and Marc Garland. Reverse engineering of multi-layer films. *Materials Today*, 14(3): 114–117, 2011. ISSN 1369-7021. doi: https://doi.org/10.1016/S1369-7021(11)70061-X. URL https://www.sciencedirect.com/science/article/pii/S136970211170061X.

[179] Francesca Cappitelli and Claudia Sorlini. Microorganisms attack synthetic polymers in items representing our cultural heritage. *Applied and environmental microbiology*, 74(3):564, 2008. doi: 10.1128/AEM.01768-07. URL https://www.ncbi.nlm.nih.gov/pmc/articles/PMC2227722/.

[180] Rolf-Joachim Mueller. Biological degradation of synthetic polyesters—enzymes as potential catalysts for polyester recycling. *Process Biochemistry*, 41(10):2124–2128, 2006. ISSN 1359-5113. doi: https://doi.org/10.1016/j.procbio.2006.05.018. URL https://www.sciencedirect.com/science/article/pii/S1359511306002200. From Biochemical Engineering to Systems Biology.

[181] Caroline Richard, Smita Mitbavkar, and Jessem Landoulsi. Diagnosis of the diatom community upon biofilm development on stainless steels in natural freshwater. *Scanning*, 2017, 2017. doi: 10.1155/2017/5052646. URL https://doi.org/10.1155/2017/5052646.

[182] Juan Carlos Camacho-Chab, Benjamín O Ortega-Morales, Christine Gaylarde, Juan E Pereañez-Sacarías, Hilda P León-Tejera, Rodrigo E Tun-Che, Radames J Álvarez-Zapata, Augusto I Almeyda-Cen, William Talavera-Pech, and Juan F Illescas-Salinas. Influence of silver nanoparticle–based coating on calcareous rock surfaces on microbial biofilm colonization in intertidal environments in campeche, mexico. *Water, Air, & Soil Pollution*, 232(5):1–15, 2021. doi: 10.1007/s11270-021-05123-1. URL https://doi.org/10.1007/s11270-021-05123-1.

[183] Fabrizio Di Caprio. Methods to quantify biological contaminants in microalgae cultures. *Algal Research*, 49:101943, 2020. ISSN 2211-9264. doi: https://doi.org/10.1016/j.algal.2020.101943. URL https://www.sciencedirect.com/science/article/pii/S2211926419312068.

[184] CJ Zhu and YK Lee. Determination of biomass dry weight of marine microalgae. *Journal of applied phycology*, 9(2):189–194, 1997. doi: 10.1023/A:1007914806640. URL https://doi.org/10.1023/A:1007914806640.

[185] Yanyan Su, Torben A Lenau, Emil Gundersen, Jacob JK Kirkensgaard, Christian Maibohm, Jérôme Pinti, and Marianne Ellegaard. The uv filtering potential of drop-casted layers of frustules of three diatom species. *Scientific reports*, 8(1):1–10, 2018. doi: 10.1038/s41598-018-19596-4. URL https://doi.org/10.1038/s41598-018-19596-4.

[186] Matilde Skogen Chauton, Lotte MB Skolem, Lasse Mork Olsen, Per Erik Vullum, John Walmsley, and Olav Vadstein. Titanium uptake and incorporation into silica nanostructures by the diatom pinnularia sp.(bacillariophyceae). *Journal of applied phycology*, 27(2):777–786, 2015. doi: 10.1007/s10811-014-0373-8. URL https://doi.org/10.1007/s10811-014-0373-8.

[187] Stine Sandbakk. Graphene oxide coatings for anti-fouling application. Master's thesis, Norwegian University of Science and Technology, 2020.

[188] Poly(propylene glycol)bis(2-aminopropyl ether) Safety Data Sheet. https://www.sigmaaldrich.com/MSDS/MSDS/DisplayMSDSPage.do?country=NO&language=no&productNumber=406651&brand=ALDRICH&PageToGoToURL=https%3A%2F%2Fwww.sigmaaldrich.com%2Fcatalog%2Fproduct%2Faldrich%2F406651%3Flang%3Den. Accessed: 2020-03-02.

[189] Aceton > 99%, Technical Safety Data Sheet. https://no.vwr.com/store/product/721128/aceton-99-technical. Accessed: 2020-03-02.

[190] Etanol Absolute Safety Data Sheet. https://no.vwr.com/store/product/20430052/etanol-absolute-vlsi. Accessed: 2020-03-02.

[191] A. H. Dam. Cealtech AS. Personal communication. Date: 2020-01-18.

[192] M. S. Chauton. SINTEF Ocean. Personal communication. Date: 2020-02-01.

[193] T. Brembu. NTNU - Department of Biotechnology and Food Science. Personal communication. Date: 2020-02-01.

[194] S Benjamin, C Carr, and D.J Walbridge. Self-stratifying coatings for metallic substrates. *Progress in Organic Coatings*, 28(3):197–207, 1996. ISSN 0300-9440. doi: https://doi.org/10.1016/0300-9440(95)00596-X. URL https://www.sciencedirect.com/science/article/pii/030094409500596X.

[195] H. Mitsui, T. Yoshimitsu, Y. Mizutani, and K. Umemoto. Electrical failure properties of cast epoxy resins. *IEEE Transactions on Electrical Insulation*, EI-16(6):533–542, 1981. doi: 10.1109/TEI.1981.298385. URL https://ieeexplore.ieee.org/abstract/document/4080893.

[196] A Cherdoud-Chihani, M Mouzali, and MJM Abadie. Study of crosslinking acid copolymer/dgeba systems by ftir. *Journal of applied polymer science*, 87(13):2033–2051, 2003. doi: https://doi.org/10.1002/app.11389. URL https://onlinelibrary.wiley.com/doi/full/10.1002/app.11389.

[197] Mehmet S Eroğlu, M Melih Akilli, and Olgun Güven. Spectroscopic, thermal, and mechanical characterization of carboxyl-terminated polybutadiene-based carbon black-filled networks. *Journal of applied polymer science*, 66(2):355–366, 1997. doi: 0021-8995/97/020355-12. URL https://onlinelibrary.wiley.com/doi/abs/10.1002/(SICI)1097-4628(19971010)66:2%3C355::AID-APP16%3E3.0.CO;2-X.

[198] Sławomir Jaworski, Mateusz Wierzbicki, Ewa Sawosz, Anna Jung, Grzegorz Gielerak, Joanna Biernat, Henryk Jaremek, Witold Łojkowski, Bartosz Woźniak, Jacek Wojnarowicz, et al. Graphene oxide-based nanocomposites decorated with silver nanoparticles as an antibacterial agent. *Nanoscale research letters*, 13(1):116, 2018. doi: 10.1186/s11671-018-2533-2. URL https://link.springer.com/article/10.1186/s11671-018-2533-2.

[199] Wei Gao. *Graphite oxide: Structure, reduction and applications*. PhD thesis, 2012. URL https://scholarship.rice.edu/handle/1911/64614.

[200] Mohammad A Aldosari, Ali A Othman, and Edreese H Alsharaeh. Synthesis and characterization of the in situ bulk polymerization of pmma containing graphene sheets using microwave irradiation. *Molecules*, 18(3):3154, 2013. doi: 10.3390/molecules18033152. URL https://www.mdpi.com/1420-3049/18/3/3152.

[201] Huafeng Yang, Changsheng Shan, Fenghua Li, Qixian Zhang, Dongxue Han, and Li Niu. Convenient preparation of tunably loaded chemically converted graphene oxide/epoxy resin nanocomposites from graphene oxide sheets through two-phase extraction. *Journal of Materials Chemistry*, 19(46):8856–8860, 2009. doi: 10.1039/B915228H. URL https://pubs.rsc.org/--/content/articlehtml/2009/jm/b915228h.

[202] Kruss. Polar Part. https://www.kruss-scientific.com/en/know-how/glossary/polar-part, . Accessed: 2021-02-05.

[203] Kruss. Dispersive Part. https://www.kruss-scientific.com/en/know-how/glossary/dispersive-part, . Accessed: 2021-02-05.

[204] Alice L. Alldredge and Mary W. Silver. Characteristics, dynamics and significance of marine snow. *Progress in Oceanography*, 20(1):41–82, 1988. ISSN 0079-6611. doi: https://doi.org/10.1016/0079-6611(88)90053-5. URL https://www.sciencedirect.com/science/article/pii/0079661188900535.

[205] Ditet Von Wettstein, Simon Gough, and C Gamini Kannangara. Chlorophyll biosynthesis. *The Plant Cell*, 7(7):1039, 1995. doi: 10.1105/tpc.7.7.1039. URL https://www.ncbi.nlm.nih.gov/pmc/articles/PMC160907/.

[206] Farooq Azam, Barbara B Hemmingsen, and Benjamin E Volcani. Role of silicon in diatom metabolism. *Archives of Microbiology*, 97(1):103–114, 1974. doi: 10.1007/BF00403050. URL https://link.springer.com/article/10.1007/BF00403050.

[207] Kouji Adachi and Peter R. Buseck. Changes in shape and composition of sea-salt particles upon aging in an urban atmosphere. *Atmospheric Environment*, 100:1–9, 2015. ISSN 1352-2310. doi: https://doi.org/10.1016/j.atmosenv.2014.10.036. URL https://www.sciencedirect.com/science/article/pii/S1352231014008255.

[208] Sina Schorn, Verena Salman-Carvalho, Sten Littmann, Danny Ionescu, Hans-Peter Grossart, and Heribert Cypionka. Cell Architecture of the Giant Sulfur Bacterium Achromatium oxaliferum: Extra-cytoplasmic Localization of Calcium Carbonate Bodies. *FEMS Microbiology Ecology*, 96(2), 12 2019. ISSN 0168-6496. doi: 10.1093/femsec/fiz200. URL https://doi.org/10.1093/femsec/fiz200. fiz200.

[209] E.J. Gelissen, C.W.M. van der Geld, M.W. Baltussen, and J.G.M. Kuerten. Modeling of droplet impact on a heated solid surface with a diffuse interface model. *International Journal of Multiphase Flow*, 123:103173, 2020. ISSN 0301-9322. doi: https://doi.org/10.1016/j.ijmultiphaseflow.2019.103173. URL https://www.sciencedirect.com/science/article/pii/S0301932219307529.

[210] Shibing Ye and Jiachun Feng. The effect of sonication treatment of graphene oxide on the mechanical properties of the assembled films. *RSC advances*, 6(46):39681–39687, 2016. doi: 10.1039/c6ra03996k. URL https://pubs.rsc.org/en/content/articlelanding/2016/ra/c6ra03996k/unauth#!divAbstract.

[211] Longqiang Ye, Yulu Zhang, Changchun Song, Yuanyang Li, and Bo Jiang. A simple sol-gel method to prepare superhydrophilic silica coatings. *Materials Letters*, 188:316–318, 2017. ISSN 0167-577X. doi: https://doi.org/10.1016/j.matlet.2016.09.043. URL https://www.sciencedirect.com/science/article/pii/S0167577X16315038.

Appendix

A Calculations

Epoxy coatings were made with graphene oxide (GO) or graphene (G) as antifouling agents and the material properties of the chemicals involved in the synthesis are shown in Table A.1.

Table A.1: Material properties of the chemicals used to prepare epoxy coatings [140, 141, 188, 189, 190, 191]. Graphene oxide (GO) and graphene (G) were dispersed as antifouling (AF) agents within the epoxy coatings.

Chemical	Abbreviation	Function	Molar mass, Mm [g/mol]	Density, ρ [g/mL]	Purity, p [-]	Molar ratio, mr [-]
DGEBA	D	Resin	340.41	1.160	1.000	1.0
Epikote	E	Resin	184.00 - 190.00	1.160	1.000	1.0
PPGBAE	P	Curing agent	230.00	0.948	1.000	0.5
Ethanol	EtOH	Solvent	46.07	0.790	0.999	-
Acetone	-	Solvent	58.08	0.792	0.990	-
Graphene oxide paste	GO paste	AF agent	-	-	0.100	-
Graphene-Epikote dispersion	G-Epikote	Precursor G slurries	-	-	0.006	-

A.1 Synthesis of epoxy sols

Epoxy sols with 90 wt% solvent compared to mass epoxy were prepared with a fixed mass of epoxy set to 60 g. The mass of solvent required to obtain the given weight ratio (wr) was calculated by the following equation:

$$m_s[g] = m_{epoxy} \cdot wr \tag{A.1}$$

With m_s being the mass of solvent, m_{epoxy} being the fixed mass of epoxy and wr being the chosen weight ratio between solvent and epoxy set to 0.9.

The mass percent of epoxy (mp_{epoxy}) compared to the solvent was then found by

$$mp_{epoxy}[-] = \frac{m_{epoxy}}{m_{epoxy} + m_s} \tag{A.2}$$

The solvent mixture for the DGEBA sol contained 50 wt% Acetone and 50 wt% EtOH. Acetone was the only solvent in the Epikote sol. The mass of each solvent component required to prepare the DGEBA sol was calculated by the following equation:

$$m_{acetone}[g] = m_{EtOH}[g] = m_s \cdot 0.5 \tag{A.3}$$

The required mass of solvent in the Epikote sol was calculated by Equation A.1. The required mass of each component required to synthesize the epoxy sols are shown in Table 3.4.

A.2 Synthesis of GO slurry

GO slurries were made by extracting 50 g of the prepared DGEBA sol and mixing with desired amounts of GO paste to obtain slurries with 0.125, 0.250, 0.500 and 0.750 wt% GO compared

to mass DGEBA. The mass of DGEBA in the extracted sol ($m_{D_{slurry}}$) was found by

$$m_{Dslurry}[g] = mp_D \cdot m_{sol} \tag{A.4}$$

With mp_D being calculated using Equation A.2 and m_{sol} being the extracted mass of DGEBA sol set as 50 g.

The mass of solvent ($m_{s,slurry}$) in the extracted sol was found by

$$m_{s,slurry}[g] = m_{sol} - m_{Dslurry} \tag{A.5}$$

The required mass of GO to prepare the GO slurries was found by the following equation:

$$m_{GOslurry}[g] = wr_{GO} \cdot m_{Dslurry} \tag{A.6}$$

Where wr_{GO} is the weight ratio of GO compared to mass DGEBA and mass of DGEBA in the extracted sol ($m_{D_{slurry}}$) being calculated in Equation A.4.

As the GO paste used in the preparation contained 10 wt% GO, the mass of GO paste to be added to obtain the desired weight ratios of GO compared to DGEBA was calculated by

$$m_{GO,pasteslurry}[g] = \frac{m_{GOslurry}}{wr_{GOpaste}} \tag{A.7}$$

with $wr_{GOpaste}$ being the purity of the GO paste reported as 0.1 as shown in Table A.1.

The masses of each component required to prepare GO slurries are shown in Table 3.5.

A.3 Synthesis of G slurries

Graphene slurries containing 0.125 wt% G and 0.250 wt% G compared to mass Epikote was prepared from the distributed graphene-Epikote dispersion with 0.6 wt% G. The G slurries should contain the same amount of epoxy as the GO slurries, and the required mass of Epikote in the G slurries ($m_{E_{slurry}}$) are therefore equal to the mass of DGEBA in the GO slurries which was calculated in Equation A.4.

The solvent in the G slurries is only acetone and the weight ratio between acetone and Epikote in the slurries was set as 0.9. Mass acetone can be calculated using Equation A.1.

The required mass of graphene in the slurries ($m_{G_{slurry}}$) was found using Equation A.6 with the weight ratio being set as 0.00125 and 0.00250. The mass of the G-Epikote to obtain the required mass of graphene in the slurries was calculated by

$$m_{G-Epikote}[g] = \frac{m_{G_{slurry}}}{wr_{G-Epikote}} \tag{A.8}$$

With $wr_{G-Epikote}$ being 0.006 as shown in Table A.1.

The mass of Epikote in the required mass of the 0.6 wt% G-Epikote dispersion is found by

$$m_{E_{G-Epikote}}[g] = m_{G-Epikote} \cdot (1 - 0.006) \tag{A.9}$$

The mass of extra Epikote which must be added to obtain the desired Epikote amount in the slurries can then be calculated as

$$m_{E_{extra}}[g] = m_{E_{slurry}} - m_{E_{G-Epikote}} \tag{A.10}$$

The masses of each chemical required to prepare the 0.125 wt% and 0.250 wt% G coatings are found in Table 3.6.

A.4 Coating batches

The masses of each coating corresponding to the mass required for one coating layer were found using the calculations explained in the following part. The mass required for one coating layer is referred to as one sol batch or slurry batch.

Sol batches

The calculations for DGEBA and Epikote are similar and therefore the calculations will be shown using the index epoxy which is referring to DGEBA and Epikote.

The mass of epoxy sol ($m_{sol_{batch}}$) in each batch was set as 0.5 g. The mass of epoxy in 0.5 g sol was calculated using Equation A.4 with the mass percent of the epoxy calculated using Equation A.2 as illustrated below:

$$m_{epoxy_{batch}}[g] = mp_{epoxy} \cdot m_{sol_{batch}} \tag{A.11}$$

The corresponding number of moles epoxy was found by

$$n_{epoxy_{batch}}[mol] = \frac{m_{epoxy_{batch}}}{Mm_{epoxy}} \tag{A.12}$$

For the Epikote epoxy, a molar mass of 187 g/mol was used in the calculations.

The corresponding number of moles of the curing agent was found from

$$n_{P_{batch}}[mol] = \frac{n_{epoxy_{batch}} \cdot mr_P}{mr_{epoxy}} \tag{A.13}$$

With mr_P and mr_{epoxy} being the molar ratios of the curing agent (PPGBAE) and the epoxy resin found in Table A.1.

The required volume of curing agent to be added to each batch was calculated by

$$V_{P_{batch}}[mL] = \frac{n_{P_{batch}} \cdot Mm_P}{\rho_P \cdot p_P} \tag{A.14}$$

With the molar mass (Mm), density (ρ) and purity (p) of the curing agent found in Table A.1.

It should be noted that the mass of epoxy will be the same in each batch, but number of moles differ as the epoxies exhibit different molar masses.

The required masses of epoxy sols and curing agent related to one batch which corresponds to one coating layer to be deposited, are shown in Table 3.8.

Slurry batches

The mass of epoxy in the slurry batches were set to be the same as the mass of epoxy in the corresponding sol batches which were calculated using Equation A.11.

The mass of solvent in the slurry batches ($m_{solvent_{slurrybatch}}$) were the same as the mass of solvent in the corresponding sol batches and could therefore be found from

$$m_{solvent_{slurrybatch}}[g] = m_{sol_{batch}} - m_{epoxy_{batch}} \tag{A.15}$$

with the $m_{sol_{batch}}$ being set to 0.5 g and $m_{epoxy_{batch}}$ being calculated in Equation A.11.

The desired mass of GO and G to be present in each batch was set as 0.125 wt% and 0.250 wt% compared to mass epoxy. The mass of GO or G in the batch could therefore be calculated as

$$m_{agent_{batch}}[g] = m_{epoxy_{batch}} \cdot wr_{agent} \tag{A.16}$$

With the index agent referring to GO or G and wr being the weight ratio between the agent and epoxy.

As GO was added to the slurry in form of GO paste which contains 10 wt% GO, the mass of GO paste in the batch could be calculated as

$$m_{GOpaste_{batch}}[g] = \frac{m_{GO_{batch}}}{p_{GO}} \tag{A.17}$$

With $m_{GO_{batch}}$ being calculated with Equation A.16 and the purity of the GO paste being reported as 0.1 as shown in Table A.1.

The required mass of GO slurry to obtain one batch with the same mass of DGEBA as the DGEBA sol batches was

The required mass of the GO slurries to obtain one batch could then be calculated using the following Equation:

$$m_{GOslurry_{batch}}[g] = m_{epoxy_{batch}} + m_{GOpaste_{batch}} + m_{solvent_{slurrybatch}} \tag{A.18}$$

With the index being DGEBA for the epoxy and acetone and ethanol for solvent.

The required mass of G slurries to obtain one batch was calculated with the following Equation:

$$m_{Gslurry_{batch}}[g] = m_{epoxy_{batch}} + m_{agent_{batch}} + m_{solvent_{slurrybatch}} \tag{A.19}$$

With the index being Epikote for epoxy, G for agent and acetone for solvent.

GO slurry batches and DGEBA sol batches contained the same amount of DGEBA and therefore the same volume of curing agent calculated in Equation A.14 was added. The same case appeared for the G slurry batches and the Epikote sol batches.

The required slurry masses required to prepare one GO slurry batch and G slurry batch are are found in Table 3.8.

B Dimensions of biofilm reactor

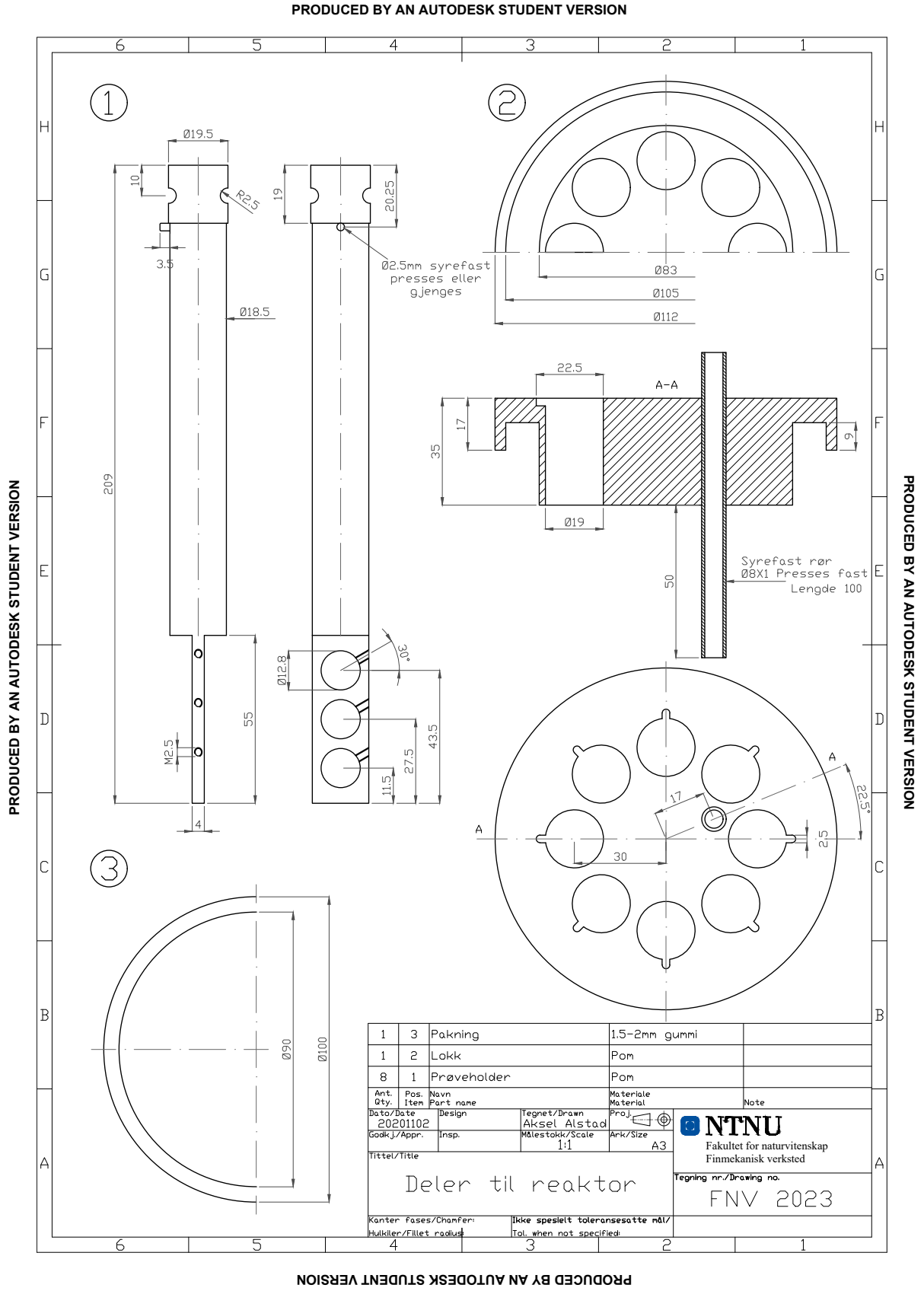

C MATLAB-code for estimations of biofilm thicknesses

The czi-files containing the Z-stacks from the measurements performed in *Zeiss LSM 800* were converted to binary files by using ImageJ. The procedure is described in the following:

1. Open the czi-file: File ⟶ Open
2. Duplicate the entire Z-stack: Right-click on the opened file and choose duplicate
3. Put on a medianfilter: Process ⟶ Filters ⟶ Median (2 pixels radius)
4. Enter a treshold to convert to binary image: Image ⟶ Adjust ⟶ Treshold ...
5. Choose methods and background: Otsu and B&W, check for "Dark background"
6. Click on Apply
7. Calculate the threshold for each image: Method: Otsu, Background: Dark and check for "Calculate threshold for each image"
8. Save the stach as a .TIFF file: File ⟶ Save As ⟶ TIFF ...
9. Note the voxel depth (called dz in the MATLAB-code below): Image ⟶ Properties

The following MATLAB-code was developed by Senior Engineer Astrid Bjørkøy and was used by the author to estimate the biofilm thicknesses of the binary files. The voxel depth (dz in the code) was adjusted for each image.

```
clear BW2 th
data = bfopen('C:\Users\marit\OneDrive\Dokumenter\MATLAB\
GO-ref-pos1-binary-tiffile');
prompt={'Enter slice'};
name='Input for first slice ';
defaultanswer={'1'};
numlines = 1;
Inputanswer = inputdlg(prompt,name,numlines,defaultanswer,'on');

sl_1 = str2double(char(Inputanswer));
seriesCount = size(data, 1)
series1 = data{1, 1};
series1_planeCount = size(series1, 1)
d = size(series1{1, 1});

z = size(series1)
imstr(3) = z(1)
dz = 1.09;

maske = ones(d(1),d(2));
for i = 1:z(1)
    BW2(:,:,i) = series1{i,1};
end

[r,c] = find(maske);
thpix = zeros(d(1),d(2));
```

```
poro = zeros(d(1),d(2));
topo = zeros(d(1),d(2));
th(1:length(r)) = 0;
for i = 1:length(r)
    T = BW2(r(i),c(i),:);
    k = find(T);
    if isempty(k)
       thpix(r(i),c(i)) = 0;
       poro(r(i),c(i)) = 0;
       topo(r(i),c(i)) = 0;
    else
       th(i) = (k(end)-k(1)+1)*dz;
       topo(r(i),c(i)) = (series1_planeCount - k(1))*dz;
       thpix(r(i),c(i)) = k(end)-k(1)+1;
       poro(r(i),c(i)) = (length(k))/(k(end)-k(1)+1);
    end
end

[a,b,Bio_th] = find(th);
disp('thickness and st.dev: ');
mean(Bio_th)
std(Bio_th)
disp('coverage: ');
length(Bio_th)/length(r)
Bio = sort(Bio_th);
%outliers = find(Bio > (mean(Bio_th)+2*std(Bio_th)));
%disp('outliers: ');
%length(outliers)/length(Bio_th)

figure
imagesc(topo)
colorbar

clear BW2
```

D FTIR-spectra of sols and slurries

The DGEBA sol and Epikote sol compositions appear stable over time as no significant changes in their transmittance spectra are observed as shown in Figure D.1. The transmittance spectra of the one day old DGEBA sol overlaps completely with the three weeks old DGEBA sol at wavenumbers ranging from 1710-2850 cm^{-1} in Figure D.1 and is therefore not visible.

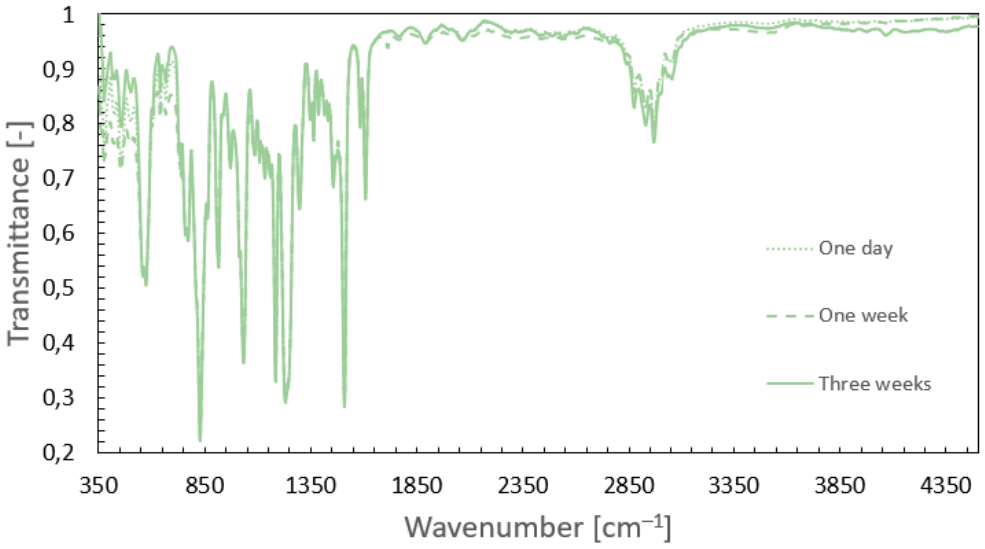

(a) DGEBA sol

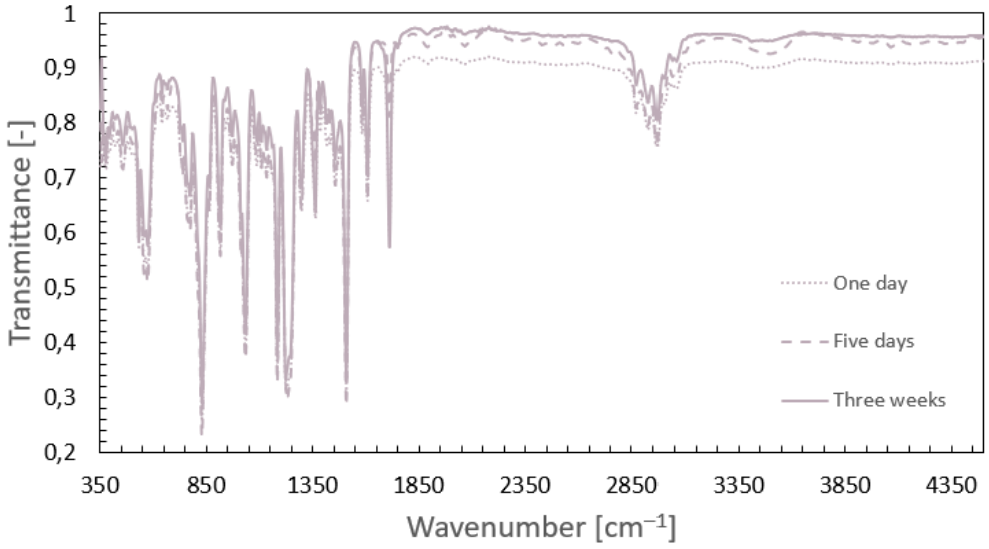

(b) Epikote sol

Figure D.1: The composition of the DGEBA sol and Epikote sol appear stable over time as no significant changes in their transmittance spectra are observed.

The full scale FTIR-spectra of three weeks old GO and G slurries and epoxy sols displaying the overlap of functional groups is shown in Figure D.2.

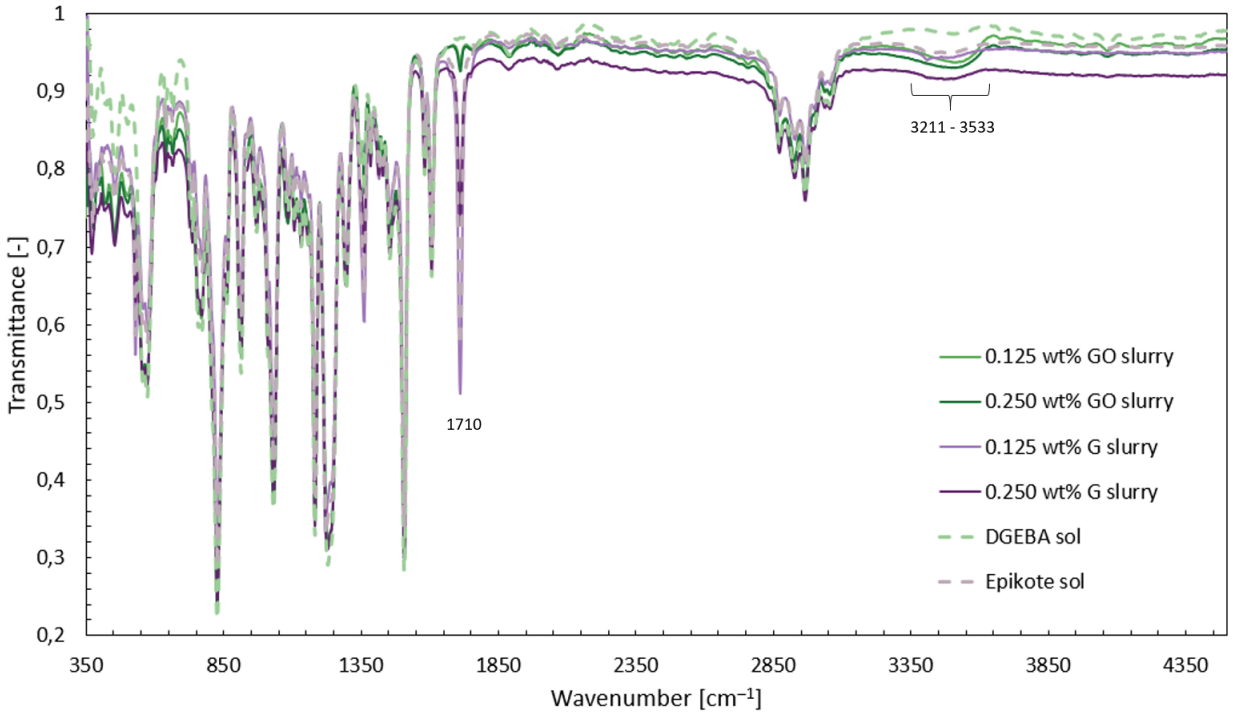

Figure D.2: Transmittance spectra of GO and G slurries and epoxy sols three weeks after preparation. The most significant changes are observed at peaks around 1710 cm^{-1} and in the range 3211-3533 cm^{-1}.

E Viscosity analysis

The viscosity estimations found in Table 4.2 was found by plotting shear stress against decreasing shear rates and performing linear regression which is shown in Figure E.1.

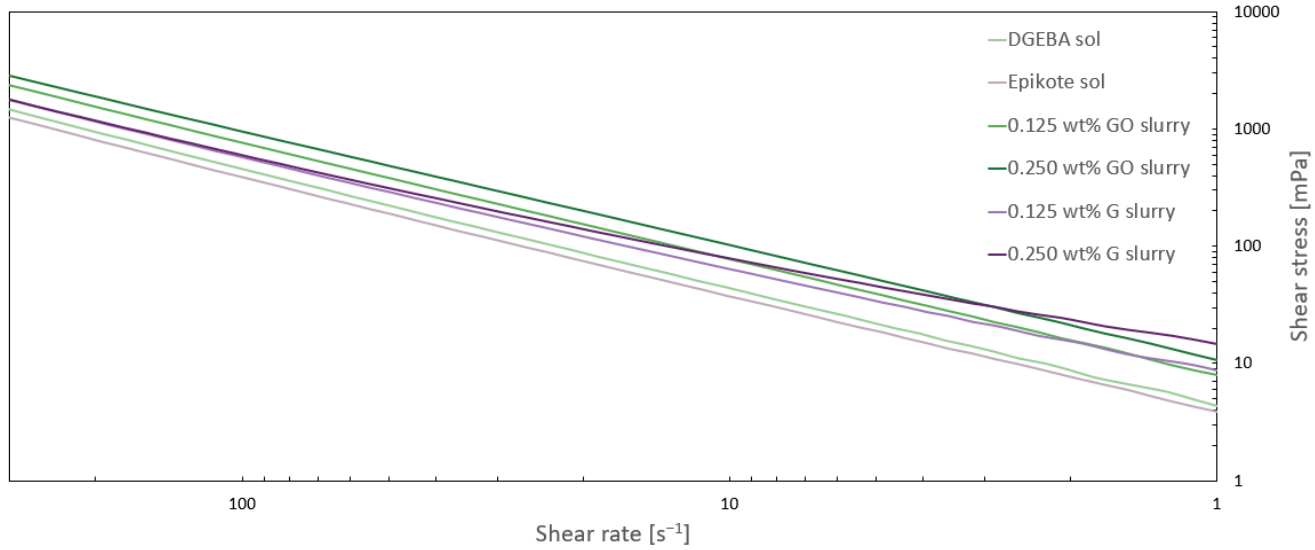

Figure E.1: Linear regressions of shear stress plotted as a function of decreasing shear rates.

F Surface roughness profiles

Surface profiles obtained from profilometer analysis of un-coated substrate and the four layer prepared coatings are shown in Figure F.1. Three positions per sample were measured. Surface profiles of the un-coated substrate and 0.250 wt% GO coating are also shown in Figure 4.15.

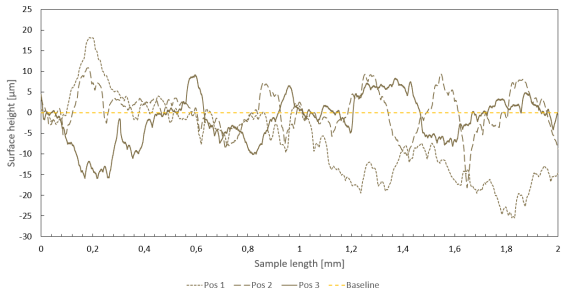

(a) Un-coated substrate

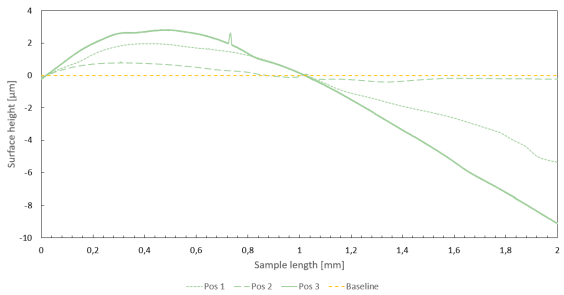

(b) DGEBA coating

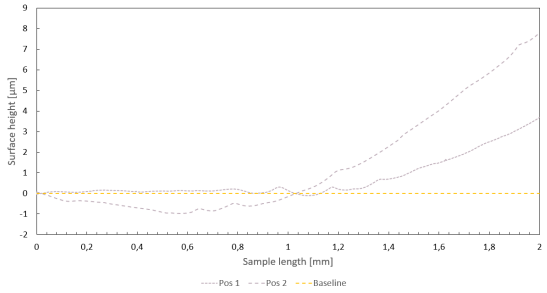

(c) Epikote coating

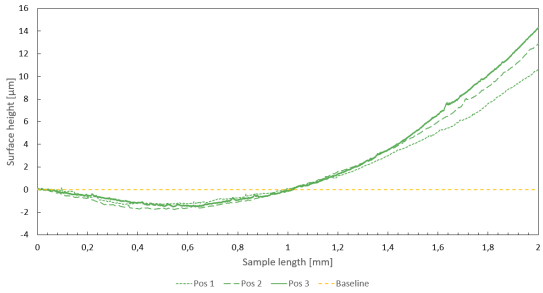

(d) 0.125 wt% GO coating

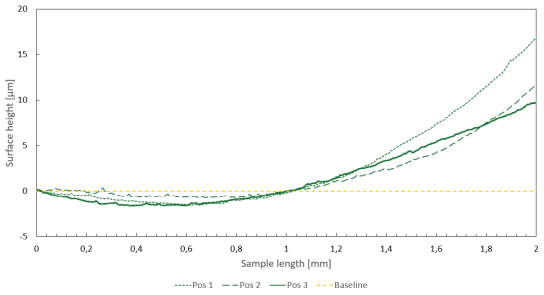

(e) 0.250 wt% GO coating

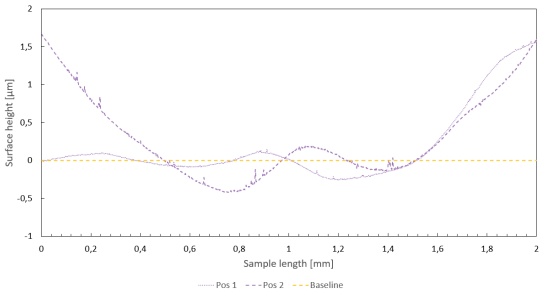

(f) 0.125 wt% G coating

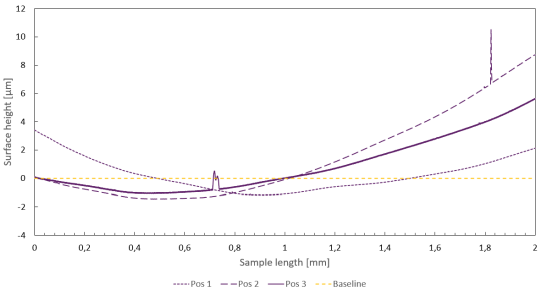

(g) 0.250 wt% G coating

Figure F.1: Surface profiles obtained from profilometer measurements. Surface profiles of the un-coated substrate and 0.25 wt% GO coating are also shown in Figure 4.15.

G Diatom growth on coated samples

The diatom growth in terms of number of diatom and percent diatom covered area for GO and G coatings being submerged for two weeks and four weeks are shown in Table G.1 and G.2 respectively.

Table G.1: Diatom growth on coated samples after submersion for two weeks.

Coating type [-]	Weight percent GO or G [wt%]	Number of coating layers [-]	Number of diatoms [-]	Diatom covered area [%]
GO	0.0	2	1.33	0.09
		3	2.33	0.11
		4	1.83	0.08
	0.125	2	0.67	0.03
		3	0.67	0.03
		4	10.83	0.45
	0.250	2	0.25	0.01
		3	0.33	0.01
		4	0.50	0.02
G	0.0	2	35.42	1.77
		3	35.25	2.47
		4	20.75	1.36
	0.125	2	15.58	0.87
		3	26.83	1.26
		4	23.50	1.15
	0.250	2	1.08	0.04
		3	13.92	0.50
		4	14.58	0.50

Table G.2: Diatom growth on coated samples after submersion for four weeks.

Coating type [-]	Weight percent GO or G [wt%]	Number of coating layers [-]	Number of diatoms [-]	Diatom covered area [%]
GO	0.0	2	1.92	0.08
		3	1.92	0.14
		4	8.33	0.33
	0.125	2	0.75	0.03
		3	1.42	0.04
		4	0.92	0.05
	0.250	2	1.75	0.08
		3	1.08	0.06
		4	1.17	0.06
G	0.0	2	118.33	8.34
		3	10.91	0.58
		4	23.17	1.21
	0.125	2	26.83	0.92
		3	18.92	0.87
		4	21.75	1.01
	0.250	2	25.17	1.04
		3	5.25	0.17
		4	111.83	3.77

NTNU

Norwegian University of
Science and Technology